

SURROGATE MODEL BASED SYSTEM IDENTIFICATION AND CONTROL  
OF GAS TURBINE ENGINES

A THESIS SUBMITTED TO  
THE GRADUATE SCHOOL OF NATURAL AND APPLIED SCIENCES  
OF  
MIDDLE EAST TECHNICAL UNIVERSITY

BY

SİNAN EKİNCİ

IN PARTIAL FULFILLMENT OF THE REQUIREMENTS  
FOR  
THE DEGREE OF DOCTOR OF PHILOSOPHY  
IN  
AEROSPACE ENGINEERING

JANUARY 2019



Approval of the thesis:

**SURROGATE MODEL BASED SYSTEM IDENTIFICATION AND  
CONTROL OF GAS TURBINE ENGINES**

submitted by **Sinan Ekinci** in partial fulfillment of the requirements for the degree  
of **Doctor of Philosophy in Aerospace Engineering Department, Middle East  
Technical University** by,

Prof. Dr. Halil Kalıpçılar  
Dean, Graduate School of **Natural and Applied Sciences**

Prof. Dr. İsmail Hakkı Tuncer  
Head of Department, **Aerospace Engineering**

Assoc. Prof. Dr. İlkey Yavrucuk  
Supervisor, **Aerospace Engineering Department, METU**

**Examining Committee Members:**

Prof. Dr. Metin Uymaz Salamcı  
Mechanical Engineering Department, Gazi University

Assoc. Prof. Dr. İlkey Yavrucuk  
Aerospace Engineering Department, METU

Prof. Dr. Oğuz UZOL  
Aerospace Engineering Department, METU

Prof. Dr. Coşku Kasnakoğlu  
Electrical and Electronics Engineering Department, TOBB ETÜ

Assist. Prof. Dr. Ali Türker Kutay  
Aerospace Engineering Department, METU

**Date:**



**I hereby declare that all information in this document has been obtained and presented in accordance with academic rules and ethical conduct. I also declare that, as required by these rules and conduct, I have fully cited and referenced all material and results that are not original to this work.**

Name, Last Name: Sinan Ekinçi

Signature :

## **ABSTRACT**

### **SURROGATE MODEL BASED SYSTEM IDENTIFICATION AND CONTROL OF GAS TURBINE ENGINES**

Ekinci, Sinan

Ph.D., Department of Aerospace Engineering

Supervisor : Assoc. Prof. Dr. İlkey Yavrucuk

January 2019, 98 pages

The focus of this thesis is on small low-cost turbojet engines where the fuel flow is provided by a gear-type fuel pump rather than a more traditional fuel metering unit. The incorporation of such type of fuel flow actuation devices introduces additional nonlinearities into the modeling and control of the small turbojet engines. As an alternative solution, this thesis presents and applies online/offline parameter estimation and adaptive control methods to such sub-class turbojet engines. For the simulation and analysis, a high-fidelity turbojet engine model including the fuel system is developed. On the other hand, a nonlinear fast engine model is proposed to capture the shaft dynamics of a small turbojet engine equipped with a gear-type fuel pump. The parameters of the fast engine model are estimated using the regression analysis. The same identification procedure is also applied to real engine test data to verify the proposed approach. Next, an online parameter estimation method using the same fast engine model structure is applied to the aero-thermal turbojet engine model. Then, the outputs of the offline and online parameter estimation approaches are compared with each other. Later, the online parameter estimation algorithm is converted to an

adaptive controller known as indirect-model reference adaptive control. Last, several control and failure scenarios are applied to the aero-thermal engine model to show its main advantages over the traditional control approaches and also to reveal its further application areas.

Keywords: Turbojet Engine Simulation, Fast Engine Model, Online System Identification, Model Reference Adaptive Control



## ÖZ

### GAZ TÜRBİN MOTORLARIN VEKİL MODEL TABANLI SİSTEM TANIMLAMASI VE KONTROLÜ

Ekinci, Sinan

Doktora, Havacılık ve Uzay Mühendisliği Bölümü

Tez Yöneticisi : Doç. Dr. İlkey Yavrucuk

Ocak 2019 , 98 sayfa

Bu tezin odak noktası, yakıt akışının daha geleneksel bir yakıt dozajlama ünitesinden ziyade dişli tip bir yakıt pompası tarafından sağlandığı küçük, düşük maliyetli turbojet motorlardır. Bu tip yakıt akışı eyleyicilerinin sisteme dahil edilmesi, küçük turbojet motorların modellenmesi ve kontrolüne ek doğrusal olmayan özellikler getirmektedir. Alternatif bir çözüm olarak, bu tezde, bu tür alt sınıf turbojet motorlara çevrimiçi / çevrimdışı parametre tahmini ve adaptif kontrol yöntemleri önerilmekte ve uygulanmaktadır. Benzetim ve analiz için yakıt sistemini de içeren yüksek doğrulukta bir turbojet motor modeli geliştirilmiştir. Öte yandan, doğrusal olmayan hızlı bir motor modeli, dişli tip bir yakıt pompasıyla donatılmış küçük bir turbojet motorunun shaft dinamiklerini yakalamak için önerilmiştir. Bu hızlı motor modelinin parametreleri, regresyon analizi yöntemi kullanılarak tahmin edilmiştir. Aynı tanımlama prosedürü, önerilen yaklaşımı doğrulamak için gerçek motor test verilerine de uygulanmıştır. Daha sonra, önerilen hızlı motor modeli yapısını kullanan bir çevrimiçi parametre tahmin yöntemi, aero-termal turbojet motor modeline uygulanmıştır. Ardından, çevrimdışı ve çevrimiçi parametre tahmin yaklaşımlarının çıktıları birbiriyle

karşılaştırılmıştır. Daha sonra, çevrimiçi parametre tahmin algoritması, dolaylı model referans uyarlamalı kontrol olarak bilinen bir adaptif kontrolcüye dönüştürülmüştür. Son olarak, geliştirilen kontrolcünün geleneksel kontrol yaklaşımlarına karşı getirdiği ana avantajlarını göstermek ve diğer uygulama alanlarını ortaya çıkarmak için aero-termal motor modeline çeşitli kontrol ve arıza senaryoları uygulanmıştır.

Anahtar Kelimeler: Turbojet Motor Simulasyonu, Hızlı Motor Modeli, Çevrimiçi Sistem Tanımlama, Model Referans Adaptif Kontrol







*To my parents...*

## ACKNOWLEDGMENTS

First, I would like to express my deepest gratitude to my advisor Assoc. Prof. Dr. İlkey Yavrucuk for providing me a professional work environment and for guiding me to choose the right one from the beginning.

And, I would like to thank Prof. Dr.-Ing. Florian Holzapfel and Dipl.-Ing., M.Sc. Christoph Göttlicher for their guidance, valuable suggestions and criticism during my visiting research at the Institute of Flight System Dynamics, Technical University of Munich.

Then, I want to specially thank Prof. Dr. Oğuz Uzol for inspiring me to work on gas turbine control systems.

Next, I would like to thank my thesis committee members, Prof. Dr. Metin U. Salamcı and Asst. Prof. Dr. Ali Türker Kutay for their valuable feedback and comments during committee meetings.

Also, I am appreciated to my friends Dr. Gönenç Gürsoy and Serdar Üşenmez for their suggestions and efforts related to adaptive and fuzzy logic control.

Last, I am also grateful to my family for their endless support and love.

## TABLE OF CONTENTS

ABSTRACT . . . . .	v
ÖZ . . . . .	vii
ACKNOWLEDGMENTS . . . . .	x
TABLE OF CONTENTS . . . . .	xi
LIST OF TABLES . . . . .	xiv
LIST OF FIGURES . . . . .	xv
LIST OF ABBREVIATIONS . . . . .	xix
LIST OF SYMBOLS . . . . .	xx

### CHAPTERS

1	INTRODUCTION . . . . .	1
1.1	Small Turbojet Engines and the Fuel Systems . . . . .	2
1.2	Definition of the Problem . . . . .	6
1.3	Contributions of This Thesis . . . . .	6
1.4	Outline . . . . .	7
2	TURBOJET ENGINE MODEL . . . . .	9
2.1	Aero-Thermal Turbojet Engine Model . . . . .	10
2.1.1	Intake . . . . .	12

2.1.2	Compressor . . . . .	12
2.1.3	Compressor Plenum . . . . .	14
2.1.4	Burner . . . . .	14
2.1.5	Turbine . . . . .	15
2.1.6	Jet Pipe Plenum . . . . .	17
2.1.7	Nozzle . . . . .	17
2.1.8	Shaft Dynamics . . . . .	18
2.2	Gear-Type Fuel Pump Model . . . . .	18
2.3	Aero-Thermal Turbojet Engine Model Validation . . . . .	21
2.3.1	Steady-State Results . . . . .	21
2.3.2	Transient Results . . . . .	24
3	OFFLINE SYSTEM IDENTIFICATION . . . . .	27
3.1	Fast Engine Model Structure . . . . .	28
3.2	Derivation of the Offline Estimation Algorithm . . . . .	30
3.3	Offline Parameter Estimation of an Aero-Thermal Model . . . . .	32
3.4	Offline Parameter Estimation of a Test Engine . . . . .	36
4	ONLINE SYSTEM IDENTIFICATION . . . . .	41
4.1	Derivation of the Online Estimation Algorithm . . . . .	41
4.2	Verification of the Online Estimation Algorithm . . . . .	47
4.3	Online Parameter Estimation of an Aero-Thermal Model . . . . .	52
5	ADAPTIVE CONTROL OF SMALL TURBOJET ENGINES . . . . .	55
5.1	Indirect Model Reference Adaptive Control . . . . .	56
5.2	Verification of the Indirect-MRAC Algorithm . . . . .	60

5.3	Testing of the Derived Indirect-MRAC . . . . .	66
5.4	Testing of the Obtained Nonlinear Controller . . . . .	72
6	ADVANTAGES AND DISCUSSIONS . . . . .	75
7	CONCLUSION . . . . .	81
	REFERENCES . . . . .	83
A	AMT OLYMPUS TURBOJET ENGINE SPECIFICATIONS . . . . .	89
B	GENERAL PROCEDURE FOR FINDING AN APPROPRIATE NON- LINEAR MODEL STRUCTURE . . . . .	91
	CURRICULUM VITAE . . . . .	97

## LIST OF TABLES

### TABLES

Table A.1 Technical Specifications of the AMT Olympus Turbojet Engine [14] 89



## LIST OF FIGURES

### FIGURES

Figure 1.1	J402-CA-400 Fuel Metering Unit [3] . . . . .	3
Figure 1.2	Cutaway View of Teledyne CAE 373-8 RPV Engine Control System [6] . . . . .	4
Figure 1.3	Block Diagram of Teledyne CAE 373-8 RPV Engine Control System [6] . . . . .	4
Figure 1.4	Gear-Type Fuel Pump Prototype for STEs . . . . .	5
Figure 2.1	Turbojet Engine with ECU . . . . .	10
Figure 2.2	Block Diagram of the Aero-Thermal Turbojet Engine Model . . . . .	11
Figure 2.3	Compressor Performance Maps for Mass Flow [14] . . . . .	13
Figure 2.4	Compressor Performance Maps for Efficiency [14] . . . . .	13
Figure 2.5	Turbine Performance Map for Mass Flow . . . . .	16
Figure 2.6	Turbine Performance Map for Efficiency . . . . .	16
Figure 2.7	Gear-Type Fuel Pump . . . . .	19
Figure 2.8	Fuel Pump Test Results . . . . .	19
Figure 2.9	3D Look-Up Table of the Gear-Type Fuel Pump . . . . .	20
Figure 2.10	Compressor Outlet Pressure Comparison with Ref. [14] . . . . .	22
Figure 2.11	EGT Comparison with Ref. [14] . . . . .	22

Figure 2.12 Fuel Flow Rate Comparison with Ref. [14] . . . . .	23
Figure 2.13 Thrust Comparison with Ref. [14] . . . . .	23
Figure 2.14 Compressor Outlet Pressure ( $P_3$ ) Response of the Aero-Thermal Model . . . . .	24
Figure 2.15 Turbine Outlet Pressure Response ( $P_5$ ) of the Aero-Thermal Model	24
Figure 2.16 Burner Temperature Response ( $T_4$ ) of the Aero-Thermal Model . .	25
Figure 2.17 Shaft Speed Response ( $N$ ) of the Aero-Thermal Model . . . . .	25
Figure 3.1 Turbojet Engine with a Gear-Type Fuel Pump . . . . .	28
Figure 3.2 Aero-Thermal Model Response to Voltage Inputs . . . . .	29
Figure 3.3 Aero-Thermal Model Response to the Stairs Level of Fuel Flow Rate Input . . . . .	33
Figure 3.4 State Comparison of the Models . . . . .	34
Figure 3.5 Comparison of the Test Results for an Applied Square Wave Command . . . . .	35
Figure 3.6 Comparison of the Test Results for an Applied Sinusoidal Command	35
Figure 3.7 Test-Bed with a Turbojet Engine and ECU [8] . . . . .	36
Figure 3.8 Turbojet Engine Response to the Stairs Level Fuel Flow Rate Input	37
Figure 3.9 Comparison of the Smoothed Data with the Raw Data and the Derived Shaft Acceleration . . . . .	37
Figure 3.10 Comparison of the Fast Engine Model Output with the Turbojet Engine Data . . . . .	38
Figure 4.1 Online Parameter Estimation Structure [33] . . . . .	42
Figure 4.2 Detailed View of the Parameter Estimation Structure . . . . .	44



Figure 4.3	Online Parameter Estimation Structure for the Fast Engine Model . . . . .	48
Figure 4.4	Shaft Speed Estimation Result of the Fast Engine Model . . . . .	49
Figure 4.5	Shaft Acceleration Estimation Result of the Fast Engine Model . . . . .	50
Figure 4.6	Parameter Estimation Results of the Fast Engine Model . . . . .	51
Figure 4.7	Online Parameter Estimation Structure for the Aero-Thermal Model . . . . .	53
Figure 4.8	Shaft Speed Estimation Result of the Aero-Thermal Model . . . . .	53
Figure 4.9	Shaft Acceleration Estimation Result of the Aero-Thermal Model . . . . .	54
Figure 4.10	Parameter Estimation Results of the Aero-Thermal Model . . . . .	54
Figure 5.1	General Structure of an Indirect-MRAC . . . . .	56
Figure 5.2	Detailed Structure of the Indirect-MRAC . . . . .	57
Figure 5.3	Detailed Structure of the Indirect-MRAC with Controller Calculation . . . . .	59
Figure 5.4	Detailed Structure of the Indirect-MRAC for Verification . . . . .	61
Figure 5.5	Indirect-MRAC Verification Result . . . . .	62
Figure 5.6	Indirect-MRAC Verification Result, Close View (first 20 s.) . . . . .	63
Figure 5.7	Indirect-MRAC Verification Result, Close View (first 70 s.) . . . . .	63
Figure 5.8	Indirect-MRAC Fast Engine Model Parameter Estimations . . . . .	65
Figure 5.9	Indirect-MRAC Fast Engine Model Controller Gains . . . . .	65
Figure 5.10	Detailed Structure of the Indirect-MRAC for Test . . . . .	67
Figure 5.11	Indirect-MRAC Test Result . . . . .	68
Figure 5.12	Indirect-MRAC Test Result (first 20 s.) . . . . .	69
Figure 5.13	Indirect-MRAC Test Result (first 70 s.) . . . . .	69
Figure 5.14	Indirect-MRAC Test Result (last 50 s.) . . . . .	70

Figure 5.15 Indirect-MRAC Aero-Thermal Model Parameter Estimations . . . . .	70
Figure 5.16 Indirect-MRAC Aero-Thermal Model Controller Gains . . . . .	71
Figure 5.17 Nonlinear Controller Performance Test-1 . . . . .	72
Figure 5.18 Nonlinear Controller Performance Test-2 . . . . .	73
Figure 5.19 Nonlinear Controller Performance Test-3 . . . . .	73
Figure 6.1 Comparison Scenario-1 . . . . .	76
Figure 6.2 Comparison Scenario-2 . . . . .	76
Figure 6.3 Failure Scenario, Shaft Speed Results . . . . .	77
Figure 6.4 Failure Scenario, Controller Gains . . . . .	78
Figure 6.5 Failure Scenario, Control Effectiveness . . . . .	79
Figure A.1 Cutaway View of the AMT Olympus Turbojet Engine [15] . . . . .	89
Figure B.1 First-Order Linear Model Output Comparison with Aero-Thermal Model Data . . . . .	92
Figure B.2 First-Order Non-Linear Model Output Comparison with Aero-Thermal Model Data (with a linear K gain function) . . . . .	94
Figure B.3 First-Order Non-Linear Model Output Comparison with Aero-Thermal Model Data (with a second-order K gain polynomial) . . . . .	95

## LIST OF ABBREVIATIONS

### Acronyms

DC	Direct current
DEEC	Digital electronic engine control
ECU	Engine control unit
EGT	Exhaust gas temperature
EPR	Engine pressure ratio
FADEC	Full authority digital engine control
FDI	Failure detection and isolation
FMU	Fuel metering unit
HP	High pressure pump
HMC	Hidromechanical control
IGV	Inlet guide vane
JP8	Jet propellant 8
LP	Linear Part
MRAC	Model reference adaptive control
NLP	Nonlinear Part
PI	Proportional integral
PID	Proportional integral derivative
RPM	Revolution per minute
STC	Self-tuning control
STE	Small Turbojet Engine
VSV	Variable stator vane

## LIST OF SYMBOLS

### Symbols, Engine

$A$	Area, $m^2$
$C_p$	Specific heat at constant pressure, $J/kgK$
$F$	Thrust, $N$
$g$	Mass flow rate, $kg/s$
$h$	Specific enthalpy, $J/kg$
$J$	Rotor assembly inertia, $m^3$
$LHV$	Lower heating value, $J/kg$
$M$	Mach number
$N$	Shaft speed, $rpm$
$P$	Pressure, $Pa$
$P_{wr}$	Power, $W$
$R$	Gas Constant, $J/kgK$
$T$	Temperature, $K$
$U$	Air speed, $m/s$
$V$	Volume, $m^3$
$\beta$	Pressure ratio
$\delta$	$P_0/P_{std}$
$\eta$	Efficiency
$\theta$	$T_0/T_{std}$
$\tau$	Time constant, s
$\gamma$	Specific heats ratio

## Subscripts, Engine

<i>0</i>	Ambient conditions
<i>1...7</i>	Engine section numbers
<i>b</i>	Burner
<i>c</i>	Compressor
<i>com</i>	Command
<i>cor</i>	Corrected
<i>cri</i>	Critical
<i>f</i>	Fuel
<i>is</i>	Isentropic
<i>jp</i>	Jet pipe
<i>loss</i>	Loss
<i>m</i>	Mechanical
<i>max</i>	Maximum
<i>meas</i>	Measured
<i>n</i>	Nozzle
<i>p</i>	Plenum
<i>std</i>	Standard day conditions
<i>t</i>	Turbine

## Symbols, Other

$A$	System matrix
$B$	Input vector
$e$	Error
$f$	Function
$I$	Identity matrix
$J$	Cost function
$K$	Gain
$k$	Discrete sample number
$N$	Shaft speed
$P$	Positive definite matrix
$Q$	Positive definite matrix
$u$	Input
$V$	Voltage
$X$	Regressor
$x$	State
$Y$	Dependent variable
$y$	Output
$\alpha$	Polynomial coefficients
$\Gamma$	Learning gain
$\Delta$	Difference
$\epsilon$	Error, residual
$\zeta$	Damping ratio
$\Theta$	Parameter
$\theta$	Parameters unknown vector
$\Lambda$	Control effectiveness

$\lambda$	Root
$\omega_n$	Natural frequency, <i>rad/s</i>

**Subscripts, Other**

0	Initial
<i>i</i>	Index
<i>I</i>	Identification
<i>m</i>	Model
<i>max</i>	Maximum
<i>p</i>	Plant





## CHAPTER 1

### INTRODUCTION

Today, gas turbine engines are the primary source of propulsive power for aircraft due to their high efficiency and reliability. Gas turbine control and diagnostic technologies are among the most important factors in achieving these levels of efficiency and reliability.

The first turbojet engines were designed around eighty years ago by Hans von Ohain from Germany and Sir Frank Whittle from the UK, independently from each other. The control systems of these first engines were mostly mechanical. Simple linkages, gear trains, and cams were used to adjust and limit the fuel flow. After the 1950s, hydromechanical controls (HMCs), also known as governors, were introduced. These control systems consisted of a metering valve to adjust the fuel flow proportional to the difference between the desired speed and the actual speed of the engine. There were also some mechanical limitations on the fuel system to prevent the engine from the flame-out and over-temperature. In the late 1950s, the engine performances were increased enormously with the engine design technology advancements including high-compression ratio compressors and high-bypass-flow turbofans. The related control technology also became more complex with the variable geometry controls, such as inlet guide vane (IGV), variable stator vane (VSV), and nozzle geometry control. And in late 1960, the HMCs and its subsystems reached their practical limitations due to the cost and weight constraints. Thus, in the early 1970s, with the development in the digital electronic technologies, analog and digital electronic control units (ECU) were introduced to provide high-level supervisory or trim control. The main functions of these ECUs were to calculate speed or temperature set points throughout the engine operation envelope [1].

In 1972, The first full-authority ECU was introduced into service on TFE731 engine. Briefly, an ECU is called "full-authority" if it controls all the engine operations from start-up to shut-down according to the power request without giving a manual override permission to the pilot. The first full-authority ECU had a single channel analog control, which includes main functions such as fail-safe operation, unrestricted power lever movement, no-throttle dead-band and automatic flat rating for the thrust. Then, the analog full-authority ECUs were evolved into FADECs (Full Authority Digital Engine Control) due to the apparent advantages of digital electronics such as ability to do complex calculations, easy update with the embedded software, and more accurate control adjustment. In 1981, the DEEC (Digital electronic engine control) of Pratt-Whitney F100 engine became the first FADEC to be flight tested. For the past 40 years, FADECs have been the standard engine control system for the jet-propelled aircraft. Today's FADECs, when compared with the first developed FADECs, they do not only control the engine throughout its operational range but also perform much more complex operations to improve engine performance and diagnostics [1].

### **1.1 Small Turbojet Engines and the Fuel Systems**

The sub-class small turbojet engines (STEs) are becoming popular among the hobbyist day by day. Besides to power model airplanes; it is used to sustain sailplanes and to power jetpacks, wingsuits, and hoverboards [2]. These engines have a very simple structure with an ECU and a fuel system to reduce the complexity, weight, and cost. The main components of these type engines are a single stage centrifugal compressor, an annular combustor, a single stage axial turbine, and a convergent nozzle. Only shaft speed and Exhaust Gas Temperature (EGT) values are measured by the ECU to govern the shaft speed and to limit the EGT. Despite the maturity and reliability of Fuel Metering Units (FMU), simple gear-type fuel pumps are preferred in such sub-class STEs.

The main function of a fuel system is to adjust the fuel flow rate required to start, accelerate and stabilize the engine under all operating conditions. High precision is necessary not only to maintain the shaft speed under varying load and ambient conditions but also to protect the engine from the excessive exhaust gas temperatures

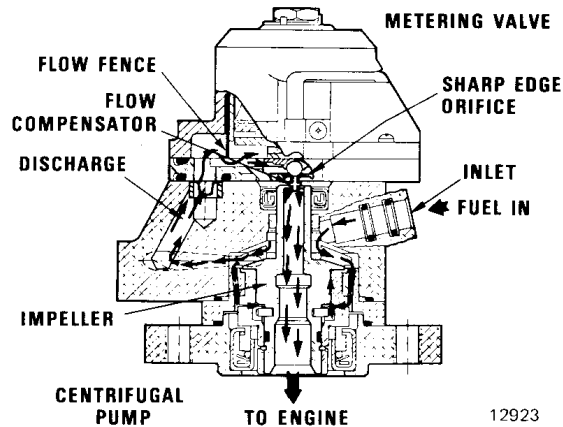


Figure 1.1: J402-CA-400 Fuel Metering Unit [3]

and compressor surge. To achieve this, mostly FMUs are used.

An FMU is generally based on three components: a gear pump, a metering valve, and a bypass valve or a differential pressure valve. Briefly, the gear pump pressurizes the fuel, the differential pressure valve keeps the fuel pressure difference between the FMU inlet and outlet constant, and the metering valve controls the fuel flow by adjusting the fuel flow area. These main components are fixed for almost all FMU designs, but their architectures may vary [4, 5].

As an example of FMU usage on small gas turbine engines, the FMU of the J402-CA-400 turbojet engine is illustrated in Fig. 1.1. The J402-CA-400 engine is a simple small-scale turbojet engine designed for the Harpoon missile. This engine was derived from the J69-T-406 turbojet engine and it is aerodynamically a 32% scale of the J69 parent engine [3].

As another example, the cutaway view of the Teledyne CAE 373-8 engine control unit is shown in Fig. 1.2. This engine is designed specially for target drones [6]. As seen in the figure, it has a very compact design that includes an alternator, a fuel metering unit and a digital electronic control unit. To clarify the working principle, its block diagram is illustrated in Fig. 1.3.

In Fig. 1.3, the pump, also referred as high-pressure (HP) pump, is a gear-type fuel pump. It is mounted on the same shaft with the alternator and driven by the engine

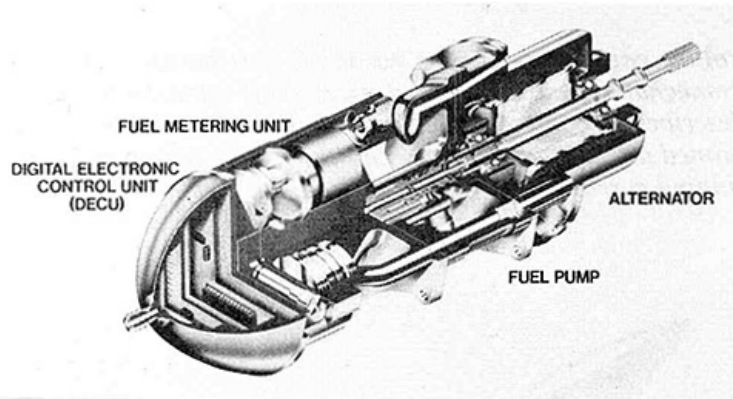


Figure 1.2: Cutaway View of Teledyne CAE 373-8 RPV Engine Control System [6]

shaft. The HP pump pressurizes the fuel supplied from the low-pressure (LP) pump and feeds it to the metering valve. Here, the metering valve is directly driven by a stepper motor, and it adjusts the fuel flow rate by changing the fuel flow area. The differential pressure valve, which is the sub-part of the FMU, keeps the differential pressure constant on the FMU by spilling the excessive flow back to the HP inlet. This constant pressure difference ensures the metering valve to adjust the fuel flow rate proportionally (linearly) respect to the fuel flow cross-section area and also independently from the nozzle pressure.

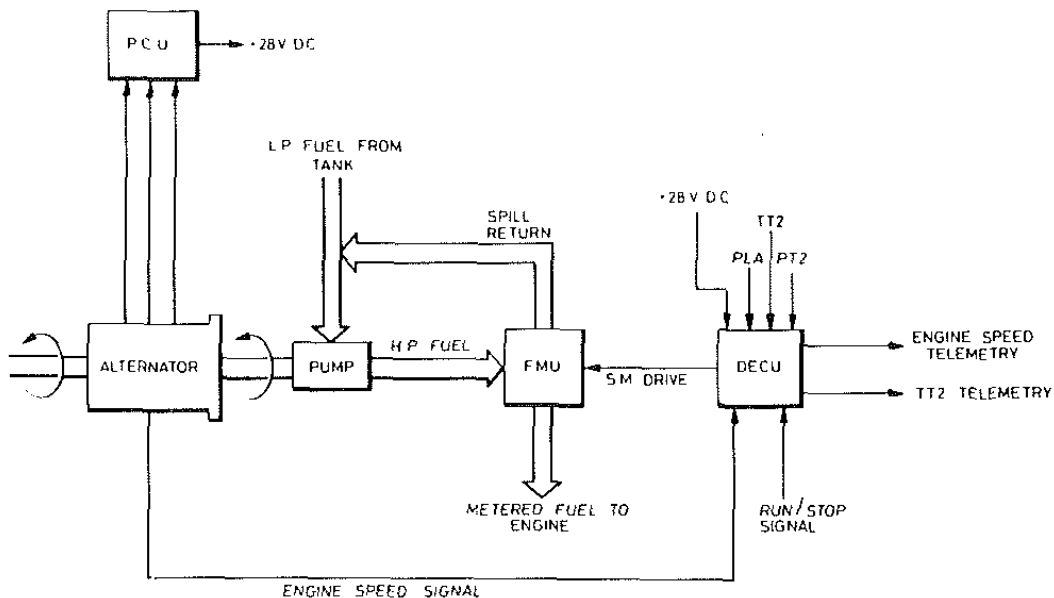
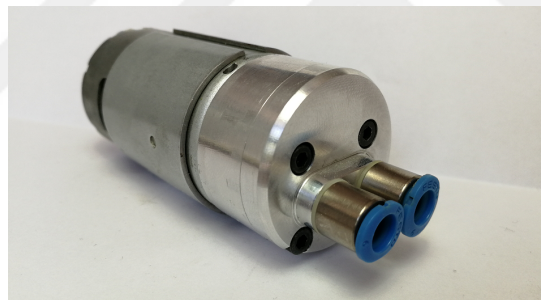


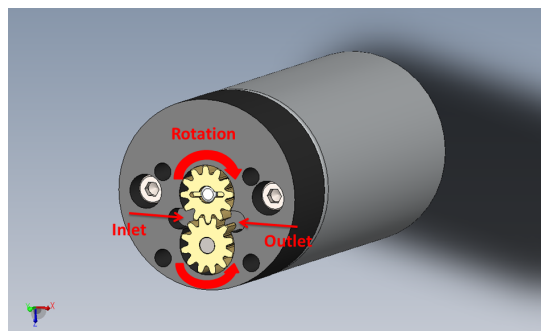
Figure 1.3: Block Diagram of Teledyne CAE 373-8 RPV Engine Control System [6]

However, in low-cost STEs, only a simple gear-type fuel pump is used rather than an FMU. Fig. 1.4a shows the prototype of a gear-type fuel pump designed for small gas turbine control applications. This prototype was previously used in our test beds for gas turbine control studies [7, 8].

The cross-sectional view of the fuel pump is illustrated in [Fig. 1.4b]. As seen in the figure, two meshed gears turn inside a metal housing. One of the meshed gears is driven by a DC motor. Here, the rotation of the gears creates a positive displacement and the fuel fills the space between the housing and outer circumference of the gears. Then, the fuel travels towards the pump's outlet by the gear rotation. However, the leakage between the meshed gears and the housing is unavoidable because of the manufacturing tolerances and wear on the parts, so the fuel leaks inherently from the high-pressurized section (pump outlet) to the low-pressurized section (pump-inlet) depending on the outlet pressure. This causes the gear-type fuel pump to behave nonlinearly under the varying outlet pressure conditions. Also, this shows us the importance of the differential pressure valve used in FMUs.



(a) Gear-Type Fuel Pump



(b) Cutaway View

Figure 1.4: Gear-Type Fuel Pump Prototype for STEs

## **1.2 Definition of the Problem**

The performances of two similar engines are not the same, due to the manufacturing tolerances and material properties. In addition, the engine components deteriorate by time due to the harsh operating conditions. Erosion, wear and tear on the engine components degrade the engine performance slowly. Moreover, replacement of the engine component after the overhaul or repairing process or failure of a component during the engine operation causes a sudden change in the engine performance. All these possible scenarios are the major challenges that must be taken into consideration in an engine control and diagnostic system design.

For advanced engine control and diagnostic applications, fast/online engine models that are able to embed into FADECs are used [1]. These online models adapt itself to the actual engine condition even with deterioration. By this way, they provide very useful data for advanced engine control and diagnostic applications, such as limit detection and protection, Failure Detection and Isolation (FDI), and model-based engine controllers.

In literature, mostly, linear or piecewise-linear techniques are used to obtain fast/online engine models [1, 9, 10]. However, these methods are not directly applicable to the low-cost STEs because of their nonlinear fuel actuation systems. The incorporation of such type of fuel flow actuation devices introduces additional nonlinearities into the modeling and control of the STEs and this makes the traditional methods inappropriate.

## **1.3 Contributions of This Thesis**

The focus of this thesis is on small low-cost turbojet engines where the fuel flow is provided by a gear-type fuel pump rather than a more traditional fuel metering unit. This thesis presents and applies online/offline parameter estimation and adaptive control methods to this type sub-class turbojet engines. The contributions of this thesis study may be summarized as follows:

- The online/fast engine models should be simple in structure and consistent with the engine dynamics. In this study, these models are kept simple to be able to run on even microcontroller based ECUs and are kept complex enough to be able to capture the additional nonlinear dynamics caused by the gear type-fuel pump.
- Due to the manufacturing tolerances, the performances of the similar type of engines and gear pumps are not the same. Even, the fuel pump replacement causes a sudden change in the engine performance. The proposed fast engine model can adapt itself to the actual engine and fuel pump combination in a short time. This can eliminate the necessary controller calibration tests.
- Wearing on the fuel pump gears or erosion on the compressor/turbine blades cause the engine performance to degrade slowly. This engine model can update itself with the actual engine condition during the flight and still can be used for the limit detection and protection. The updated engine parameters can also be used for health monitoring and diagnostics purposes.
- This sub-class turbojet engines are instrumented mostly with inductive type proximity sensors for the shaft speed measurement without a redundancy option. The performance of these type sensor heavily depends on the clearance between the compressor blades. Also, they are inherently susceptible to magnetic field interferences. The proposed fast engine model can provide software redundancy and can be used for failure detection and isolation (FDI) purposes.
- Also, any degradation on the turbojet engine or on the fuel pump directly affects the controller performance. The proposed adaptive control method using the fast engine model can update itself to actual engine dynamics and recovers the desired turbojet response.

## **1.4 Outline**

Chapter 2 is where a high-fidelity aero-thermal turbojet engine model is developed. In order to achieve a high-fidelity level, the inter-component volumes method was used. Next, a nonlinear gear-type fuel pump model was created by using test data and

integrated with the aero-thermal model. Last, the developed aero-thermal model was verified with experimental data found in the literature.

Chapter 3 proposes a nonlinear approximate model (or a fast engine model) for the shaft dynamics simulation. The least squares method was used for the parameter estimation of the approximate model. The obtained model was then tested under different fuel pump command scenarios. Last, the same identification procedure was repeated with real engine data to verify the proposed model structure and the derived identification method.

Chapter 4 derives an online estimation algorithm which uses the same approximate model structure. The convergence and boundedness of the parameter update laws were proved by using Lyapunov stability theory. The algorithm was first applied to the approximate model and then verified on the aero-thermal turbojet model.

Chapter 5 introduces an indirect-model reference adaptive control (indirect-MRAC) for the shaft speed control of STEs. The adaptive controller again uses the same approximate model structure and the derived online parameter estimation algorithm. Firstly, the controller gain update laws was derived. Then, the algorithm was applied to both approximate and aero-thermal models.

Chapter 6 compares the developed indirect-MRAC with a classical controller under various test conditions. Last, both controllers were tested under a failure scenario to reveal the main advantages of the indirect-MRAC.



## CHAPTER 2

### TURBOJET ENGINE MODEL

In this study, the AMT Olympus turbojet engine was chosen as the test case [11]. This engine is designed for model aircraft, high-speed aerial target drones, and heat/power generators. It is a very basic type of a turbojet engine comprising a standard inlet, a single stage centrifugal compressor with vaned diffusers, an annular combustor, a single stage axial turbine, and a convergent nozzle. The cutaway view and technical specifications of the engine are given in Appendix A.

The control system of the engine is also very simple. A microcontroller based ECU is used to control the shaft speed and to limit the EGT. To manipulate the fuel flow rate, only the gear type fuel pump is used instead of a more traditional FMU.

The shaft speed control structure of the AMT turbojet engine is illustrated in Fig. 2.1. Here, the ECU receives the shaft speed command and engine's actual shaft speed measurement (feedback) and then, generates the actuation voltage required for the gear-type fuel pump. The fuel flow rate of the pump depends on the actuation voltage and the compressor outlet pressure. Last, the supplied fuel is burned in the combustion chamber and the generated energy transformed into the thrust.

However, the generated thrust of a turbojet engine is not a measurable quantity. It is a function of the shaft speed, compressor inlet conditions, and aircraft speed. But, as seen in Fig. 2.1, the shaft speed is the only parameter that can be controlled within these parameters to achieve the desired thrust. For this reason, the fuel pump supply voltage and shaft speed are defined as the input and output of the system, respectively. In Fig. 2.1, the red dashed line defines the propulsion system in which this study is interested. To simulate this system, a generic aero-thermal turbojet engine model with

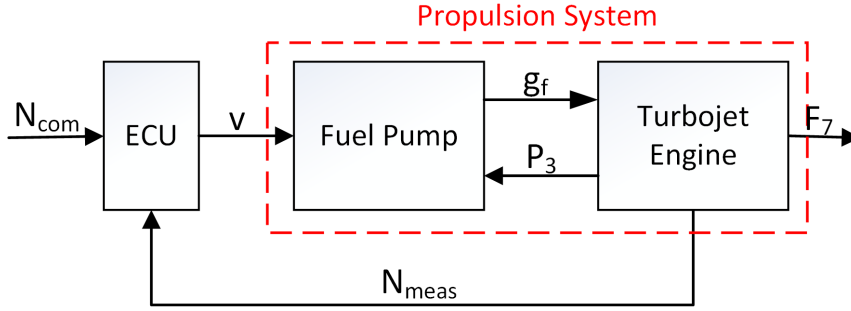


Figure 2.1: Turbojet Engine with ECU

a gear-type fuel pump is developed in the following sections.

## 2.1 Aero-Thermal Turbojet Engine Model

A turbojet engine is a complex and inherently nonlinear machine. A good high-fidelity aero-thermal model, which can simulate the transient response as well as the steady-state condition of the target engine, is important for the system identification and controller development processes. In this study, the inter-component volumes method is preferred to achieve this high-fidelity level [12–21]. In this method, the major components of a gas turbine are modeled separately as a one-dimensional flow device by using the laws of conservation of mass and energy. Each component is also assumed to be in quasi-steady state condition. By this way, it is possible to use quasi-steady state performance maps in compressor and turbine models. For the sake of simplicity, the compressor and turbine are also considered as a volumeless component so, a plenum is placed to their behind to maintain the unsteady mass balance within the engine. In addition, the lumped-parameter approach is preferred for the physical properties of the air. Which means, any variations of the specific heat of the air are either represented in the definition of isentropic efficiency or neglected. Lastly, the specific heat value at constant pressure ( $C_p$ ) is obtained from a 4th-order polynomial of the temperature. The temperature value required for this polynomial is obtained from the previous time step.

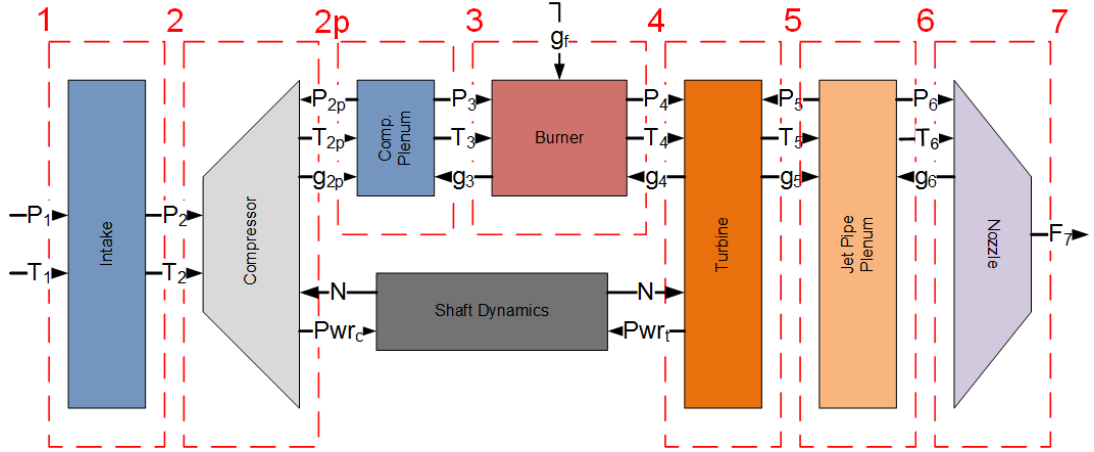


Figure 2.2: Block Diagram of the Aero-Thermal Turbojet Engine Model

The paper published by Rahman [14] was used as the reference for the compressor/turbine maps and the other parameters of the AMT Olympus turbojet engine. The experimental data published in this reference was also used for the validation of the developed simulation model.

Figure 2.2 depicts the block diagram of the turbojet engine's simulation model. In this figure, the major engine components are illustrated by the blocks. Here, the red dashed lines denote the control volumes and stations where the thermodynamic state of the air must be considered and, the arrows represent the data flow between the control volumes. The parameters of the state vector and input required to define the engine dynamics are chosen as

$$x = [ P_3, P_5, T_4, N ]^T \quad (2.1)$$

where  $P_3$  and  $P_5$  is the air pressure at the compressor and the turbine outlet, respectively,  $T_4$  is the air temperature at the turbine inlet, and  $N$  is the rotational speed of the engine shaft, and

$$u = g_f \quad (2.2)$$

defines the input of the engine dynamics, which is the mass flow rate of the fuel ( $g_f$ ).

### 2.1.1 Intake

The pressure and temperature at the intake entrance ( $P_1, T_1$ ) are considered equal to the ambient conditions ( $P_0, T_0$ ):

$$P_1 = P_0 \quad (2.3)$$

$$T_1 = T_0 \quad (2.4)$$

The intake is assumed to be an ideal component so, the energy and pressure losses along the intake are ignored. The stagnation quantities ( $P_2, T_2$ ) at the intake outlet can be obtained from the following equations [22–24]:

$$P_2 = P_1 \left( \left( \frac{T_2}{T_1} \right)^{\frac{\gamma}{\gamma-1}} \right) \quad (2.5)$$

$$T_2 = T_1 \left( 1 + \frac{\gamma-1}{2} M_0^2 \right) \quad (2.6)$$

### 2.1.2 Compressor

To use the steady-state compressor maps during transient conditions, the compressor is considered as a volumeless and quasi-steady state component. In Fig. 2.3 and Fig. 2.4, the compressor steady-state pressure ratio ( $\beta_c = P_{2p}/P_2$ ) and isentropic efficiency ( $\eta_{is,c}$ ) maps as a function of the corrected mass flow rate ( $g_{2p,cor} = g_{2p}\sqrt{\theta}/\delta$ ) and corrected shaft speed ( $N_{cor} = N/\sqrt{\theta}$ ) are presented, respectively. These maps are digitized and converted to the 2D lookup tables as functions of the pressure ratio and corrected shaft speed in order to calculate the corrected mass flow rate and isentropic efficiency at the compressor outlet. For simplicity, the linear interpolation method is used to evaluate these functions given below:

$$g_{2p,cor} = f_1(\beta_c, N/\sqrt{\theta}) \quad (2.7)$$

$$\eta_{is,c} = f_2(g_{2p,cor}, N/\sqrt{\theta}) \quad (2.8)$$

where  $\delta, \theta$  are defined as:

$$\delta = \frac{P_2}{P_{std}}, \quad \theta = \frac{T_2}{T_{std}} \quad (2.9)$$

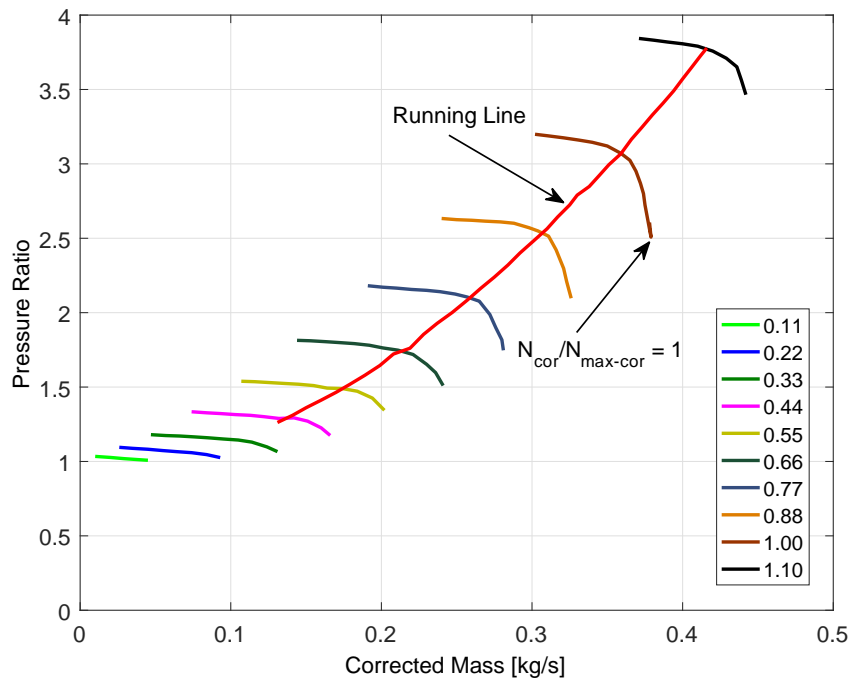


Figure 2.3: Compressor Performance Maps for Mass Flow [14]

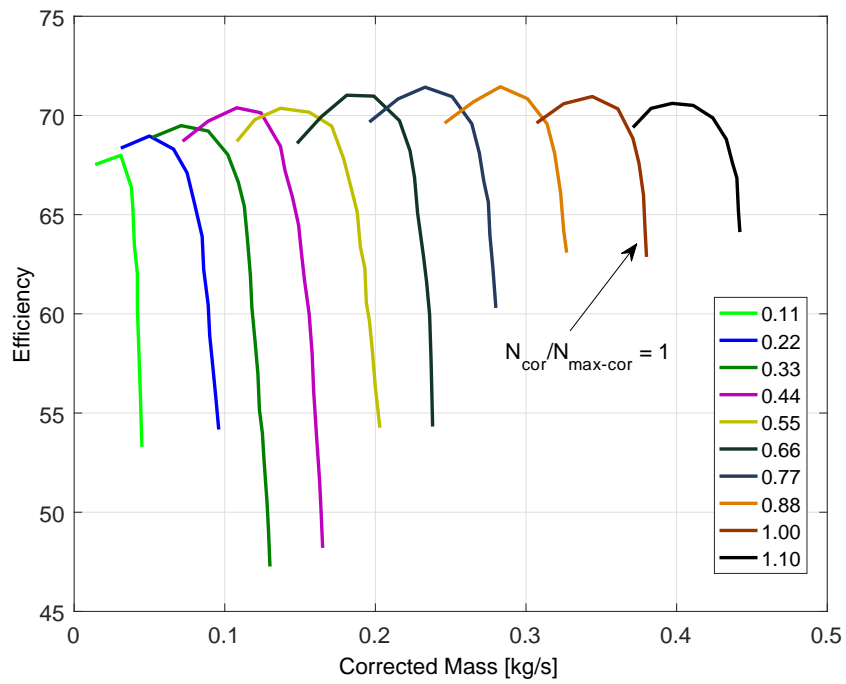


Figure 2.4: Compressor Performance Maps for Efficiency [14]

Also, the total temperature at the compressor outlet is [22]:

$$T_{2p} = T_2 \left( 1 + \frac{1}{\eta_{is,c}} \left( \left( \frac{P_{2p}}{P_2} \right)^{\frac{\gamma-1}{\gamma}} - 1 \right) \right) \quad (2.10)$$

where the specific heat ratio ( $\gamma$ ) is evaluated from the arithmetic average of the inlet ( $T_2$ ) and the outlet ( $T_{2p}$ ) temperatures. Last, the power consumption of the compressor is [22]:

$$Pwr_c = g_{2p}(C_{p2}T_2 - C_{p2p}T_{2p}) \quad (2.11)$$

### 2.1.3 Compressor Plenum

To provide the unsteady mass balance between the compressor and burner, a plenum is placed after the compressor outlet. The rate of change of the pressure in the plenum is derived from the ideal gas law. The simplified version of this equation is given as follows [1, 25]:

$$\frac{dP_{2p}}{dt} = \frac{RT_{2p}}{V_{p,c}}(g_{2p} - g_3) \quad (2.12)$$

In addition, the energy and pressure losses are also neglected so, the air pressure and temperature are assumed to be constant along the plenum:

$$P_3 = P_{2p} \quad (2.13)$$

$$T_3 = T_{2p} \quad (2.14)$$

### 2.1.4 Burner

The burner is considered to be a pure energy accumulator. The pressure loss ( $\eta_{loss}$ ) and burning efficiency ( $\eta_b$ ) are taken into account during the calculations. The temperature rate derived from the unsteady energy conservation law is [13]:

$$\tau_b \frac{dT_4}{dt} = \frac{g_3 C_{p3} T_3 + g_f (C_{p,b} T_0 + \eta_b LHV) - g_4 C_{p4} T_4}{g_4 C_{p4}} \quad (2.15)$$

where  $\tau_b$  is the time constant and  $C_{p,b}$  is the specific heat value of the fuel. In addition, it is assumed that the fuel delivered to the burner is at ambient temperature ( $T_0$ ). Last, the mass flow rate at the burner input ( $g_3$ ) is:

$$g_3 = g_4 - g_f \quad (2.16)$$

and the burner outlet pressure ( $P_4$ ) is:

$$P_4 = \eta_{loss} P_3 \quad (2.17)$$

### 2.1.5 Turbine

The assumptions made in the compressor model are also valid for the turbine model. The turbine performance maps (Fig. 2.5, 2.6) obtained from Ref. [14], converted into functions of the turbine expansion ratio ( $\beta_t = P_4/P_5$ ) and non-dimensional shaft speed ( $N/\sqrt{T_4}$ ) to get the non-dimensional mass flow ( $g_{4,non} = g_4\sqrt{T_4}/P_4$ ) and turbine isentropic efficiency ( $\eta_{is,t}$ ):

$$g_{4,non} = f_1(\beta_t, N/\sqrt{T_4}) \quad (2.18)$$

$$\eta_{is,t} = f_2(\beta_t, N/\sqrt{T_4}) \quad (2.19)$$

Furthermore, the turbine outlet temperature can be calculated from the equations given in [22, 23]:

$$T_5 = T_4 \left( 1 + \eta_t \left( \left( \frac{P_5}{P_4} \right)^{\frac{\gamma-1}{\gamma}} - 1 \right) \right) \quad (2.20)$$

where  $\gamma$  is evaluated from the arithmetic average of the inlet ( $T_4$ ) and outlet ( $T_5$ ) temperature. Last, the power ( $Pwr_t$ ) produced by the turbine is calculated from the equation below [22, 23]:

$$Pwr_t = g_4(C_{p5}T_5 - C_{p4}T_4) \quad (2.21)$$

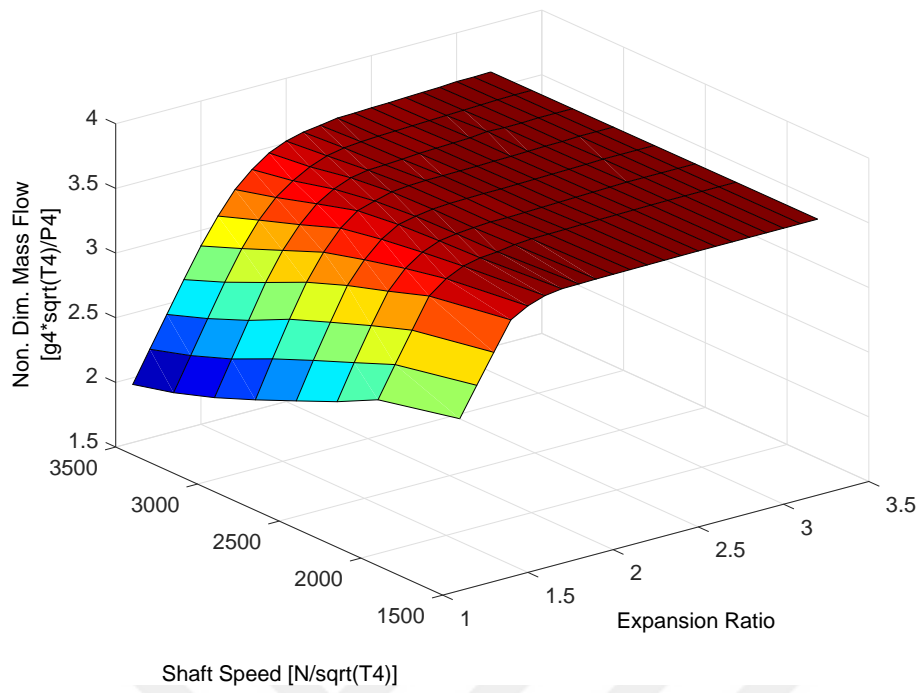


Figure 2.5: Turbine Performance Map for Mass Flow

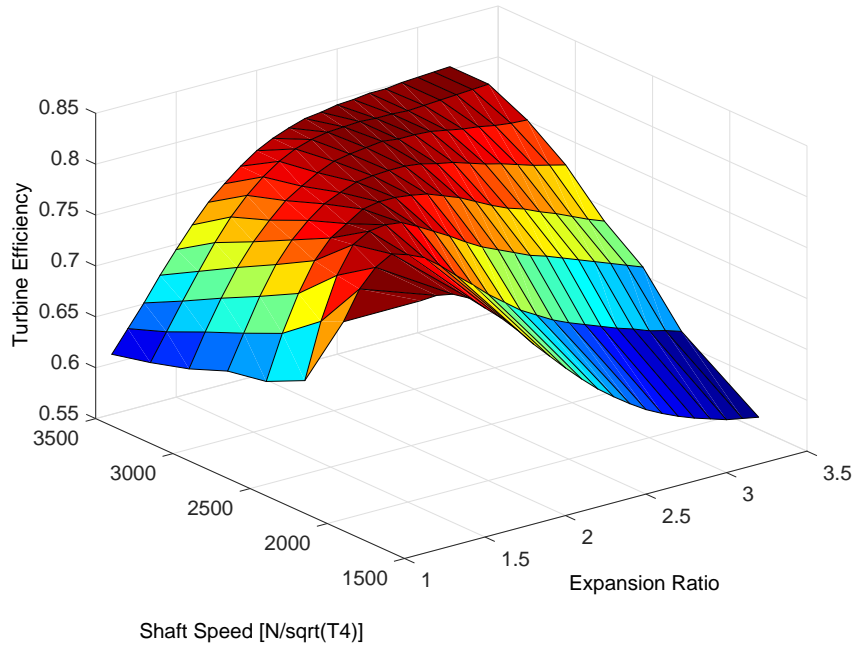


Figure 2.6: Turbine Performance Map for Efficiency



### 2.1.6 Jet Pipe Plenum

Similar to the compressor plenum, this component maintains the unsteady mass balance between the turbine and nozzle. The equations defined in the plenum section can be rearranged as:

$$\frac{dP_5}{dt} = \frac{RT_5}{V_{p,n}}(g_5 - g_6) \quad (2.22)$$

and, the pressure and temperature at the plenum outlet ( $P_6, T_6$ ) are:

$$P_6 = P_5 \quad (2.23)$$

$$T_6 = T_5 \quad (2.24)$$

### 2.1.7 Nozzle

The nozzle is considered as a simple convergent type nozzle. The nozzle pressure ratio ( $\beta_n$ ) is defined as:

$$\beta_n = \frac{P_6}{P_0} \quad (2.25)$$

If the air speed through a nozzle reaches the speed of sound, the nozzle chokes. The pressure ratio at this moment is called the critical pressure ratio ( $(\beta_n)_{cri}$ ). This ratio defines the upper saturation limit of the nozzle. The critical pressure ratio can be expressed as a function of the specific heat ratio:

$$(\beta_n)_{cri} = \left( \frac{2}{\gamma + 1} \right)^{\frac{\gamma}{\gamma-1}} \quad (2.26)$$

The air velocity at a nozzle outlet ( $U_7$ ) as a function of the nozzle pressure ratio and nozzle temperature is [22, 23]

$$U_7 = \sqrt{2C_{p6}T_6\eta_n \left( 1 - \beta_n^{\frac{\gamma-1}{\gamma}} \right)} \quad (2.27)$$

where  $\eta_n$  represents the nozzle efficiency. The mass flow rate through a nozzle ( $g_6$  or  $g_7$ ) can be derived from the continuity equation [22, 23]:

$$g_7 = g_6 = \frac{AP_6}{\sqrt{T_6}} \sqrt{\frac{\gamma}{R}} M_7 \left( 1 + \frac{\gamma-1}{2} M_7^2 \right)^{\frac{1-\gamma}{2\gamma-2}} \quad (2.28)$$

where  $M_7$  is the Mach number of the air jet and can be calculated as:

$$M_7 = \frac{U_7}{\sqrt{\gamma RT_6}} \quad (2.29)$$

Finally, the net thrust ( $F_7$ ) generated by a turbojet engine can be obtained from the velocity and pressure differences at the nozzle outlet:

$$F_7 = g_7(U_7 - U_0) + A_n(P_7 - P_0) \quad (2.30)$$

where  $U_0$  is the aircraft speed.

### 2.1.8 Shaft Dynamics

The equation of the rotational acceleration ( $\dot{N}_{rad/s}$ ) derived from the angular momentum equilibrium is:

$$\dot{N}_{rad/s} = \frac{\eta_m P w r_t - P w r_c}{J N_{rad/s}} \quad (2.31)$$

where  $J$  denotes the total inertia of the rotating assembly of the compressor, turbine, and shaft. The bearing friction and other mechanical losses are implemented as the mechanical loss ( $\eta_m$ ).

## 2.2 Gear-Type Fuel Pump Model

A gear-type fuel pump which was developed in-house for small gas turbines is shown in Fig. 2.7. To get performance values of the designed gear pump, it was tested under the varying outlet pressure with 3V, 6V, and 8V supply voltages at standard day conditions. The JP8 fuel was used during the tests. In each test session, the pump outlet pressure was increased with the help of a valve on the fuel line, and the fuel flow rate and the pump's current were recorded with respect to the pump's outlet gauge pressure.

In Fig 2.8, the fuel pump test results for each of the three supply voltages are given. This contains fuel flow rate versus pump outlet pressure (solid lines) and consumed current versus pump outlet pressure (dashed lines). In addition, a possible fuel pump running line is denoted by the magenta dotted line. As seen in the figure, the fuel pump at a constant supply voltage shows almost a linear behavior with increasing outlet pressure. However, the slope of each test results flattens with increasing supply voltage. Besides, a turbojet engine's fuel demand increases exponentially with respect to the compressor outlet pressure. Therefore, for a ramp up in engine power (or a shaft

speed acceleration), the fuel pump supply voltage needs to be increased against the increasing compressor outlet pressure. This is illustrated in the possible fuel pump running line shown in Figure 2.8, which unveils nonlinear behavior in the fuel pump's operation.

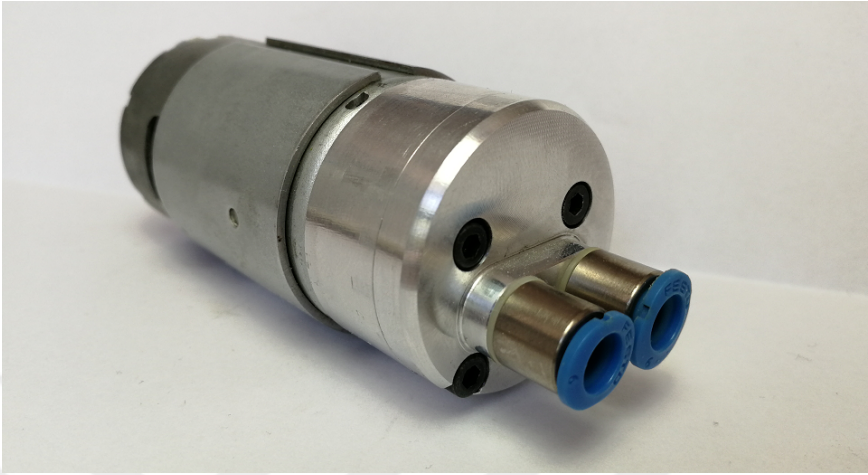


Figure 2.7: Gear-Type Fuel Pump

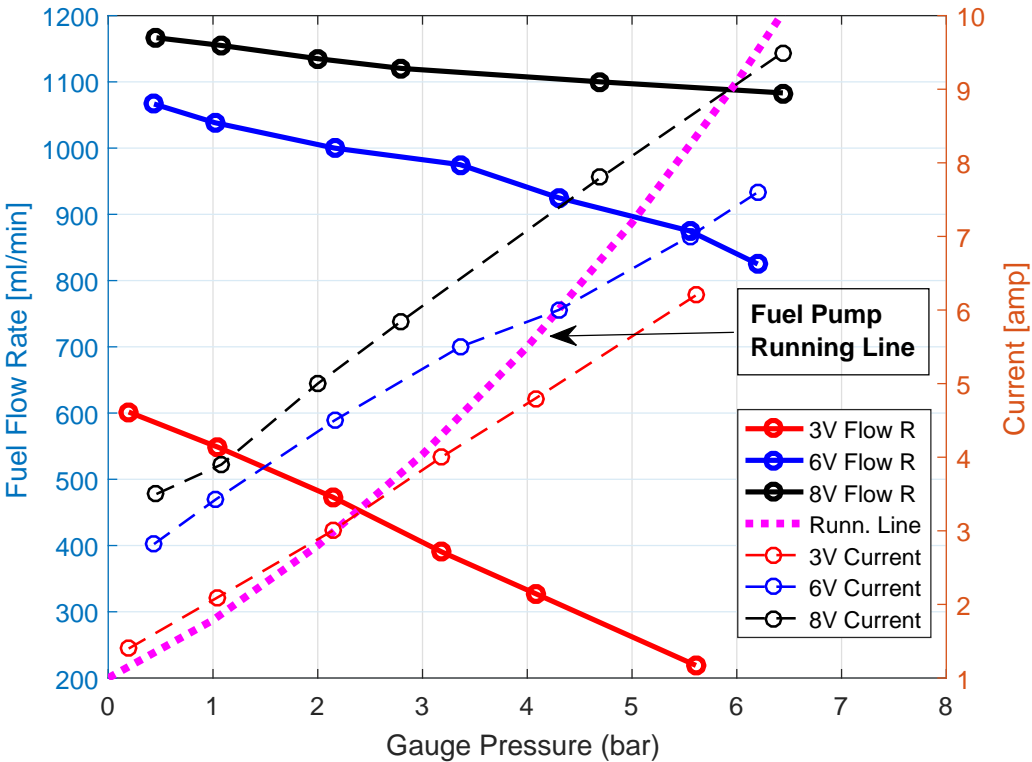


Figure 2.8: Fuel Pump Test Results

In this application, a small direct-current (DC) electrical motor is used to drive the gears of the fuel pump, so its dynamical response can be represented with a first-order transfer function [26]. However, the mechanical time constant of DC motors is around milliseconds ( [27]) and for small turbojet engines, it is around seconds ( [7, 8, 28]). Therefore, the transient (dynamic) response of the gear pump can be neglected for sake of simplicity and it can be modeled using a 3D look-up table as a function of the pump outlet pressure and pump supply voltage. The 3D look-up table of the gear-type fuel pump is depicted in Fig. 2.9.

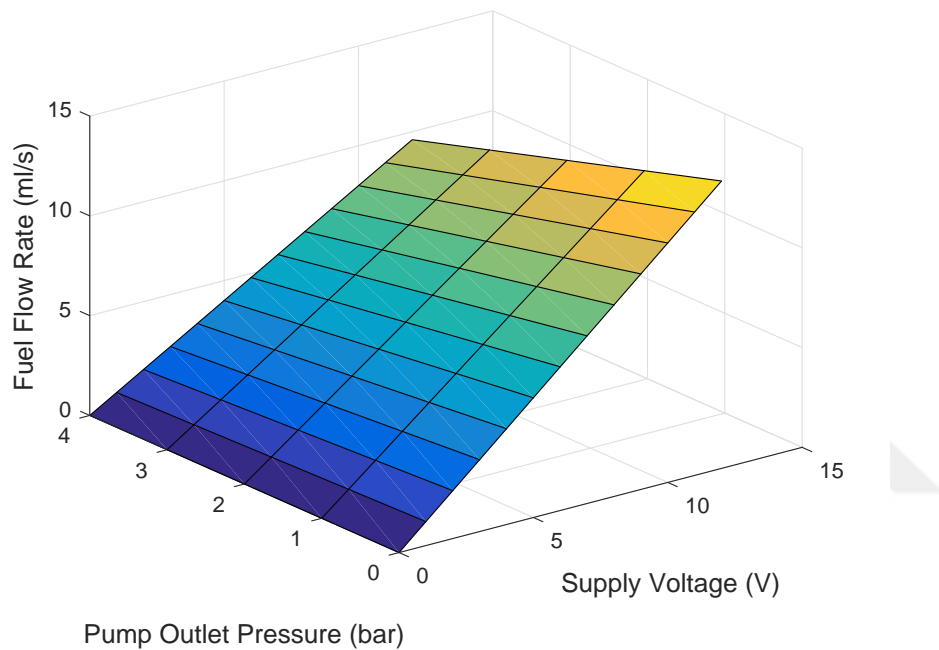


Figure 2.9: 3D Look-Up Table of the Gear-Type Fuel Pump

## 2.3 Aero-Thermal Turbojet Engine Model Validation

The aero-thermal turbojet model was developed in the MATLAB/Simulink environment and the simulation results were compared with the experimental data published in Ref. [14]. The simulation settings are ODE4 (Runge-Kutta) for the solver method and  $dt = 0.001$  s for the time step. The engine is considered to run on a test bench ( $U_0 = 0$  m/s) at sea level. The ambient conditions ( $P_0$ ,  $T_0$ ) are 288.15 K for the temperature and 101325 Pa for the pressure. The plenum volumes are  $0.002$  m<sup>3</sup> for  $V_{p,c}$  and  $0.001$  m<sup>3</sup> for  $V_{p,jp}$ . The inertia of the rotor assembly ( $J$ ) is  $0.0002$  kgm<sup>2</sup>. The properties of the jet fuel (JP8) are set to 2010 J/kgK for  $C_p$  and  $42.5 \times 10^6$  J/kg for  $LHV$ . For the burner, the pressure loss ( $\eta_{loss}$ ) and time constant ( $\tau_b$ ) are set to 0.98 and 0.01 s, respectively. The efficiencies are 0.80 for the burner ( $\eta_b$ ), 0.98 for the nozzle ( $\eta_n$ ), and 0.90 for the mechanical transmission ( $\eta_m$ ). The initial state vector is:

$$x = [294845 Pa, 162676 Pa, 1159 K, 89.68 \% N_{max}]^T \quad (2.32)$$

where the states are obtained from the trim condition for the fuel flow rate input of:

$$u = 8 \times 10^{-3} \text{ kg/s} \quad (2.33)$$

### 2.3.1 Steady-State Results

The steady-state comparison results for the compressor outlet pressures, EGTs ( $T_6$ ), thrusts, and fuel flow rates versus the shaft speed are depicted in Figs. 2.10, 2.11, 2.12, 2.13. As seen in the figures, the simulation results show similar trends with the experimental data. The main differences between the results, especially in the fuel flow rate result, are caused by the different control input implementation. For the experimental results, the AMT turbojet engine is controlled in the closed-loop control as shown in Fig. 2.1. Therefore, the shaft speed command is the control input of the turbojet engine and is denoted by the x-axis in the figures. However, the aero-thermal model results are of the open-loop control so that the fuel flow rate shown in Fig. 2.12 is the control input of the engine. Nevertheless, by adjusting the efficiencies, the differences between the simulation result and the experimental data can be compensated and a higher convergence may be obtained. However, an accurate engine performance model is beyond the scope of this study.

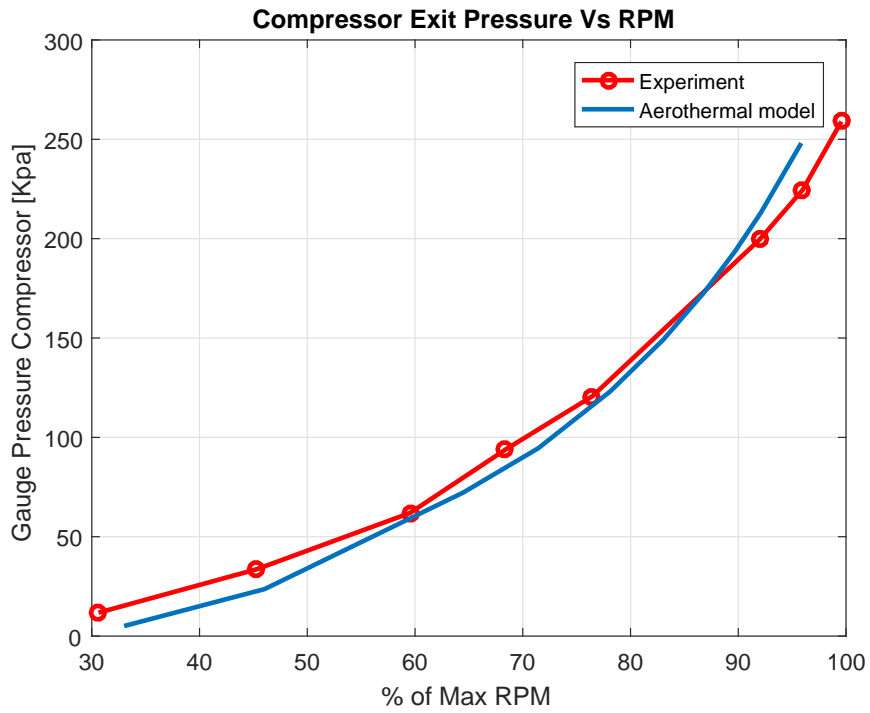


Figure 2.10: Compressor Outlet Pressure Comparison with Ref. [14]

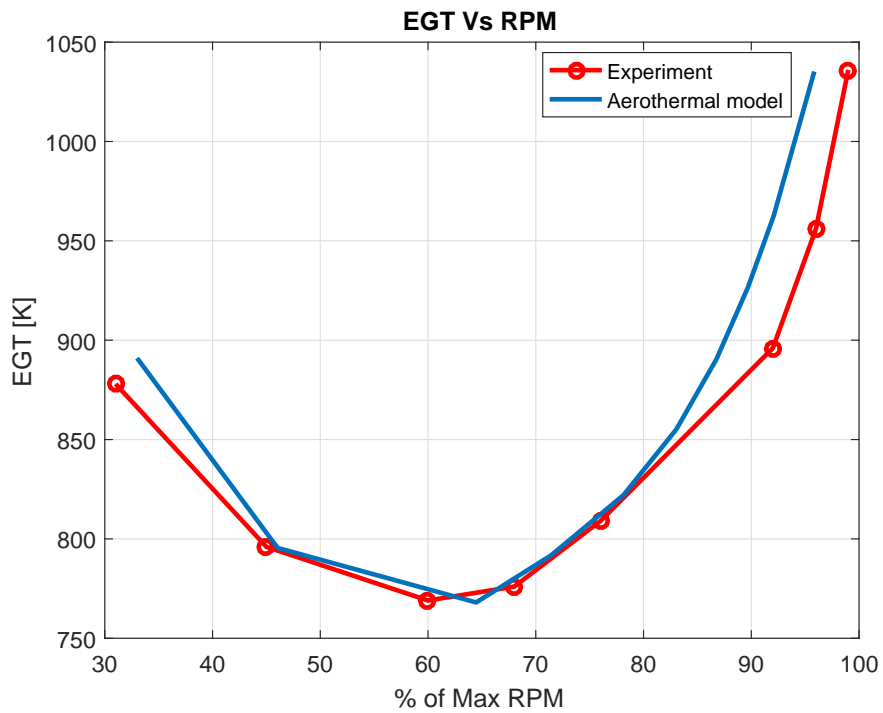


Figure 2.11: EGT Comparison with Ref. [14]

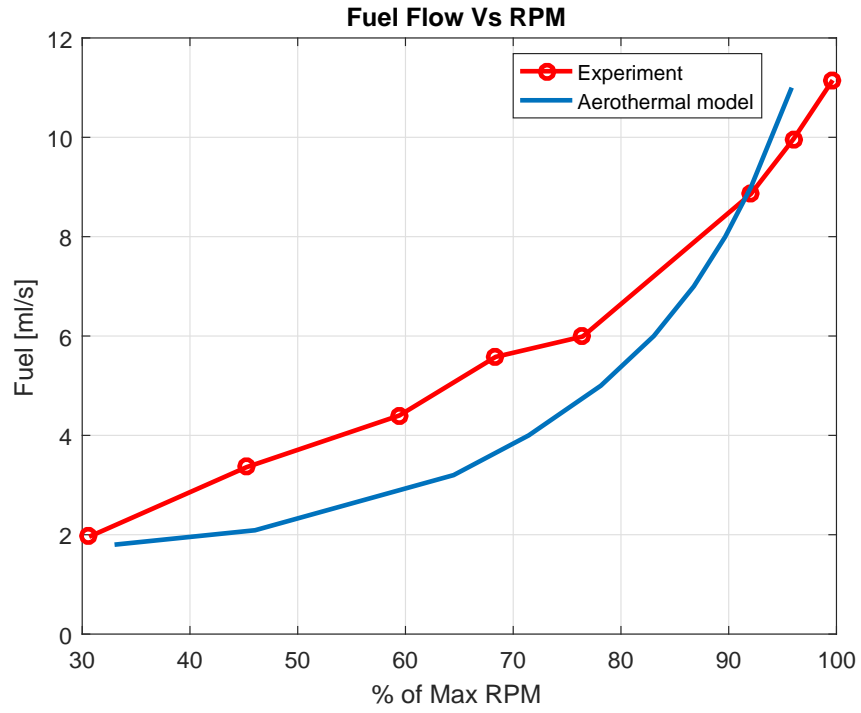


Figure 2.12: Fuel Flow Rate Comparison with Ref. [14]

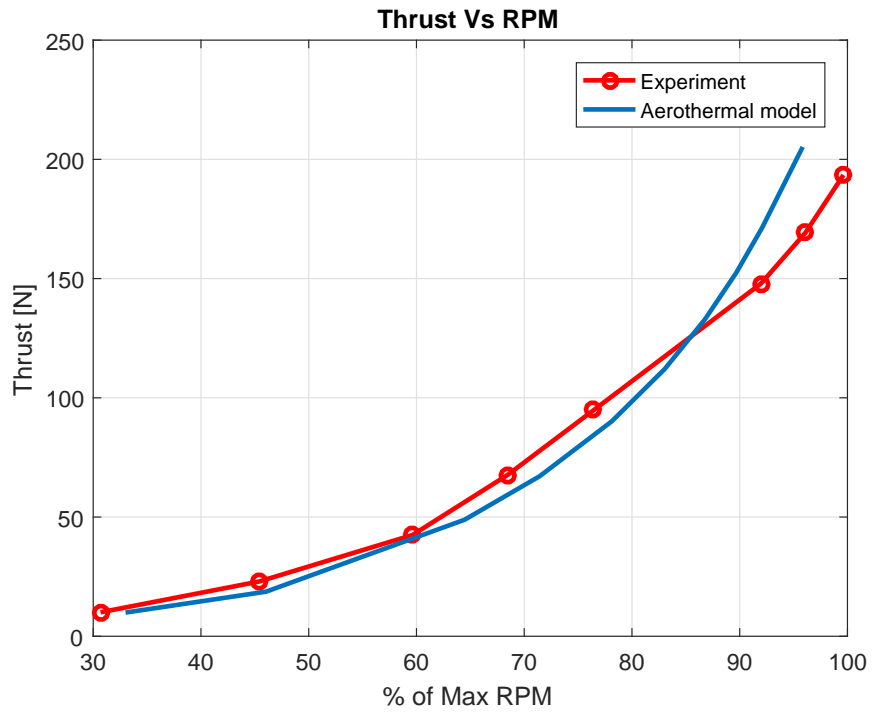


Figure 2.13: Thrust Comparison with Ref. [14]

### 2.3.2 Transient Results

The transient response of the aero-thermal model states ( $P_3$ ,  $P_5$ ,  $T_4$ ,  $N$ ) for an applied staircase input of the fuel flow rate ( $g_b$ ) is shown in Figs 2.14 2.15 2.16 2.17.

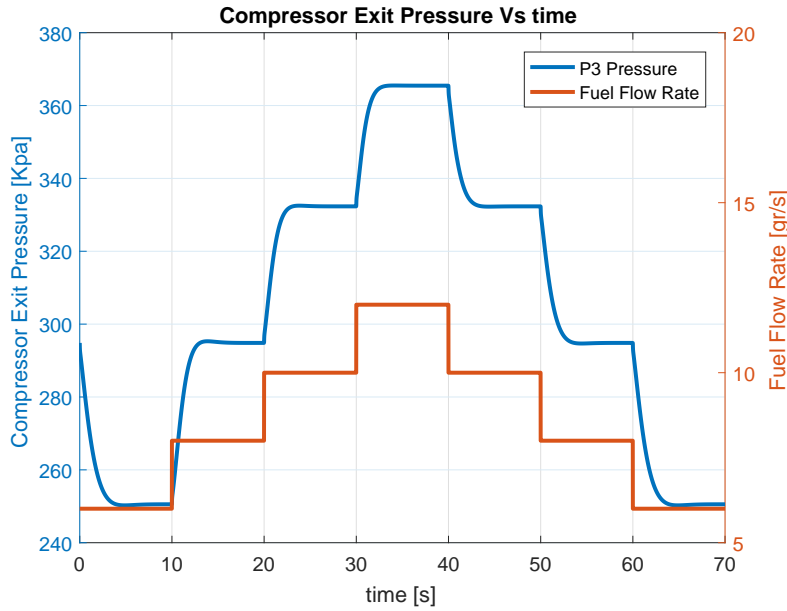


Figure 2.14: Compressor Outlet Pressure ( $P_3$ ) Response of the Aero-Thermal Model

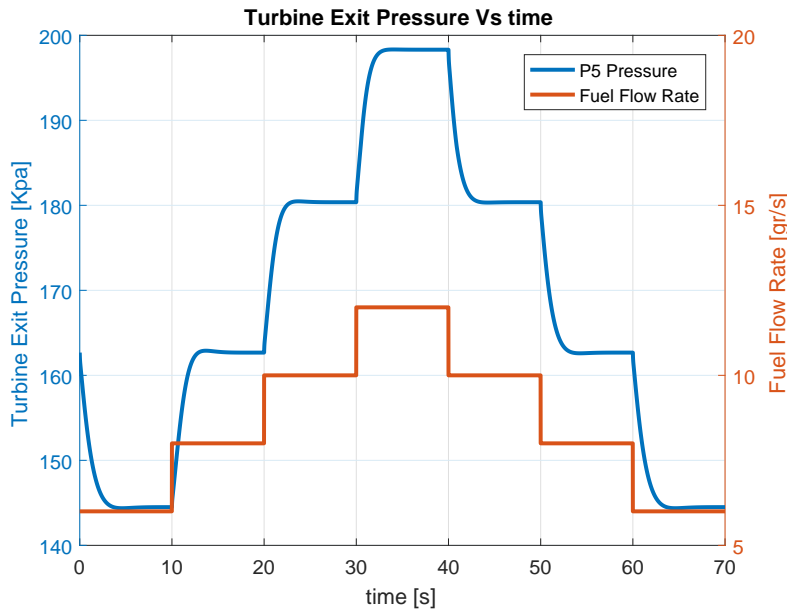


Figure 2.15: Turbine Outlet Pressure Response ( $P_5$ ) of the Aero-Thermal Model



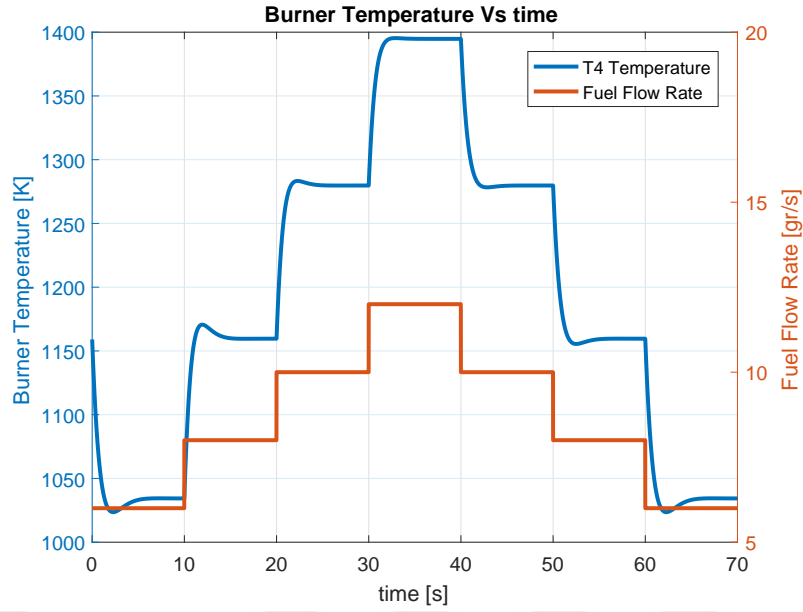


Figure 2.16: Burner Temperature Response ( $T_4$ ) of the Aero-Thermal Model

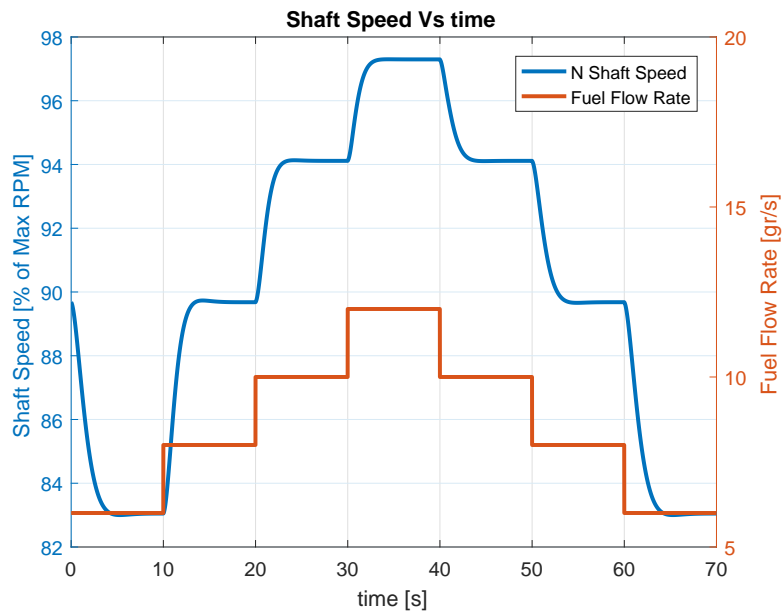


Figure 2.17: Shaft Speed Response ( $N$ ) of the Aero-Thermal Model

In refs. [1, 9, 29], and our previous works [7, 8, 28], a first or second order transfer function can be fitted on each step response of a gas turbine engine. As seen in the figures, the transient responses of the aero-thermal model are consistent with a first or second order transfer function output.



## CHAPTER 3

### OFFLINE SYSTEM IDENTIFICATION

System identification defines a methodology to construct mathematical models of dynamical systems based on the observed data. Data set, model structure, and identification method are the basic elements of this methodology. An appropriate structure which defines the interaction between the regressors and unknown system parameters is the most important step of this methodology [30].

The dynamical behavior of a system can be approximated by linear models around its equilibrium points. This approach is called the black-box method in the literature [30]. This method is also used to model the dynamical response of gas turbines. In ref. [9], Rowen uses a first-order transfer function to simulate the shaft dynamics of a heavy-duty gas turbine. In ref. [1, 10], further details can be found.

In this study, the target STE is just actuated with a simple gear-type fuel pump rather than an FMU. So, the overall system is inherently non-linear due to the internal dynamics of the turbojet engine and its interaction with the fuel pump. Hence, the classical approaches given in refs. [1, 9, 10, 30] cannot be directly used to get a fast engine model which can simulate all the shaft dynamics along the operational range.

In this chapter, a fast engine model structure and its offline parameter estimation algorithm are proposed for the shaft dynamics of a turbojet engine. To estimate the fast engine model parameters, the least squares method is used. Then, the obtained model is tested under different fuel command scenarios. Last, the same identification procedure is applied to the dataset of a real turbojet engine.

### 3.1 Fast Engine Model Structure

The target propulsion system consisting of a turbojet engine and a gear-type fuel pump is illustrated in Fig. 3.1. Here, the red dashed line defines the system boundaries to be represented by a fast engine model structure and to be identified later. The actuation voltage of the fuel pump is the input, and the rotational speed of the engine shaft is the output of the system, respectively.

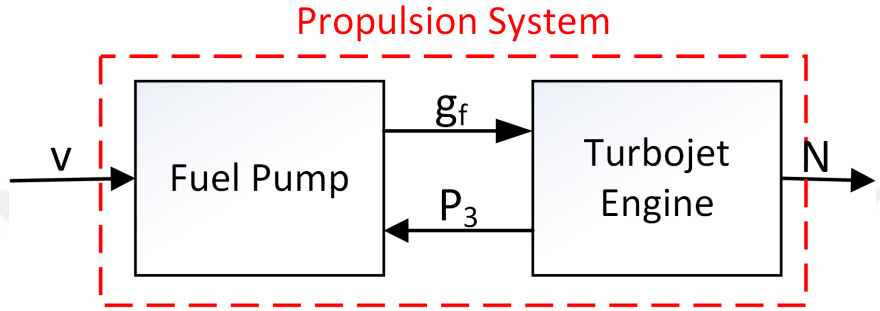


Figure 3.1: Turbojet Engine with a Gear-Type Fuel Pump

To see the shaft dynamics response of the aero-thermal model, a staircase fuel pump voltage input is applied to the propulsion system. Figure 3.2 shows the applied fuel pump voltage input and the resulting aero-thermal model response. Also shown is the output of a second-order transfer function defined as:

$$\frac{N(s)}{V(s)} = \frac{K\omega_n^2}{s^2 + 2\zeta\omega_n s + \omega_n^2} \quad (3.1)$$

where the parameters of the second-order transfer function are  $\omega_n = 1.4$ ,  $\zeta = 0.85$  and  $K = 2.2$ . The response of this transfer function is denoted by the dashed blue line. As seen in the figure, the proposed linear model fits on the aero-thermal model response between the shaft speeds of  $90\%N_{max}$  and  $94\%N_{max}$ . However, the output of this linear model becomes inaccurate at higher and lower shaft speeds. As it is known, the parameters  $\omega_n$  and  $\zeta$  only affect the transient behavior of the linear model. So here, the inaccurate gain  $K$  is the major source of the error. Therefore, the gain  $K$  can be modified as a polynomial function of the shaft speed:

$$K = \alpha_2 \Delta N(s)^2 + \alpha_1 \Delta N(s) + \alpha_0 \quad (3.2)$$

where the  $\alpha$ 's denote the coefficients of the second-order polynomial.

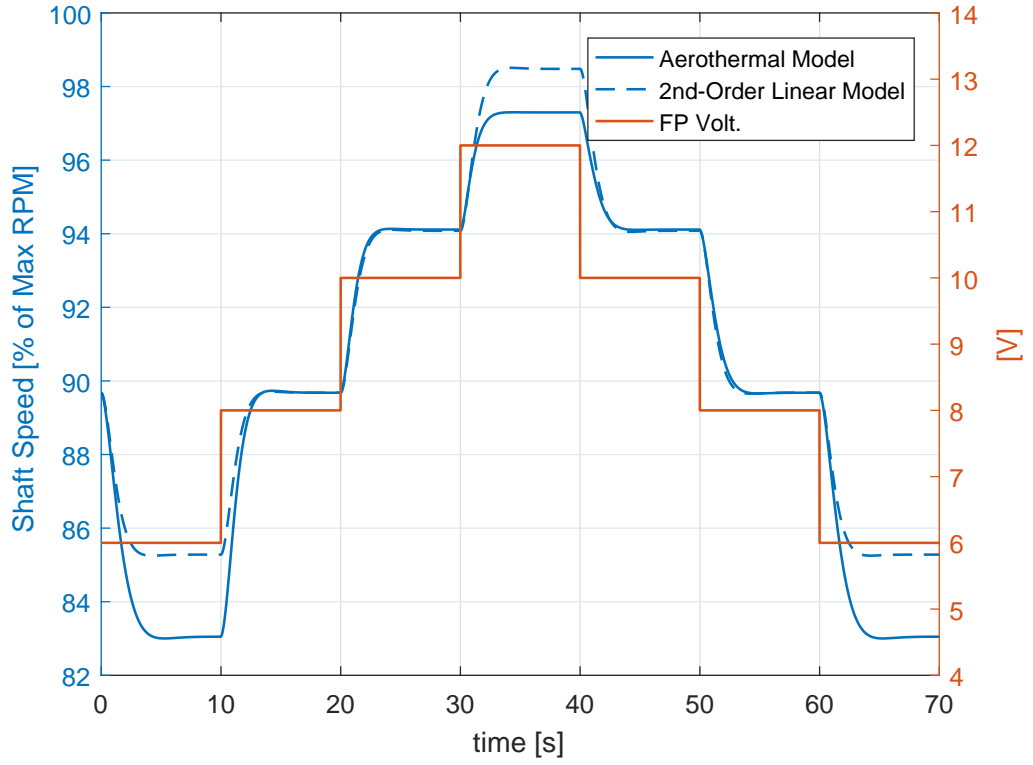


Figure 3.2: Aero-Thermal Model Response to Voltage Inputs

Thus, Eqn. 3.1 becomes:

$$\frac{\Delta N(s)}{\Delta V(s)} = \frac{(\alpha_2 \Delta N(s)^2 + \alpha_1 \Delta N(s) + \alpha_0) \omega_n^2}{s^2 + 2\zeta \omega_n s + \omega_n^2} \quad (3.3)$$

If Eqn. 3.3 is converted to the time-domain and rearranged, the following is obtained:

$$\Delta \ddot{N} = -2\zeta \omega_n \Delta \dot{N} - \omega_n^2 \Delta N + \alpha_2 \omega_n^2 \Delta N^2 \Delta V + \alpha_1 \omega_n^2 \Delta N \Delta V + \alpha_0 \omega_n^2 \Delta V \quad (3.4)$$

The state-space representation of Eqn. 3.4 is

$$\begin{bmatrix} \Delta \dot{N} \\ \Delta \ddot{N} \end{bmatrix} = \begin{bmatrix} 0 & 1 \\ -\omega_n^2 & -2\zeta \omega_n \end{bmatrix} \begin{bmatrix} \Delta N \\ \Delta \dot{N} \end{bmatrix} + \begin{bmatrix} 0 \\ \alpha_0 \omega_n^2 \end{bmatrix} \Delta V + \begin{bmatrix} 0 & 0 \\ \alpha_1 \omega_n^2 & \alpha_2 \omega_n^2 \end{bmatrix} \begin{bmatrix} \Delta N \Delta V \\ \Delta N^2 \Delta V \end{bmatrix} \quad (3.5)$$

where  $N$  and  $\dot{N}$  form the state vector of the fast engine model structure. The linear

part of this fast engine model structure is still a second-order transfer function:

$$LP = \begin{bmatrix} 0 & 1 \\ -\omega_n^2 & -2\zeta\omega_n \end{bmatrix} \begin{bmatrix} N \\ \dot{N} \end{bmatrix} + \begin{bmatrix} 0 \\ \alpha_0\omega_n^2 \end{bmatrix} V \quad (3.6)$$

and the nonlinear part of the model is:

$$NLP = \begin{bmatrix} 0 & 0 \\ \alpha_1\omega_n^2 & \alpha_2\omega_n^2 \end{bmatrix} \begin{bmatrix} NV \\ N^2V \end{bmatrix} \quad (3.7)$$

### 3.2 Derivation of the Offline Estimation Algorithm

The method of least squares is applied for the parameter estimation of the proposed fast engine model structure given in Eqn. 3.5. In this method, the main idea is to minimize the sum of the squares of residuals between the system output and the regression model. The main advantages of this technique are the mathematical simplicity of the algorithm which is based on simple matrix algebraic operations, and the parameter estimates are obtained by a single-step calculation cycle. In addition, the least squares method can be applied to non-linear models similar to linear models [31].

Equation 3.4 can be rewritten as a regression model in discrete time domain:

$$\begin{aligned} \Delta\ddot{N}(k) = & -2\zeta\omega_n\Delta\dot{N}(k) - \omega_n^2\Delta N(k) + \alpha_2\omega_n^2\Delta N^2(k)\Delta V(k) + \\ & \alpha_1\omega_n^2\Delta N(k)\Delta V(k) + \alpha_0\omega_n^2\Delta V(k) \end{aligned} \quad (3.8)$$

where  $\ddot{N}(k)$  is the measured system response (or dependent variable) at  $k$ th data point and can be symbolized by:

$$y(k) = \ddot{N}(k) \quad (3.9)$$

Additionally,  $N$ ,  $\dot{N}$  and,  $V$  are the independent variables of the equation. These variables are alternatively called "regressors", "predictor variables", or "explanatory variables" [31] and can be rewritten in a vector form represented by  $x$  as follows:

$$x(k) = [\Delta N(k) \quad \Delta\dot{N}(k) \quad \Delta V(k) \quad \Delta N^2(k)\Delta V(k) \quad \Delta N(k)\Delta V(k)] \quad (3.10)$$

Last,  $\omega_n$ ,  $\zeta$  and  $\alpha_i$  are the unknown parameters to be estimated. Also, these parameters are considered as constant and uncorrelated with the independent variables, and they can be symbolized by the vector  $\theta$ :

$$\theta = [-\omega_n^2 \quad -2\zeta\omega_n \quad \alpha_0\omega_n^2 \quad \alpha_1\omega_n^2 \quad \alpha_2\omega_n^2]^T \quad (3.11)$$

Finally, Equation 3.8 can be rewritten as:

$$y(k) = x(k)\theta + \epsilon(k) \quad (3.12)$$

where  $\epsilon$  is the error in the measurement. Although the parameters multiply both linear and nonlinear functions of the independent variables, the equation is still linear in the parameters. Thus, for discrete time point  $k$ , Eqn. 3.12 can be written as:

$$\begin{aligned} y(1) &= x(1)\theta + \epsilon(1); \\ y(2) &= x(2)\theta + \epsilon(2); \\ &\vdots \quad \quad \quad \vdots \\ y(k) &= x(k)\theta + \epsilon(k); \end{aligned} \quad (3.13)$$

The matrix form of this regression model becomes:

$$X = \begin{bmatrix} \Delta N(1) & \Delta \dot{N}(1) & \Delta V(1) & \Delta N^2(1)\Delta V(1) & \Delta N(1)\Delta V(1) \\ \Delta N(2) & \Delta \dot{N}(2) & \Delta V(1) & \Delta N^2(2)\Delta V(2) & \Delta N(2)\Delta V(2) \\ \vdots & \vdots & \vdots & \vdots & \vdots \\ \Delta N(k) & \Delta \dot{N}(k) & \Delta V(k) & \Delta N^2(k)\Delta V(k) & \Delta N(k)\Delta V(k) \end{bmatrix} \quad (3.14)$$

$$Y = [\ddot{N}(1) \ \ddot{N}(2) \ \dots \ \ddot{N}(k)]^T \quad (3.15)$$

$$\epsilon = [\epsilon(1) \ \epsilon(2) \ \dots \ \epsilon(k)]^T \quad (3.16)$$

It is assumed that the error is uncorrelated with the independent variables and has zero mean ( $E(\epsilon) = 0$ ) and variance ( $E(\epsilon\epsilon^T) = \sigma^2 I = 0$ ) [31]. So, Equation 3.13 can be rewritten in a matrix form:

$$Y = X\theta + \epsilon \quad (3.17)$$

and, the equation error becomes:

$$\epsilon = Y - X\theta; \quad (3.18)$$

The best estimator of  $\theta$  in a least-squares sense obtained by minimizing the sum of squared differences between the measurement and the model, and this defines the cost function [31, 32]:

$$J(\theta) = \frac{1}{2}(Y - X\theta)^T(Y - X\theta) \quad (3.19)$$

The gradient of the cost function with respect to  $\theta$  gives the estimated parameter values  $\hat{\theta}$  minimizing the cost function:

$$\frac{\partial J}{\partial \theta} = -Y^T X + \theta^T (X^T X) = 0 \quad (3.20)$$

Here,  $\theta$  can be replaced with  $\hat{\theta}$  which is the estimation of the true parameter values and then, the equation becomes:

$$(X^T X)\hat{\theta} = X^T Y \quad (3.21)$$

Finally, assuming  $X^T X$  to be invertible, we get:

$$\hat{\theta} = (X^T X)^{-1} X^T Y \quad (3.22)$$

which is the least squares estimate of  $\theta$ .

### 3.3 Offline Parameter Estimation of an Aero-Thermal Model

The system identification method derived above is first tested on the developed aero-thermal turbojet engine model with a gear-type fuel pump described in Sec. 2. The initial conditions defined in Sec. 2.10 are used for the simulation. Figure 3.3 shows the shaft speed response of the aero-thermal model to the staircase fuel flow rate input. Here, the engine first decelerates to the shaft speed of  $83\%N_{max}$  and then accelerates to  $90\%N_{max}$ ,  $94\%N_{max}$  and  $97\%N_{max}$ , respectively. Then, the engine decelerates back through to the same fuel pump command inputs. To obtain  $X$  of Eqn. 3.2, the trim values are subtracted from the actual values. By applying Eqn. 3.22, the parameter estimation vector  $\hat{\theta}$  is found as:

$$\hat{\theta} = [-1.8054 \quad -2.3360 \quad 4.8220 \quad -0.1835 \quad -0.0001] \quad (3.23)$$

and the fast engine model given in Eqn. 3.5 becomes:

$$\begin{bmatrix} \Delta \dot{N} \\ \Delta \ddot{N} \end{bmatrix} = \begin{bmatrix} 0 & 1 \\ -1.8054 & -2.3360 \end{bmatrix} \begin{bmatrix} \Delta N \\ \Delta \dot{N} \end{bmatrix} + \begin{bmatrix} 0 \\ 4.8220 \end{bmatrix} \Delta V + \begin{bmatrix} 0 & 0 \\ -0.1835 & -0.0001 \end{bmatrix} \begin{bmatrix} \Delta N \Delta V \\ \Delta N^2 \Delta V \end{bmatrix} \quad (3.24)$$



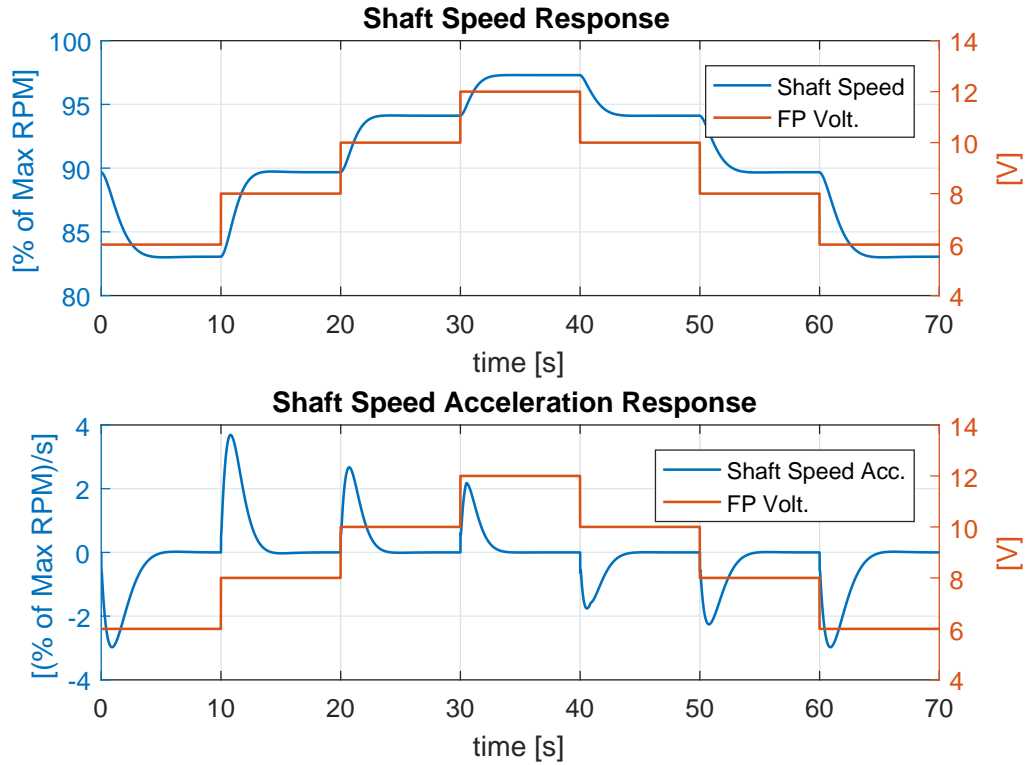


Figure 3.3: Aero-Thermal Model Response to the Stairs Level of Fuel Flow Rate Input

Therefore, the estimated system parameters are found as follows:

$$\omega_n = 1.3437$$

$$\zeta = 0.8692$$

$$\alpha_0 = 2.6709$$

$$\alpha_1 = -0.1016$$

$$\alpha_2 = -0.00006$$

The roots of the linear part of the fast engine model are found as  $\lambda_{1,2} = -1.1680 \pm 0.6642i$ , and it is stable as expected. Figure 3.4 compares the obtained fast engine model outputs ( $\Delta N$ ,  $\Delta \dot{N}$ ) with the data set gathered from the aero-thermal model. The estimated values for the proposed fast engine model structure provide the expected convergence with the aero-thermal model.

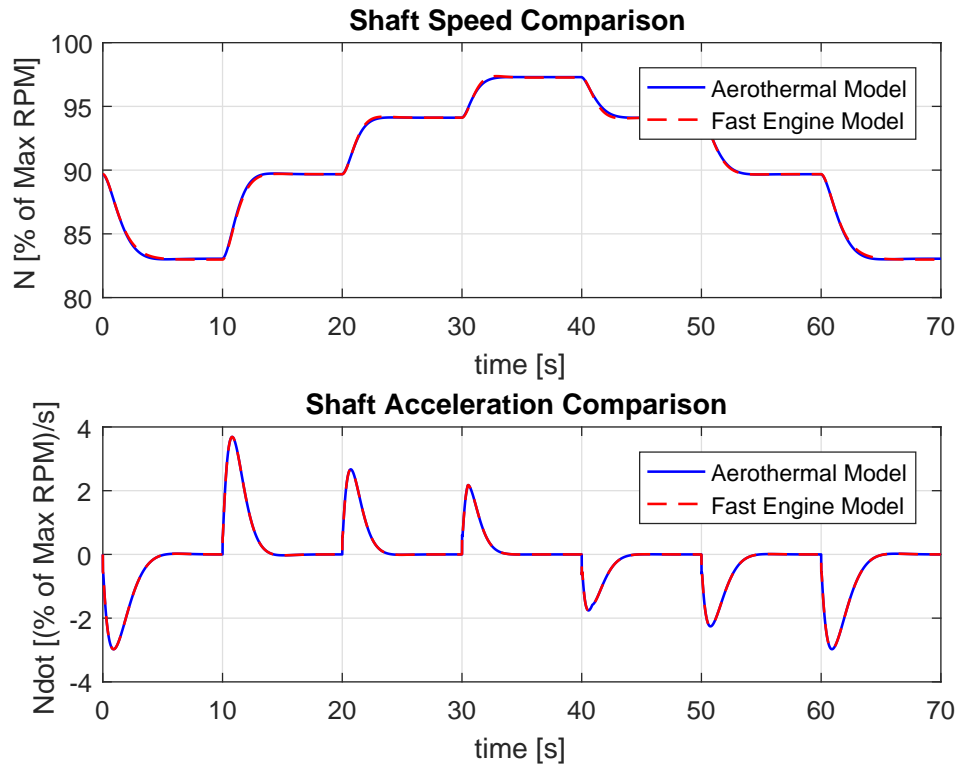


Figure 3.4: State Comparison of the Models

To test the fast engine model under different fuel command scenarios, first, a periodical square input command is applied. The comparison of the fast engine model response with the aero-thermal model response is shown in Fig. 3.5. As seen in the figure, the fast engine model show a good consistency with the aero-thermal model response and the differences seem negligible.

As the second scenario, a sinusoidal fuel pump command with  $\Delta = 1V$  amplitude and 0.05 Hz frequency is applied on both the aero-thermal model and fast engine model. As it is shown in Fig. 3.6, the shaft speed response of the aero-thermal model oscillates between  $87\%N_{max}$  and  $92\%N_{max}$  and the fast engine model closely follows it.

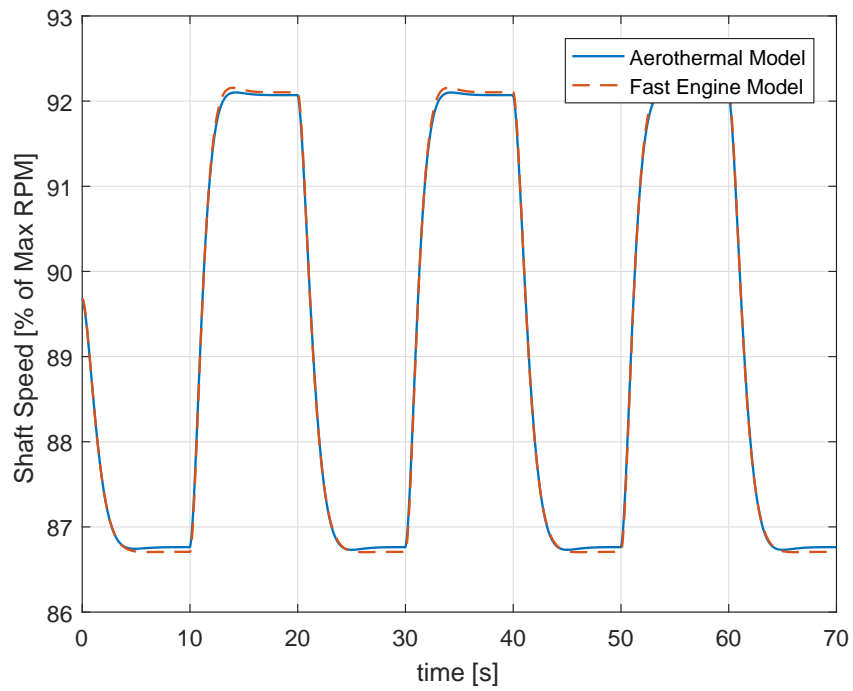


Figure 3.5: Comparison of the Test Results for an Applied Square Wave Command

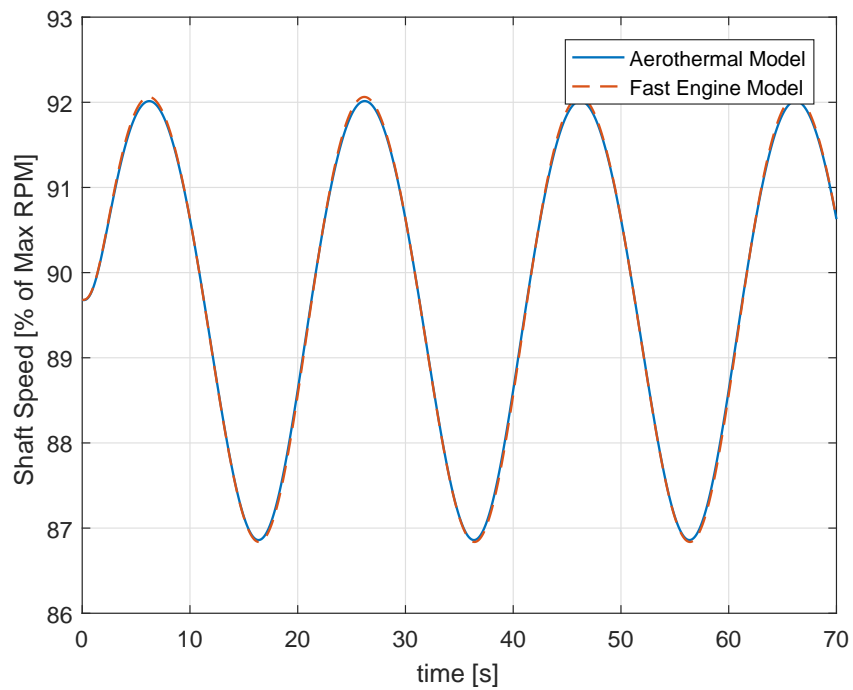


Figure 3.6: Comparison of the Test Results for an Applied Sinusoidal Command

### 3.4 Offline Parameter Estimation of a Test Engine

The method is then tested on a real turbojet engine in ground testing. The test setup consisting of an experimental STE actuated with a gear-type fuel pump is shown in Fig 3.7. The engine produces 400 N of thrust at 100,000 RPM. For the safety, the engine's shaft speed is limited to 85,000 RPM using the ECU software during the experiments. Here, the ECU is in an aluminum box containing an electronic card, a gear-type fuel pump, and two fuel-line valves. The electronic card accommodates a 16-bit microprocessor, data acquisition circuits for the EGT and shaft speed measurements, drivers for the fuel pump and fuel valves, and flash memory for the logging. Further details about the test setup and ECU are given in Refs. [7, 8].

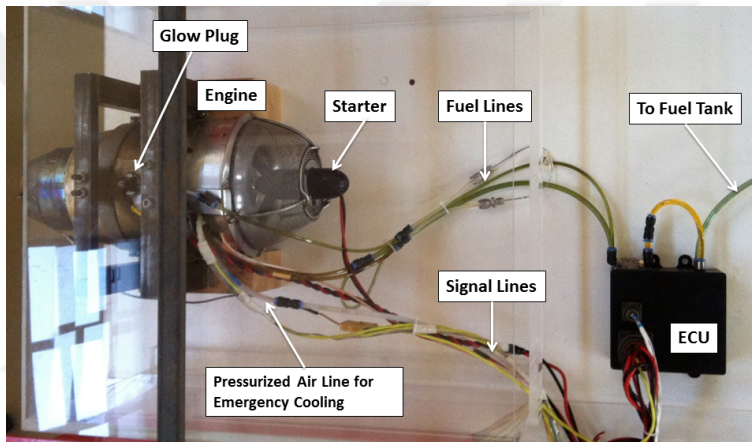


Figure 3.7: Test-Bed with a Turbojet Engine and ECU [8]

The test data gathered from the turbojet engine for the applied staircase fuel pump input command is depicted in Fig. 3.8. However, the data is not sufficient to evaluate the derived least squares algorithm because of the missing shaft speed acceleration, but here, normal derivation techniques become inappropriate because the sample rate of these noisy data is only 10Hz. For the solution, the local smoothing method explained in [32] is used. This method again uses a least squares method to fit a second-order polynomial on the gathered data points in the time-domain. After applying this method, the obtained smoothed shaft speed and derived shaft speed acceleration results are depicted in Fig. 3.9. As it is shown in Fig. 3.9, the shaft acceleration data has less noise and it is now suitable to be used in the estimation algorithm.

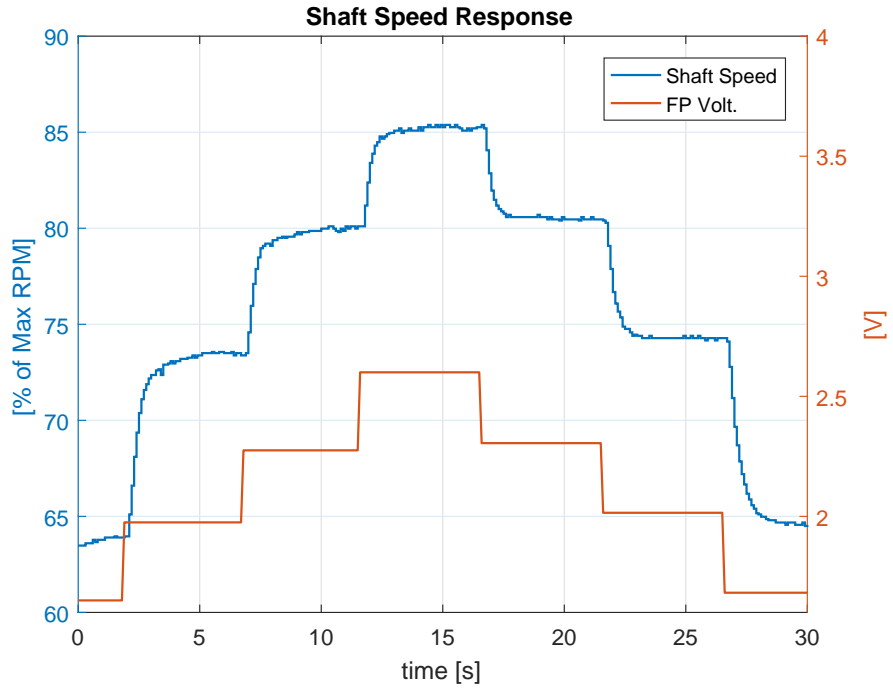


Figure 3.8: Turbojet Engine Response to the Stairs Level Fuel Flow Rate Input

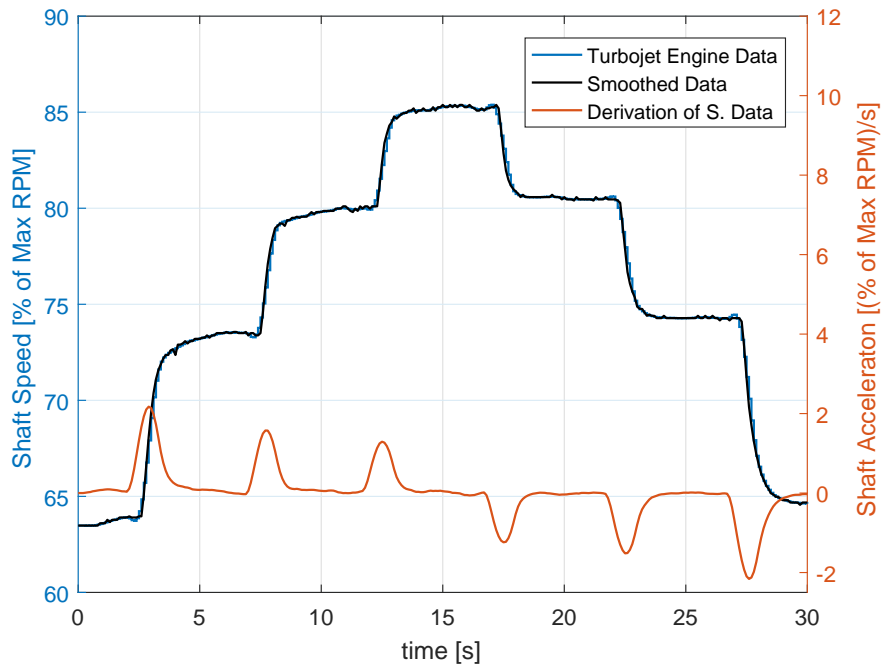


Figure 3.9: Comparison of the Smoothed Data with the Raw Data and the Derived Shaft Acceleration

After applying the derived least-squares algorithm to the smoothed test data, the fast engine model is estimated as:

$$\begin{bmatrix} \Delta \dot{N} \\ \Delta \ddot{N} \end{bmatrix} = \begin{bmatrix} 0 & 1 \\ -15.9153 & -7.5902 \end{bmatrix} \begin{bmatrix} \Delta N \\ \Delta \dot{N} \end{bmatrix} + \begin{bmatrix} 0 \\ 573.2520 \end{bmatrix} \Delta V + \begin{bmatrix} 0 & 0 \\ -8.7614 & -0.0334 \end{bmatrix} \begin{bmatrix} \Delta N \Delta V \\ \Delta N^2 \Delta V \end{bmatrix} \quad (3.25)$$

and the parameters of the model are found as:

$$\omega_n = 3.9894$$

$$\zeta = 0.9513$$

$$\alpha_0 = 36.0189$$

$$\alpha_1 = -0.5505$$

$$\alpha_2 = -0.0021$$

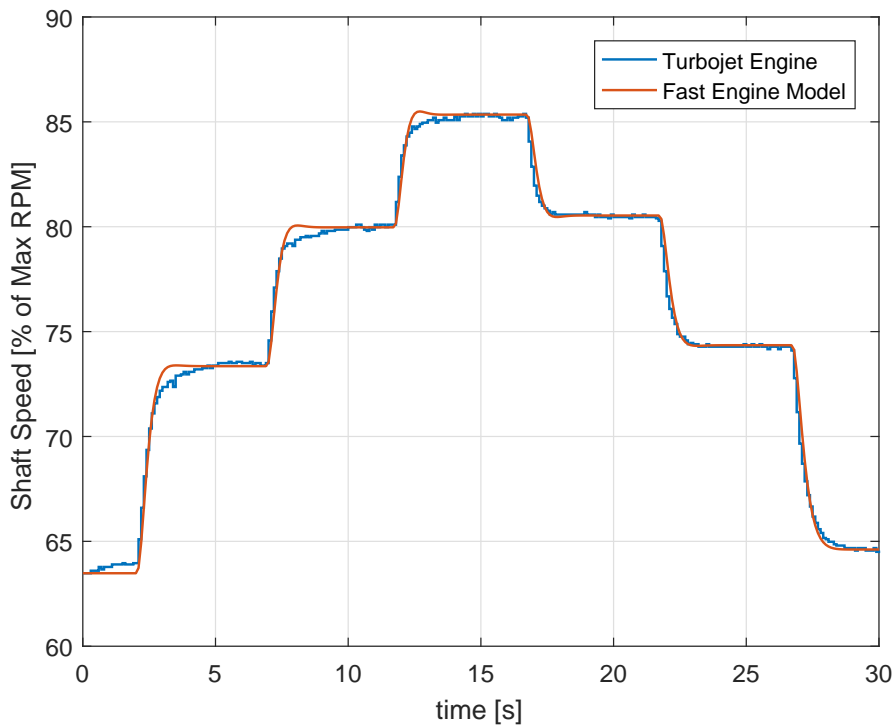


Figure 3.10: Comparison of the Fast Engine Model Output with the Turbojet Engine Data

The linear part of the system is stable as expected with the roots of  $\lambda_{1,2} = -3.7951 \pm 1.2298j$ . Figure 3.10 compares the obtained fast engine model response with the real engine test data. Even the acceleration and deceleration responses of the engine are not symmetrical, the fast engine model follows the test engine response with acceptable accuracy.

As it is shown in the test result, the proposed fast engine model structure and the derived parameter estimation algorithm based on the least squares method are applicable to similar turbojet engines, especially those actuated with a gear-type fuel pump.

Finally, this offline identification method can also be applied to any nonlinear system that is especially actuated by a nonlinear actuator. The generalized version of this method is given in Appendix A.





## CHAPTER 4

### ONLINE SYSTEM IDENTIFICATION

In this chapter, an online parameter estimation algorithm based on Lyapunov stability theorem is derived for the target STEs. The algorithm uses the fast engine model structure proposed in Sec: 3.1. By using the regressors defined in this model structure, the parameter update laws are derived and then, their boundedness and convergence are proved. Last, the derived algorithm is tested on both the fast and aero-thermal turbojet engine model, respectively.

#### 4.1 Derivation of the Online Estimation Algorithm

The general structure of the online system identification algorithm is depicted in Fig. 4.1. Here, the block "Plant" represents a nonlinear time-invariant system with an input ( $u(t)$ ) and output ( $y_p(t)$ ) signals. Its state dynamics ( $\dot{x}_p(t)$ ) and output ( $y_p(t)$ ) are defined with  $f_p(x_p, u, \Theta_p^*)$  and  $h_p(x_p)$ . Here, the final plant parameters are denoted by  $\Theta_p^*$ . The identification model is expressed with  $\dot{\hat{x}}_I = \hat{f}(\hat{x}_I, y_p, u, \hat{\Theta}_p)$  and  $\hat{y}_I = \hat{h}(\hat{x}_I)$  in the identification block. This block calculates the identified plant output ( $y_I$ ) by receiving the input and output signals from the plant and the estimated plant parameters ( $\hat{\Theta}_p$ ) from the adaptation block. The adaptation block uses Lyapunov stability theory based parameter update laws which are the functions of the plant input/output and the error ( $e_I$ ) between the plant and the identification model [33].

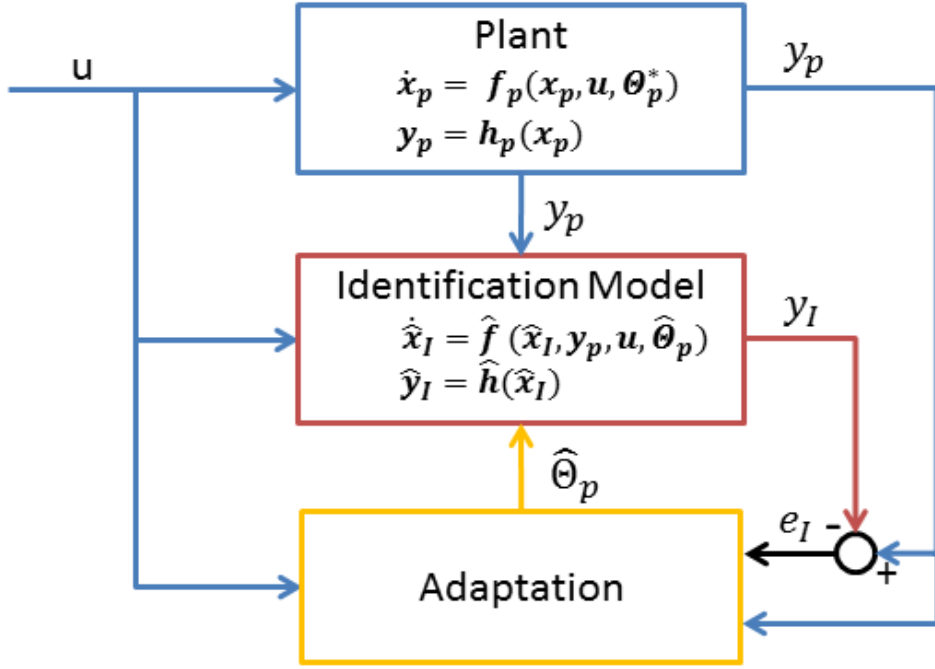


Figure 4.1: Online Parameter Estimation Structure [33]

In this study, the plant block is the shaft dynamics of an STE equipped with a gear-type fuel pump. If the fast engine model structure given in Eqn: 3.5 is recalled:

$$\begin{bmatrix} \Delta \dot{N} \\ \Delta \ddot{N} \end{bmatrix} = \begin{bmatrix} 0 & 1 \\ -\omega_n^2 & -2\zeta\omega_n \end{bmatrix} \begin{bmatrix} \Delta N \\ \Delta \dot{N} \end{bmatrix} + \begin{bmatrix} 0 \\ \alpha_0\omega_n^2 \end{bmatrix} \Delta V + \begin{bmatrix} 0 & 0 \\ \alpha_1\omega_n^2 & \alpha_2\omega_n^2 \end{bmatrix} \begin{bmatrix} \Delta N \Delta V \\ \Delta N^2 \Delta V \end{bmatrix} \quad (4.1)$$

The linear part of this nonlinear model can be denoted as:

$$A_p x_p + B_p u = \begin{bmatrix} 0 & 1 \\ -\omega_n^2 & -2\zeta\omega_n \end{bmatrix} \begin{bmatrix} \Delta N \\ \Delta \dot{N} \end{bmatrix} + \begin{bmatrix} 0 \\ \alpha_0\omega_n^2 \end{bmatrix} \Delta V \quad (4.2)$$

where the shaft speed ( $\Delta N$ ) and shaft acceleration ( $\Delta \dot{N}$ ) are the states of the fast engine model and can be represented with a system state vector  $x_p \in \mathfrak{R}^{2 \times 1}$ .  $\Delta V$  is the input of the system and can be represented with a control input  $u \in \mathfrak{R}$ .  $A_p \in \mathfrak{R}^{2 \times 2}$  is the state matrix which is constant and unknown. In addition, the input matrix  $\begin{bmatrix} 0 & \alpha_0\omega_n^2 \end{bmatrix}^T$  can be represented with a constant and known input vector  $B_p \in \mathfrak{R}^{2 \times 1}$

and with a constant, positive and unknown control effectiveness gain  $\Lambda \in \mathfrak{R}$ :

$$B_p \Lambda = \begin{bmatrix} 0 \\ 1 \end{bmatrix} \alpha_0 \omega_n^2 = \begin{bmatrix} 0 \\ \alpha_0 \omega_n^2 \end{bmatrix} \quad (4.3)$$

where  $\Lambda$  gain is the fuel pump performance factor which converts the fuel pump supply voltage into the fuel flow rate. Hereby, the representation of the linear part of the system becomes:

$$\dot{x}_p = A_p x_p + B_p \Lambda u \quad (4.4)$$

The nonlinear part of the fast engine model can be expressed by an unknown constant parameter matrix  $\Theta_f^* \in \mathfrak{R}^{2 \times 2}$ , and a known 2D regressor vector  $f(x_p, u) \in \mathfrak{R}^2$ , whose components are continuously differentiable functions of  $x_p$  and  $u$ :

$$\Theta_f^* f(x_p, u) = \begin{bmatrix} 0 & 0 \\ \alpha_1 \omega_n^2 & \alpha_2 \omega_n^2 \end{bmatrix} \begin{bmatrix} \Delta N \Delta V \\ \Delta N^2 \Delta V \end{bmatrix} \quad (4.5)$$

Finally, by using Eq. 4.4 and Eq. 4.5, the general form of the fast engine model becomes:

$$\dot{x}_p = A_p x_p + B_p \Lambda u + \Theta_f^* f(x_p, u) \quad (4.6)$$

In Fig. 4.2, the details of the system identification structure are given. Here, the proposed identification model is:

$$\dot{\hat{x}}_p = A_m \hat{x}_p + [\hat{A}_p - A_m] x_p + B_p \hat{\Lambda} u + \hat{\Theta}_f f(x_p, u) \quad (4.7)$$

where  $A_m$  matrix defines the identification model dynamics. Without  $A_m$  matrix, the error dynamics required to derive the parameter update laws depends on  $A_p$ , which is unknown and may be unstable. Here,  $A_m \in \mathfrak{R}^{2 \times 2}$  is a Hurwitz matrix ( $Re[\lambda_i] < 0$ ). Therefore, the error dynamics of the identification process will be:

$$\dot{e}_I = \dot{\hat{x}}_p - \dot{x}_p \quad (4.8)$$

Using the identification model dynamics defined in Eq. 4.7 and the plant dynamics given in Eq. 4.6, Eq. 4.8 can be rewritten as:

$$\dot{e}_I = A_m \hat{x}_p + [\hat{A}_p - A_m] x_p + B_p \hat{\Lambda}_p u + \hat{\Theta}_f f(x_p, u) - A_p x_p - B_p \Lambda u - \Theta_f^* f(x_p, u) \quad (4.9)$$

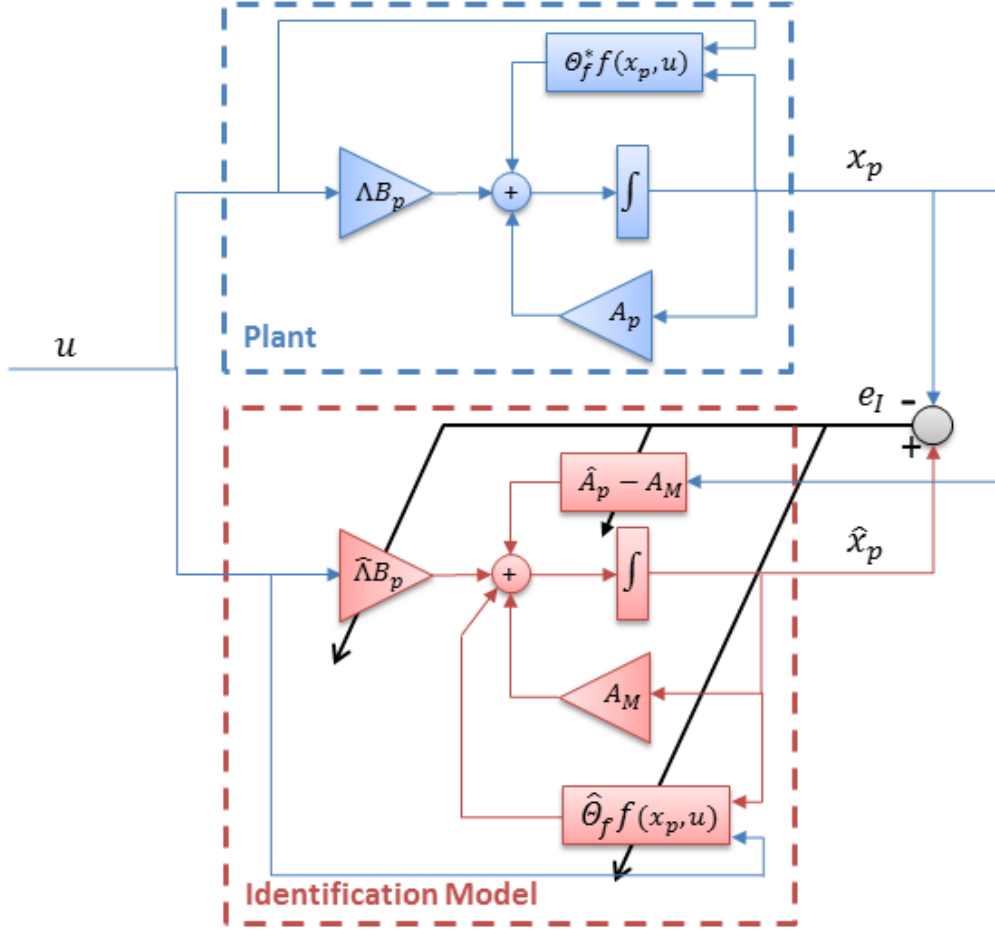


Figure 4.2: Detailed View of the Parameter Estimation Structure

and then:

$$\dot{e}_I = A_m[\hat{x}_p - x_p] + [\hat{A}_p - A_p]x_p + B_p[\hat{\Lambda} - \Lambda]u + [\hat{\Theta}_f - \Theta_f^*]f(x_p, u) \quad (4.10)$$

Finally, we get the error dynamics:

$$\dot{e}_I = A_m e_I + \tilde{A}_p x_p + B_p \tilde{\Lambda} u + \tilde{\Theta}_f f(x_p, u) \quad (4.11)$$

where:

$$\begin{aligned} \tilde{A}_p &= \hat{A}_p - A_p \\ \tilde{\Lambda} &= \hat{\Lambda} - \Lambda \\ \tilde{\Theta}_f &= \hat{\Theta}_f - \Theta_f^* \end{aligned} \quad (4.12)$$

To prove the stability and parameter convergence of the error dynamics, Lyapunov stability theory needs to be applied. For this, the Lyapunov function candidate can be

chosen as follows:

$$V = \frac{1}{2}e_I^T P e_I + \frac{1}{2}Tr[\tilde{A}_p \Gamma_A^{-1} \tilde{A}_p^T] + \frac{1}{2}Tr[\tilde{\Lambda} \Gamma_\Lambda^{-1} \tilde{\Lambda}^T] + \frac{1}{2}Tr[\tilde{\Theta}_f \Gamma_\Theta^{-1} \tilde{\Theta}_f^T] \quad (4.13)$$

where  $P \in \mathfrak{R}^{2x2}$  is a symmetric positive definite matrix,  $\Gamma_A \in \mathfrak{R}^{2x2}$  and  $\Gamma_f \in \mathfrak{R}^{2x2}$  are diagonal positive definite matrices, and  $\Gamma_\Lambda \in \mathfrak{R}$  is a scalar.

For the stability proof, the time derivative of the Lyapunov function should satisfy the condition of  $\dot{V} \leq 0$  [34, 35], so the trace parts of Eqn. (4.13) can be rearranged as:

$$\begin{aligned} \frac{1}{2} \frac{dTr[\tilde{A}_p \Gamma_A^{-1} \tilde{A}_p^T]}{dt} &= \frac{1}{2} Tr[\dot{\tilde{A}}_p \Gamma_A^{-1} \tilde{A}_p^T] + \frac{1}{2} Tr[\tilde{A}_p \Gamma_A^{-1} \dot{\tilde{A}}_p^T] = Tr[\tilde{A}_p \Gamma_A^{-1} \dot{\tilde{A}}_p^T] \\ \frac{1}{2} \frac{dTr[\tilde{\Lambda} \Gamma_\Lambda^{-1} \tilde{\Lambda}^T]}{dt} &= \frac{1}{2} Tr[\dot{\tilde{\Lambda}} \Gamma_\Lambda^{-1} \tilde{\Lambda}^T] + \frac{1}{2} Tr[\tilde{\Lambda} \Gamma_\Lambda^{-1} \dot{\tilde{\Lambda}}^T] = Tr[\tilde{\Lambda} \Gamma_\Lambda^{-1} \dot{\tilde{\Lambda}}^T] \\ \frac{1}{2} \frac{dTr[\tilde{\Theta}_f \Gamma_\Theta^{-1} \tilde{\Theta}_f^T]}{dt} &= \frac{1}{2} Tr[\dot{\tilde{\Theta}}_f \Gamma_\Theta^{-1} \tilde{\Theta}_f^T] + \frac{1}{2} Tr[\tilde{\Theta}_f \Gamma_\Theta^{-1} \dot{\tilde{\Theta}}_f^T] = Tr[\tilde{\Theta}_f \Gamma_\Theta^{-1} \dot{\tilde{\Theta}}_f^T] \end{aligned} \quad (4.14)$$

**Remark1:** The trace of a matrix is:

$$Tr[A] = \sum_{j=1}^n a_{jj} = a_{11} + a_{22} + \dots + a_{nn} \quad (4.15)$$

**Remark2:** The time derivative of a trace matrix is:

$$\frac{dTr[A]}{dt} = Tr \left[ \frac{dA}{dt} \right] \quad (4.16)$$

And, the time derivative of the Lyapunov function given in (4.13) is found as:

$$\dot{V} = e_I^T P \dot{e}_I + Tr[\tilde{A}_p \Gamma_A^{-1} \dot{\tilde{A}}_p^T] + Tr[\tilde{\Lambda} \Gamma_\Lambda^{-1} \dot{\tilde{\Lambda}}^T] + Tr[\tilde{\Theta}_f \Gamma_\Theta^{-1} \dot{\tilde{\Theta}}_f^T] \quad (4.17)$$

Again, by adding the error dynamic given in Eq. 4.11, this equation becomes:

$$\begin{aligned} \dot{V} = e_I^T P [A_m e_I + \tilde{A}_p x_p + B_p \tilde{\Lambda} u + \tilde{\Theta}_f f(x_p, u)] + \\ Tr[\tilde{A}_p \Gamma_A^{-1} \dot{\tilde{A}}_p^T] + \\ Tr[\tilde{\Lambda} \Gamma_\Lambda^{-1} \dot{\tilde{\Lambda}}^T] + \\ Tr[\tilde{\Theta}_f \Gamma_\Theta^{-1} \dot{\tilde{\Theta}}_f^T] \end{aligned} \quad (4.18)$$

where  $e_I^T P A_m e_I$  is a scalar and it can be rearranged as:

$$e_I^T P A_m e_I = \frac{1}{2} (e_I^T P A_m e_I)^T + \frac{1}{2} e_I^T P A_m e_I = \frac{1}{2} e_I^T (A_m^T P + P A_m) e_I \quad (4.19)$$

Then, the Lyapunov function derivative becomes:

$$\begin{aligned}\dot{V} = & \frac{1}{2}e_I^T(A_m^T P + P A_m)e_I + e_I^T P \tilde{A}_p x_p + Tr[\tilde{A}_p \Gamma_A^{-1} \dot{\tilde{A}}_p^T] + \\ & e_I^T P B_p \tilde{\Lambda} u + Tr[\tilde{\Lambda} \Gamma_\Lambda^{-1} \dot{\tilde{\Lambda}}^T] + \\ & e_I^T P \tilde{\Theta}_f f(x_p, u) + Tr[\tilde{\Theta}_f \Gamma_\Theta^{-1} \dot{\tilde{\Theta}}_f^T]\end{aligned}\quad (4.20)$$

By definition, the reference model is stable in the sense of Lyapunov and it can be defined as:

$$A_m^T P + P A_m = -Q_0 \quad (4.21)$$

Finally, the Lyapunov function derivative is obtained as below:

$$\begin{aligned}\dot{V} = & -\frac{1}{2}e_I^T Q_0 e_I + Tr[\tilde{A}_p(x_p e_I^T P + \Gamma_A^{-1} \dot{\tilde{A}}_p^T)] + \\ & Tr[\tilde{\Lambda}(u e_I^T P B_p + \Gamma_\Lambda^{-1} \dot{\tilde{\Lambda}}^T)] + \\ & Tr[\tilde{\Theta}_f(f(x_p, u) e_I^T P + \Gamma_\Theta^{-1} \dot{\tilde{\Theta}}_f^T)]\end{aligned}\quad (4.22)$$

**Remark3:** The trace identity given for two vectors a and b is:

$$a^T b = Tr[b \cdot a^T] \quad (4.23)$$

To satisfy  $\dot{V} \leq 0$  condition, the elements of  $\dot{V}$  should satisfy the following conditions:

$$\tilde{A}_p(x_p e_I^T P + \Gamma_A^{-1} \dot{\tilde{A}}_p^T) = 0 \quad (4.24)$$

$$\dot{\tilde{A}}_p^T = -\Gamma_A x_p e_I^T P \quad (4.25)$$

and similar to this equation, the other elements of  $\dot{V}$  becomes:

$$\tilde{\Lambda}(u e_I^T P B_p + \Gamma_\Lambda^{-1} \dot{\tilde{\Lambda}}^T) = 0 \quad (4.26)$$

$$\dot{\tilde{\Lambda}}^T = -\Gamma_\Lambda u e_I^T P B_p \quad (4.27)$$

and:

$$\tilde{\Theta}_f(f(x_p, u) e_I^T P + \Gamma_\Theta^{-1} \dot{\tilde{\Theta}}_f^T) = 0 \quad (4.28)$$

$$\dot{\tilde{\Theta}}_f^T = -\Gamma_\Theta f(x_p, u) e_I^T P \quad (4.29)$$

Here the  $Q_0$  matrix is a symmetric positive definite matrix defined as ( $A_m^T P + P A_m = -Q_0$   $Q_0 = Q_0^T > 0$ ). To satisfy ( $\dot{V} \leq 0$ ) condition, the elements of the Lyapunov

function derivative should satisfy the following conditions:

$$\begin{aligned}
\dot{\hat{A}}_p &= \dot{\hat{A}} - \dot{A} \quad \text{and} \quad \dot{A}_p = 0 \\
\dot{\hat{\Lambda}} &= \dot{\hat{\Lambda}} - \dot{\Lambda} \quad \text{and} \quad \dot{\Lambda} = 0 \\
\dot{\hat{\Theta}} &= \dot{\hat{\Theta}} - \dot{\Theta} \quad \text{and} \quad \dot{\Theta} = 0
\end{aligned} \tag{4.30}$$

and finally, the related parameter update laws are obtained as:

$$\begin{aligned}
\dot{\hat{A}}_p^T &= -\Gamma_A x_p e_I^T P \\
\dot{\hat{\Lambda}}^T &= -\Gamma_\Lambda u e_I^T P B_p \\
\dot{\hat{\Theta}}_f^T &= -\Gamma_f f(x_p, u) e_I^T P
\end{aligned} \tag{4.31}$$

Here the design parameters  $\Gamma_A$ ,  $\Gamma_\Lambda$ , and  $\Gamma_f$  are the learning rate gains, and they are used to determine the adaptation speed. Finally, the remaining element in Lyapunov function derivative inherently satisfies the given condition below:

$$\dot{V} = -\frac{1}{2} e_I^T Q_0 e_I \leq 0 \tag{4.32}$$

This condition assures the global stability and boundedness of the Lyapunov function, but it does not guarantee the asymptotic stability as the time derivative of the Lyapunov function is only negative semi-definite. However, Barbalat's Lemma proves the convergence of the error ( $e_I$ ) to zero [33, 35].

## 4.2 Verification of the Online Estimation Algorithm

The simulation structure required to verify the derived online system identification algorithm is depicted in Fig. 4.3. Here, the block "Plant" is the fast engine model of the shaft dynamics of a STE given in Eqn: 3.24:

$$\begin{aligned}
\begin{bmatrix} \Delta \dot{N} \\ \Delta \ddot{N} \end{bmatrix} &= \begin{bmatrix} 0 & 1 \\ -1.8054 & -2.3360 \end{bmatrix} \begin{bmatrix} \Delta N \\ \Delta \dot{N} \end{bmatrix} + \begin{bmatrix} 0 \\ 4.8220 \end{bmatrix} \Delta V + \\
&\quad \begin{bmatrix} 0 & 0 \\ -0.1835 & -0.0001 \end{bmatrix} \begin{bmatrix} \Delta N \Delta V \\ \Delta N^2 \Delta V \end{bmatrix}
\end{aligned} \tag{4.33}$$

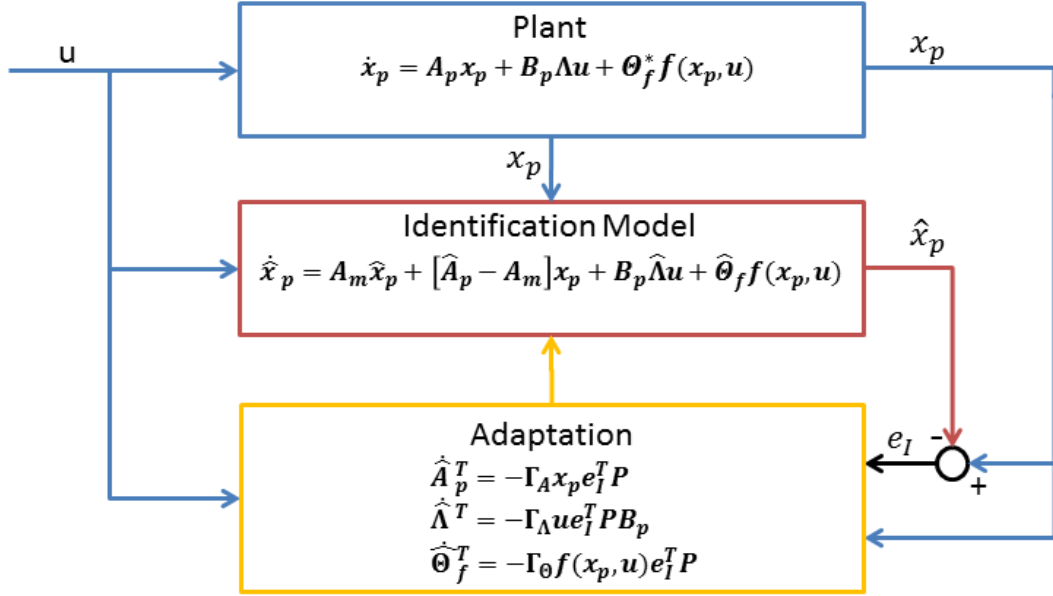


Figure 4.3: Online Parameter Estimation Structure for the Fast Engine Model

The second block in Fig. 4.3 represents the identification model defined in Eq. 4.7. This model was selected as a second order linear model with the parameters of  $\omega_n = 0.6 \text{ rad/s}$  for the natural frequency and  $\zeta = 1$  for the damping ratio. The system matrix ( $A_m$ ) of the identification model becomes:

$$A_m = \begin{bmatrix} 0 & 1 \\ -\omega_n^2 & -2\zeta\omega_n \end{bmatrix} = \begin{bmatrix} 0 & 1 \\ -0.36 & -1.2 \end{bmatrix} \quad (4.34)$$

The initial estimation values for the plant parameters are:

$$\hat{A}_p = \begin{bmatrix} 0 & 1 \\ -1 & -2 \end{bmatrix} \quad (4.35)$$

$$\hat{\Lambda} = 0.5 \quad (4.36)$$

$$\hat{\Theta}_f = \begin{bmatrix} 0 & 0 \\ 0 & 0 \end{bmatrix} \quad (4.37)$$

The third block in Fig. 4.3 is the adaptation block and it comprises the parameter update laws given in Eq. 4.31. The learning gains defined in these update law formu-



lations are:

$$\Gamma_A = \begin{bmatrix} 20 & 0 \\ 0 & 20 \end{bmatrix} \quad (4.38)$$

$$\Gamma_\Lambda = 3 \quad (4.39)$$

$$\Gamma_\Theta = \begin{bmatrix} 0.01 & 0 \\ 0 & 100 \end{bmatrix} \quad (4.40)$$

As seen in the fast engine model given in Eq. 4.33, the first rows of the matrices are known and constant because the first state ( $N$ ) of the model is the integration of the second state ( $\dot{N}$ ). Therefore, the first diagonal element of  $P$  matrix needs to be kept as small as possible.  $P$  matrix is chosen as:

$$P = \begin{bmatrix} 1e^{-5} & 0 \\ 0 & 1 \end{bmatrix} \quad (4.41)$$

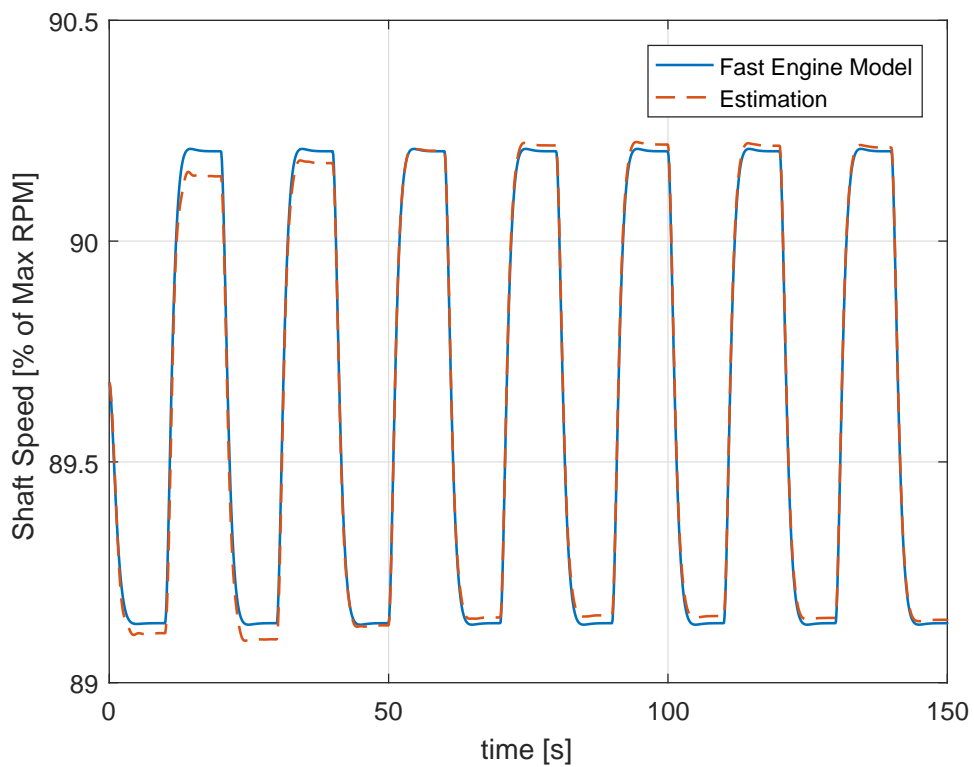


Figure 4.4: Shaft Speed Estimation Result of the Fast Engine Model

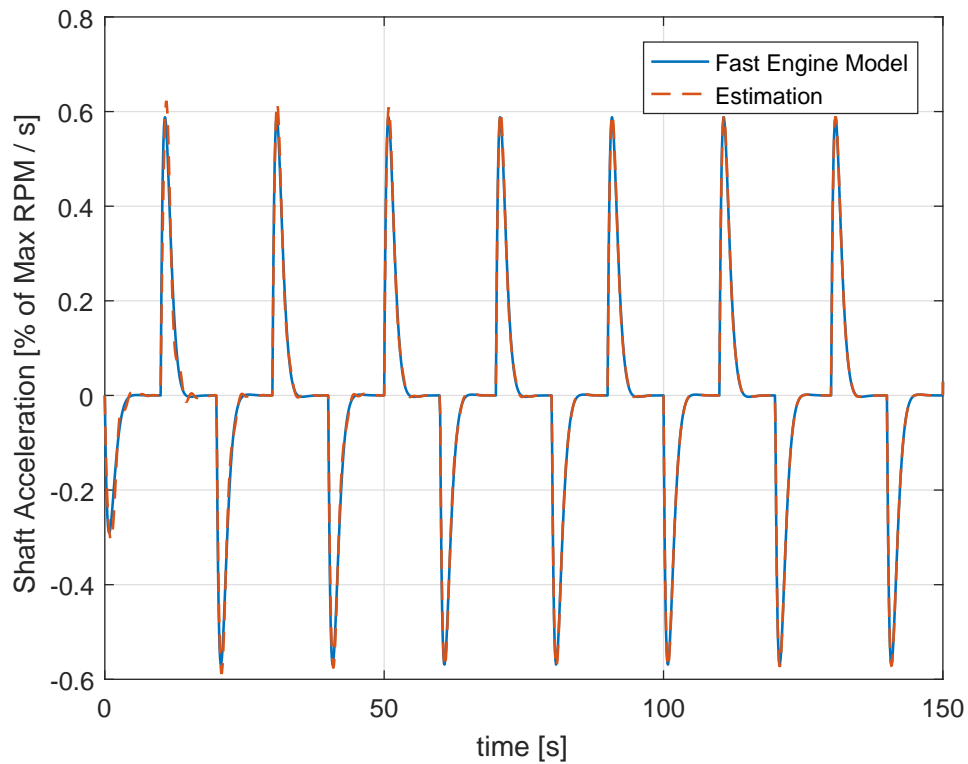


Figure 4.5: Shaft Acceleration Estimation Result of the Fast Engine Model

To converge the parameters to be identified to their ideal values and the error dynamics to zero, the input command ( $u$ ) must be persistently exciting [36, 37]. Here, the idea is to manipulate the error dynamics by using the periodic input signals. The square-shaped periodic signals because of having higher frequency component are much more suitable to excite the error dynamics. However, it is important to note that the periodic signal shape, amplitude, and frequency must be applicable for the system. Further details regarding the persistency of excitation can be found in Refs. [36–39].

For this system, the periodic square signal with  $\Delta V = 1V$  amplitude and  $0.05 Hz$  frequency was selected for the persistence of excitation. The shaft speed and acceleration results for the defined input signal are shown in Fig. 4.4 and Fig.4.5. Here, the blue line denotes the response of the fast engine model. As seen in Fig. 4.4, the shaft speed oscillates between around  $87\%N_{max}$  and  $92\%N_{max}$  during the simulation because of the persistence of excitation. Likewise, the red dashed line shows the identification model output (estimation). As seen in the results, the estimated shaft

speed and acceleration converge to the fast engine model states with time as expected.

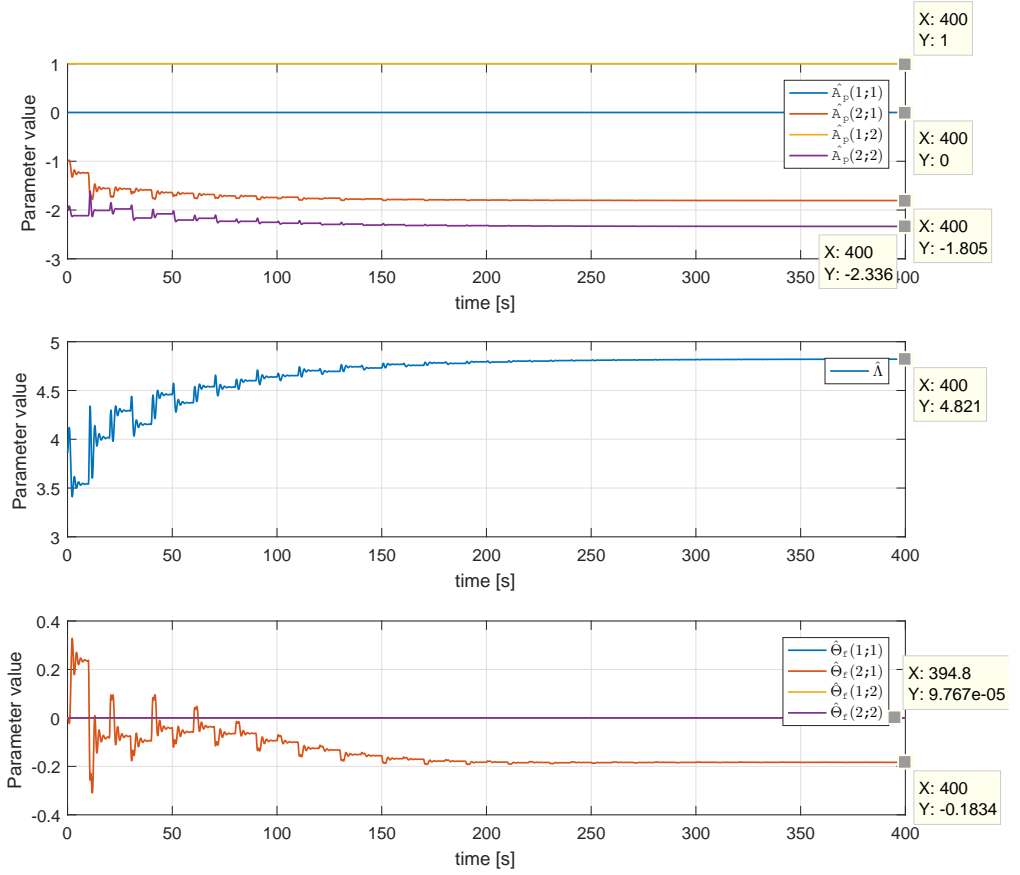


Figure 4.6: Parameter Estimation Results of the Fast Engine Model

The general trend of the estimated parameters is plotted in Fig. 4.6. The final values of the estimated parameters are found as below:

$$\hat{A}_p = \begin{bmatrix} 0 & 1 \\ -1.805 & -2.336 \end{bmatrix} \quad (4.42)$$

$$\hat{\Lambda} = 4.821 \quad (4.43)$$

$$\hat{\Theta}_f = \begin{bmatrix} 0 & 0 \\ -0.1834 & 9.767e^{-5} \end{bmatrix} \quad (4.44)$$

The results clearly show that the parameter convergences are succeeded and their final values are very close to the fast engine model parameters in Eq. 4.33. The obtained results have verified the correctness of the derived parameter update laws and the

online parameter estimation structure. After this point, the next step is to test this algorithm on the aero-thermal model.

### 4.3 Online Parameter Estimation of an Aero-Thermal Model

To test the algorithm, the fast engine model given in Fig 4.3 was replaced with the aero-thermal model as depicted in Fig 4.7. The engine is assumed as running on a test bench ( $U_0 = 0 \text{ m/s}$ ) at sea level. The ambient conditions ( $P_0, T_0$ ) are set  $288.15 \text{ K}$  and  $101325 \text{ Pa}$ , respectively. The same control input and initial parameters defined in the previous section (Sec. 4.2) were applied to the system.

The engine shaft speed and acceleration responses are plotted in Fig. 4.8 and Fig. 4.9, respectively. As seen in the results, the estimated states slowly converge to the aero-thermal model states over time. As seen from the general trend of the estimated parameters in Fig. 4.10, the parameter convergences occurred and the parameter estimations are:

$$\hat{A}_p = \begin{bmatrix} 0 & 1 \\ -1.901 & -2.458 \end{bmatrix} \quad (4.45)$$

$$\hat{\Lambda} = 4.979 \quad (4.46)$$

$$\hat{\Theta}_f = \begin{bmatrix} 0 & 0 \\ -0.1851 & 1.212e^{-6} \end{bmatrix} \quad (4.47)$$

The estimated parameters are very close to fast engine parameters given in Eq. 4.33. It was not expected to get the same estimation values because of the differences between the identification methods. The obtained results prove that the proposed structure for the online system identification of the shaft dynamics of a turbojet engine is true and the derived Lyapunov based parameter update laws are applicable to the similar turbojet engines.

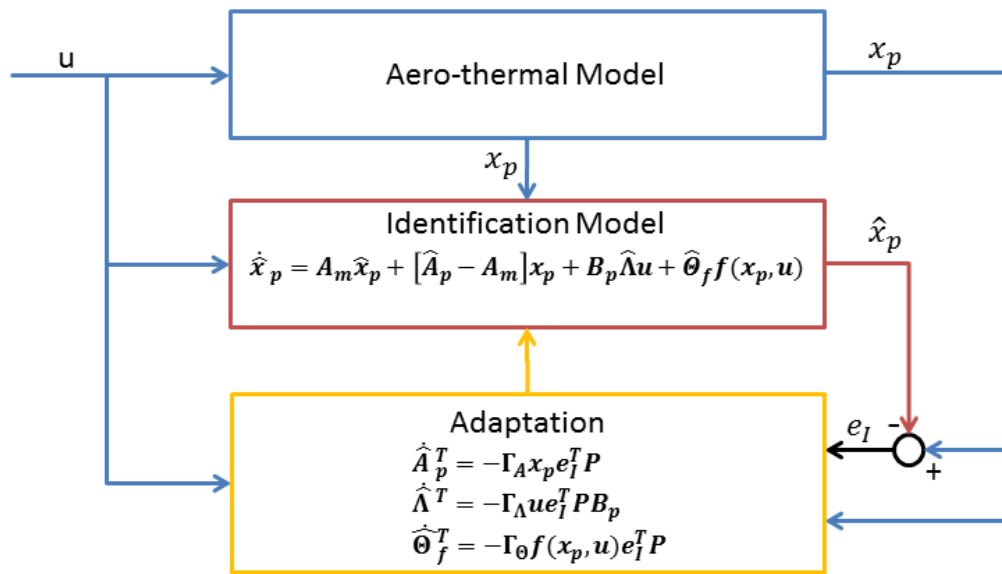


Figure 4.7: Online Parameter Estimation Structure for the Aero-Thermal Model

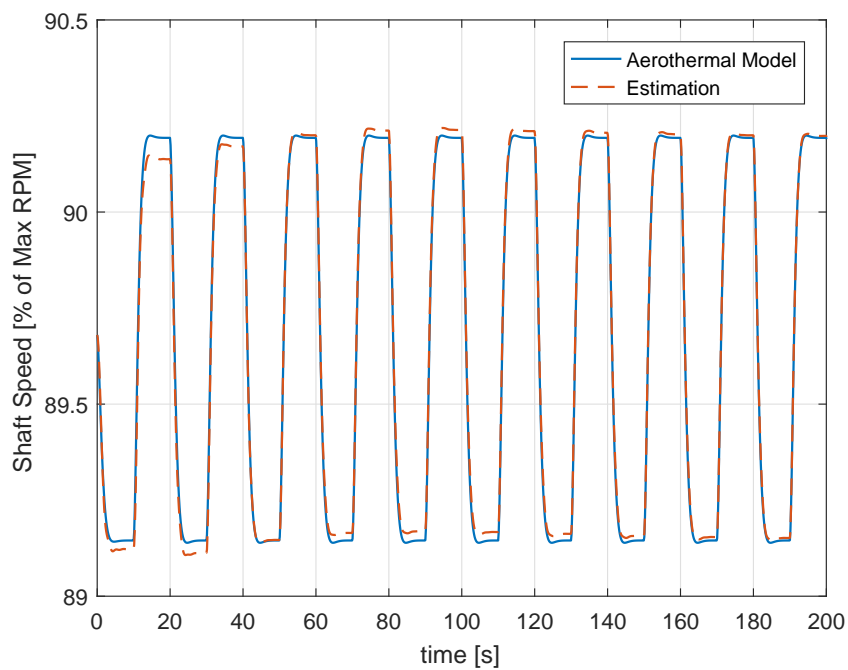


Figure 4.8: Shaft Speed Estimation Result of the Aero-Thermal Model

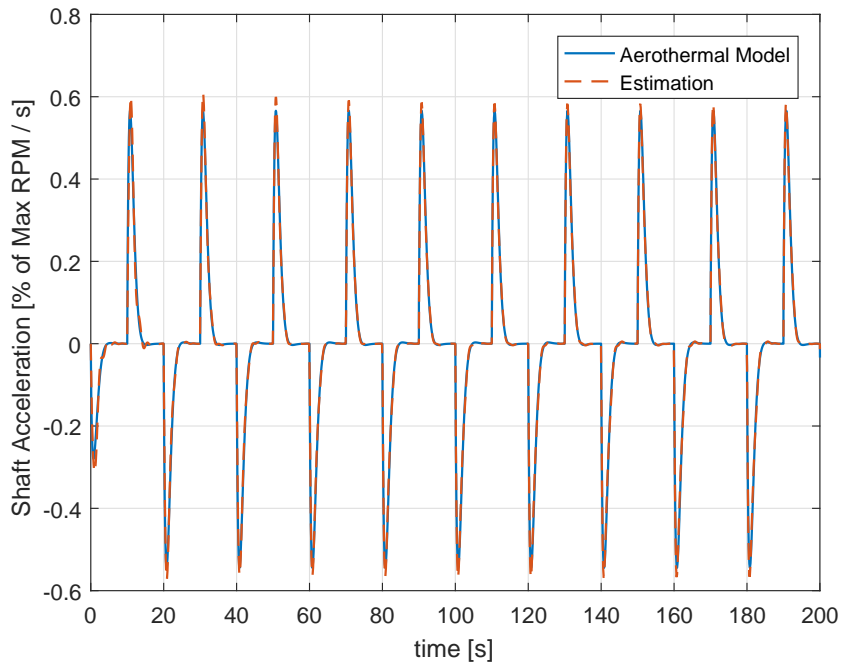


Figure 4.9: Shaft Acceleration Estimation Result of the Aero-Thermal Model

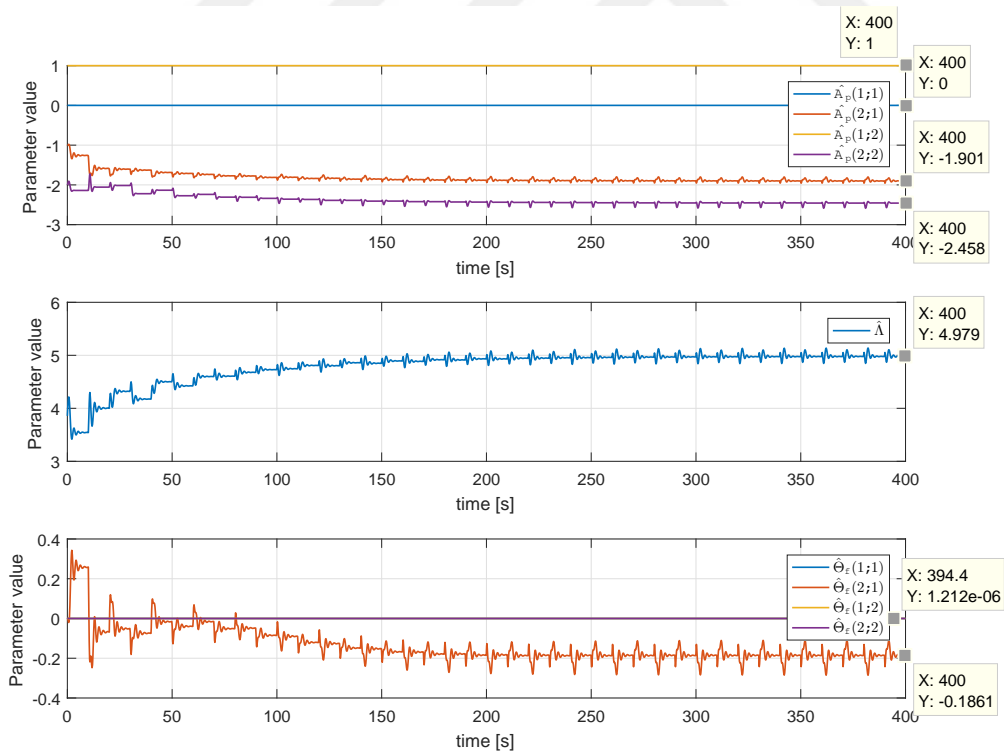


Figure 4.10: Parameter Estimation Results of the Aero-Thermal Model

## CHAPTER 5

### ADAPTIVE CONTROL OF SMALL TURBOJET ENGINES

The gas turbine engine parts, including feedback sensors, operate in harsh conditions such as high temperature, pressure, and vibration etc. These conditions can cause erosion, wear or tear on the engine parts. Any degradation on one of these engine parts or in the fuel system may change the engine dynamics or even cause the engine to malfunction. In such cases, advanced diagnostic and control techniques known as Failure Detection and Isolation (FDI), limit detection and protection, health monitoring, and adaptive control are used [1, 40, 41]. These techniques usually contain onboard/fast engine models compatible with the engine dynamics [1, 10, 42, 43]. Also, these models must be simple enough to be able to embed into onboard (built-in) computers such as ECUs or FADECs. The fast engine model proposed in Sec: 3.1 is compatible with these requirements and can be used as a fast engine model for small turbojet engines.

In this chapter, the online parameter estimation algorithm derived in Chp: 4 is integrated with an adaptive control. By this way, the ideal controller gains for the desired engine response can be achieved, and any deterioration on the controller performance can be compensated simultaneously. This approach is known as Self-Tuning Controller (STC) or Indirect Model Reference Adaptive Control (Indirect MRAC) in the literature [35, 44, 45]

The general structure of an indirect-MRAC is illustrated in Fig. 5.1. Here, the plant parameters are estimated simultaneously by using the error ( $e_I$ ) between the plant dynamics and identification model dynamics and then, these parameters are used to either compute controller gains or update controller gains.

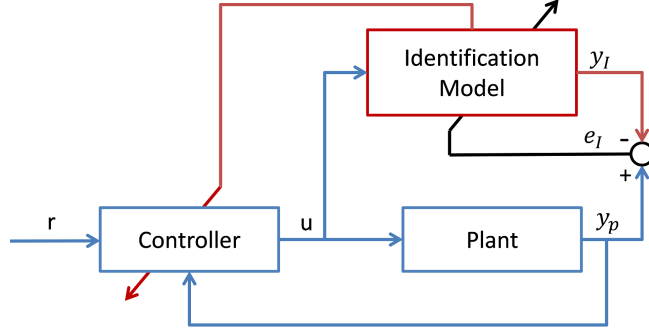


Figure 5.1: General Structure of an Indirect-MRAC

### 5.1 Indirect Model Reference Adaptive Control

The details of the indirect-MRAC structure are depicted in Fig. 5.2. As seen in the figure, the adaptive control structure is just added on the online system identification structure explained in Sec. 4.2. Similarly, the plant is the fast engine model for the shaft dynamics of an STE expressed with:

$$\dot{x}_p = A_p x_p + B_p \Lambda u + \Theta_f^* f(x_p, u) \quad (5.1)$$

and the identification model is:

$$\dot{\hat{x}}_p = A_m \hat{x}_p + [\hat{A}_p - A_m] x_p + B_p \hat{\Lambda} u + \hat{\Theta}_f f(x_p, u) \quad (5.2)$$

Here, the control input ( $u(t)$ ) and states ( $x_p(t)$ ) are received from the plant, and the plant parameter estimations ( $\hat{A}_p$ ,  $\hat{\Lambda}$ ,  $\hat{\Theta}_f$ ) are received from the adaptation block. Then, the plant state estimations ( $\hat{x}_p$ ) are evaluated. By using the identification error ( $e_I$ ), control input, and states; the adaptation block executes the parameter update laws derived in the previous chapter as:

$$\begin{aligned} \dot{\hat{A}}_p^T &= -\Gamma_A x_p e_I^T P \\ \dot{\hat{\Lambda}}^T &= -\Gamma_\Lambda u e_I^T P B_p \\ \dot{\hat{\Theta}}_f^T &= -\Gamma_\Theta f(x_p, u) e_I^T P \end{aligned} \quad (5.3)$$

The obtained plant parameter estimations ( $\hat{A}_p$ ,  $\hat{\Lambda}$ ,  $\hat{\Theta}_f$ ) from the integration of the equations above are then used to calculate the controller gains ( $K_c$ ). The control law is:

$$u = K_x x_p + K_r r + K_f f(x_p, u) \quad (5.4)$$



and substituting this into Eqn: 5.1, the closed-loop system dynamics becomes:

$$\dot{x}_p = A_p x_p + B_p \Lambda (K_x x_p + K_r r + K_f f(x_p, u)) + \Theta_f^* f(x_p, u) \quad (5.5)$$

then if this equation is rearranged, the following is achieved:

$$\dot{x}_p = (A_p + B_p \Lambda K_x) x_p + B_p \Lambda K_r r + (B_p \Lambda K_f + \Theta_f^*) f(x_p, u) \quad (5.6)$$

Last, the reference model representing the desired system response is defined as below:

$$\dot{x}_M = A_m x_m + B_m r \quad (5.7)$$

From here, the controller gains can be found from the matching condition between the closed loop dynamics (Eqn: 5.6) and reference model (Eqn: 5.7):

$$\begin{aligned} A_m &= A_p + B_p \Lambda K_x \\ B_m &= B_p \Lambda K_r \\ 0 &= B_p \Lambda K_f + \Theta_f^* \end{aligned} \quad (5.8)$$

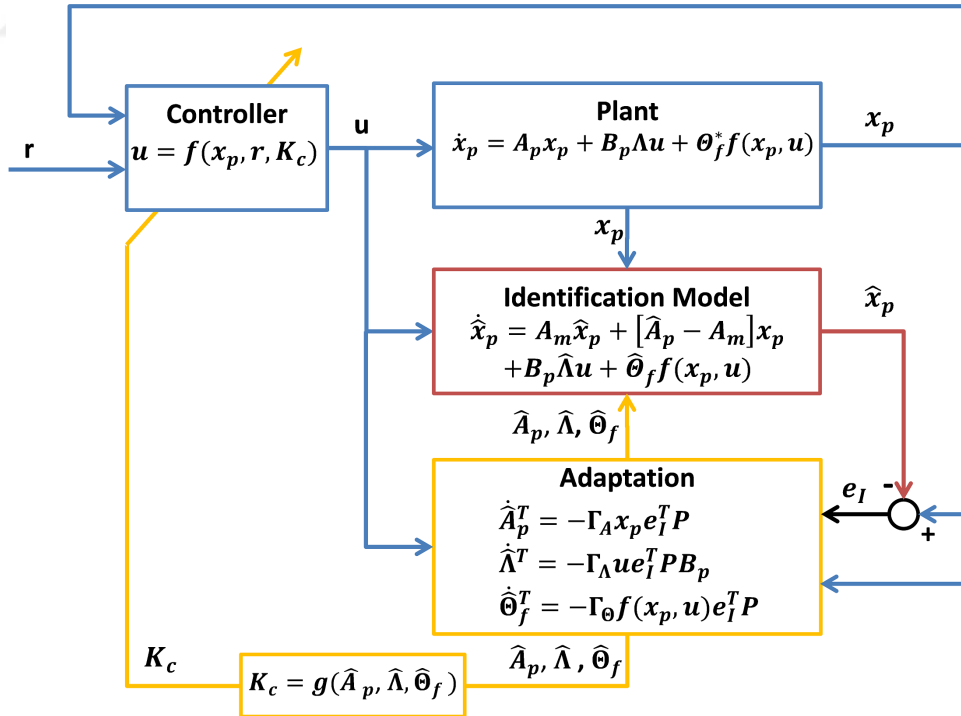


Figure 5.2: Detailed Structure of the Indirect-MRAC

Thus, the equations that give the ideal controller parameters are found as:

$$\begin{aligned} K_x &= -[B_p\Lambda]^{-1}[A_p - A_m] \\ K_r &= [B_p\Lambda]^{-1}B_m \\ K_f &= -[B_p\Lambda]^{-1}\Theta_f^* \end{aligned} \quad (5.9)$$

Here, if the actual plant parameters are replaced with the estimated plant parameters, the controller calculation laws become:

$$\begin{aligned} K_x &= -[B_p\hat{\Lambda}]^{-1}[\hat{A}_p - A_m] \\ K_r &= [B_p\hat{\Lambda}]^{-1}B_m \\ K_f &= -[B_p\hat{\Lambda}]^{-1}\hat{\Theta}_f \end{aligned} \quad (5.10)$$

These equations give the ideal controller gains for the desired system output. Thus, the adaptive control structure given in Fig. 5.2 can be updated as in Fig. 5.3. For the proof, these equations can be substituted into the control law given in Eqn. 5.4

$$u = -[B_p\hat{\Lambda}]^{-1}[\hat{A}_p - A_m]x_p + [B_p\hat{\Lambda}]^{-1}B_mr - [B_p\hat{\Lambda}]^{-1}\hat{\Theta}_ff(x_p, u) \quad (5.11)$$

and if this equation is applied to the identification model given in Eqn. 5.2:

$$\begin{aligned} \dot{\hat{x}}_p &= A_m\hat{x}_p + [\hat{A}_p - A_m]x_p + B_p\hat{\Lambda}(-[B_p\hat{\Lambda}]^{-1}[\hat{A}_p - A_m]x_p + [B_p\hat{\Lambda}]^{-1}B_mr \\ &\quad - [B_p\hat{\Lambda}]^{-1}\hat{\Theta}_ff(x_p, u)) + \hat{\Theta}_ff(x_p, u) \end{aligned} \quad (5.12)$$

and rearranged, the following is achieved:

$$\dot{\hat{x}}_p = A_m\hat{x}_p + B_mr \quad (5.13)$$

which means that the dynamics of the identification model is the same as the desired reference model dynamics specified in Eqn. 5.7. As seen in Fig. 5.1 or Fig. 5.2, there is no reference model directly implemented in the structural layout of the system. Instead, the identification model behaves like the desired reference model and the control error converges to zero simultaneously with the identification error in the same manner. However, in this control approach, the inverse of  $[B_p\hat{\Lambda}]$  has to exist. Also, if  $\hat{\Lambda}$  approaches to zero, the term  $[B_p\hat{\Lambda}]^{-1}$  in the controller calculation laws (Eqn:5.10) goes to the infinity and causes the controller gain calculation process to fail. To avoid this, a lower saturation limit must be set for the term  $\hat{\Lambda}$ . However, in this application, the term  $[B_p\hat{\Lambda}]$  is defined as a vector with two elements, so its inverse is not available.

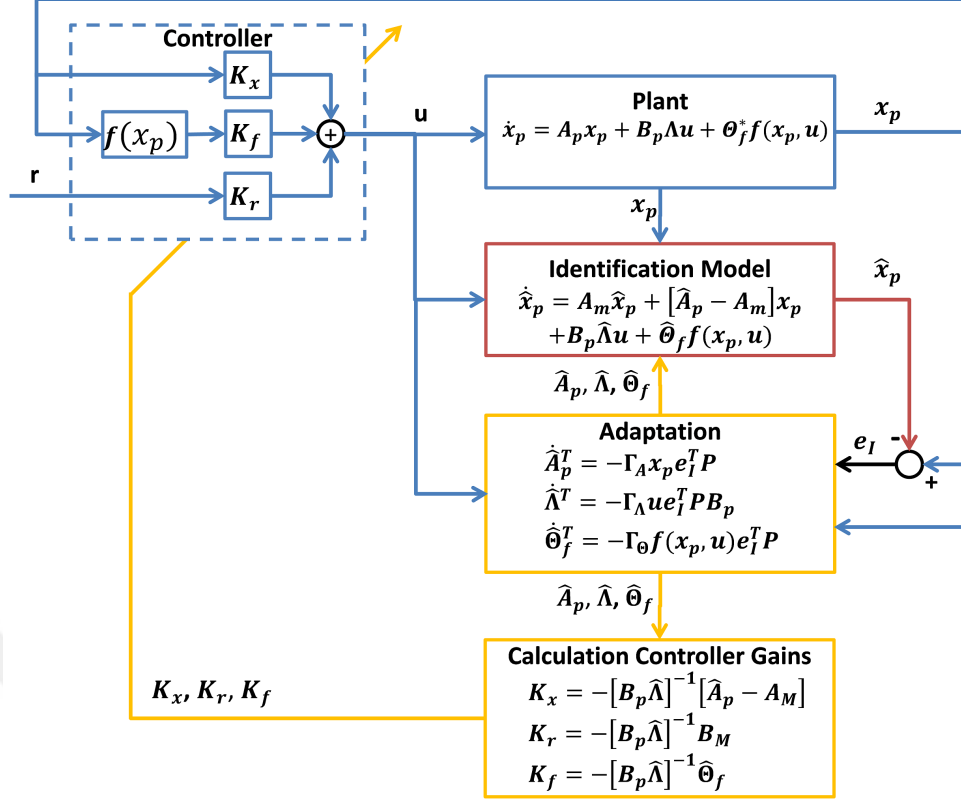


Figure 5.3: Detailed Structure of the Indirect-MRAC with Controller Calculation

As a solution, new adaptation laws can be defined for the controller gains. If the controller parameter calculation laws given in Eqn: 5.10 are rearranged:

$$\begin{aligned}
 0 &= \hat{A}_p - A_m + B_p \hat{\Lambda} K_x \\
 0 &= -B_m + B_p \hat{\Lambda} K_r \\
 0 &= \hat{\Theta}_f + B_p \hat{\Lambda} K_f
 \end{aligned} \tag{5.14}$$

The following additional errors can be defined [46]:

$$\begin{aligned}
 \epsilon_x &= \hat{A}_p - A_m + B_p \hat{\Lambda} K_x \\
 \epsilon_r &= -B_m + B_p \hat{\Lambda} K_r \\
 \epsilon_f &= \hat{\Theta}_f + B_p \hat{\Lambda} K_f
 \end{aligned} \tag{5.15}$$

By using the adaptation laws given in refs [46–48], new controller gain update laws

become:

$$\begin{aligned}
\dot{K}_x^T &= -\Gamma_x \epsilon_x^T B_p \\
\dot{K}_r^T &= -\Gamma_r \epsilon_r^T B_p \\
\dot{K}_f^T &= -\Gamma_f \epsilon_f^T B_p
\end{aligned} \tag{5.16}$$

The main advantage of this approach is that there is no need to define a saturation limit for  $\hat{\Lambda}$ .

## 5.2 Verification of the Indirect-MRAC Algorithm

The indirect-MRAC structure given in Fig. 5.3 is modified as shown in Fig. 5.4 by replacing the controller gain laws (Eqn. 5.16) for the simulation. Here, the plant is the fast engine model of the turbojet shaft dynamics given in Eqn. 3.24:

$$\begin{aligned}
\begin{bmatrix} \Delta \dot{N} \\ \Delta \ddot{N} \end{bmatrix} &= \begin{bmatrix} 0 & 1 \\ -1.8054 & -2.3360 \end{bmatrix} \begin{bmatrix} \Delta N \\ \Delta \dot{N} \end{bmatrix} + \begin{bmatrix} 0 \\ 1 \end{bmatrix} 4.8220 \Delta V + \\
&\quad \begin{bmatrix} 0 & 0 \\ -0.1835 & -0.0001 \end{bmatrix} \begin{bmatrix} \Delta N \Delta V \\ \Delta N^2 \Delta V \end{bmatrix}
\end{aligned} \tag{5.17}$$

The identification block in Fig. 5.4 also defines the reference model giving the desired response. For this model, a second-order linear model with parameters of  $\omega_n = 5.0 \text{ rad/s}$  and  $\zeta = 1$  is selected. The system matrix ( $A_m$ ) and input vector ( $B_m$ ) of the identification/reference model become:

$$A_m = \begin{bmatrix} 0 & 1 \\ -\omega_n^2 & -2\zeta\omega_n \end{bmatrix} = \begin{bmatrix} 0 & 1 \\ -25 & -10 \end{bmatrix} \tag{5.18}$$

and:

$$B_m = \begin{bmatrix} 0 \\ K\omega_n^2 \end{bmatrix} = \begin{bmatrix} 0 \\ 25 \end{bmatrix} \tag{5.19}$$

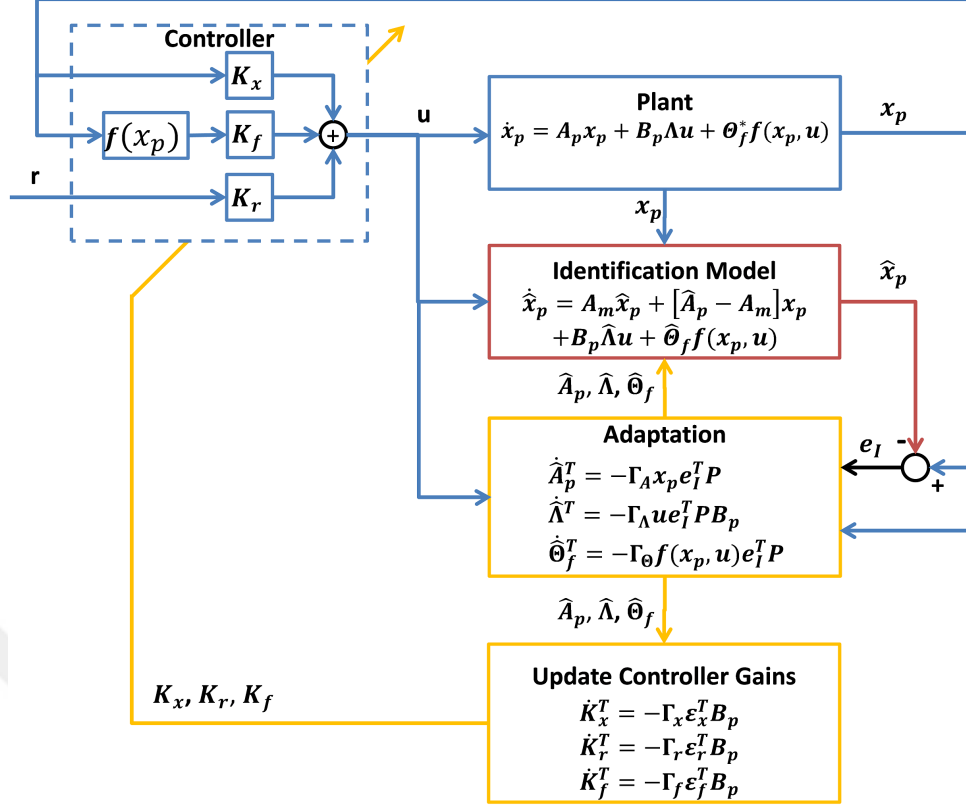


Figure 5.4: Detailed Structure of the Indirect-MRAC for Verification

The initial estimations of the plant parameters are:

$$\hat{A}_p = \begin{bmatrix} 0 & 1 \\ -0.5 & -1 \end{bmatrix} \quad (5.20)$$

$$\hat{\Lambda} = 4.3 \quad (5.21)$$

$$\hat{\Theta}_f = \begin{bmatrix} 0 & 0 \\ 0 & 0 \end{bmatrix} \quad (5.22)$$

$P$  matrix is chosen as:

$$P = \begin{bmatrix} 1e^{-5} & 0 \\ 0 & 1 \end{bmatrix} \quad (5.23)$$

The learning gains defined in the adaptation block are:

$$\Gamma_A = \begin{bmatrix} 3 & 0 \\ 0 & 3 \end{bmatrix} \quad (5.24)$$

$$\Gamma_\Lambda = 0.017 \quad (5.25)$$

$$\Gamma_{\Theta} = \begin{bmatrix} 0.004 & 0 \\ 0 & 8 \end{bmatrix} \quad (5.26)$$

The initial values of the controller parameters are:

$$K_x = \begin{bmatrix} 0 & 0 \end{bmatrix} \quad (5.27)$$

$$K_r = 0 \quad (5.28)$$

$$K_f = \begin{bmatrix} 0 & 0 \end{bmatrix} \quad (5.29)$$

The learning gains of the controller gain update laws are:

$$\Gamma_x = \begin{bmatrix} 0.1 & 0 \\ 0 & 0.1 \end{bmatrix} \quad (5.30)$$

$$\Gamma_r = 0.1 \quad (5.31)$$

$$\Gamma_f = \begin{bmatrix} 0.1 & 0 \\ 0 & 0.1 \end{bmatrix} \quad (5.32)$$

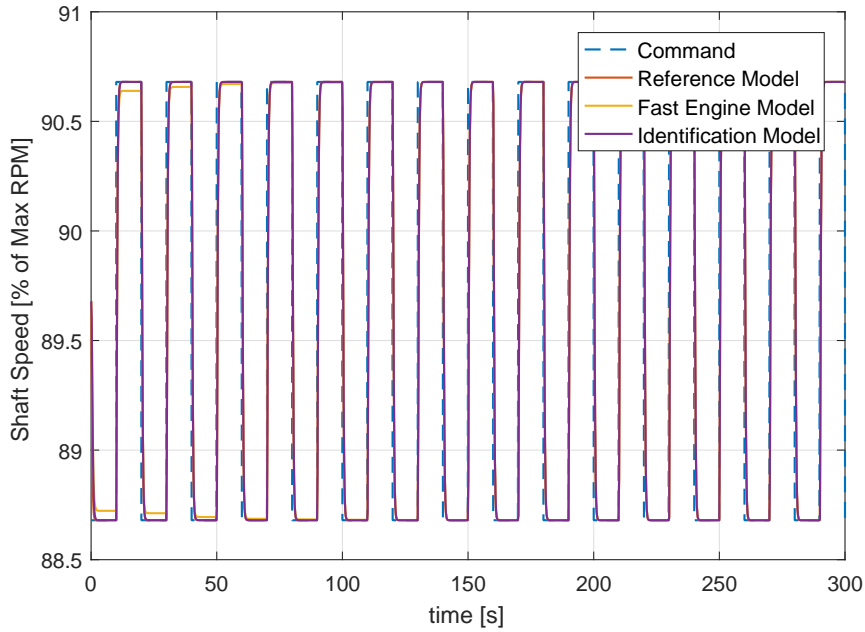


Figure 5.5: Indirect-MRAC Verification Result

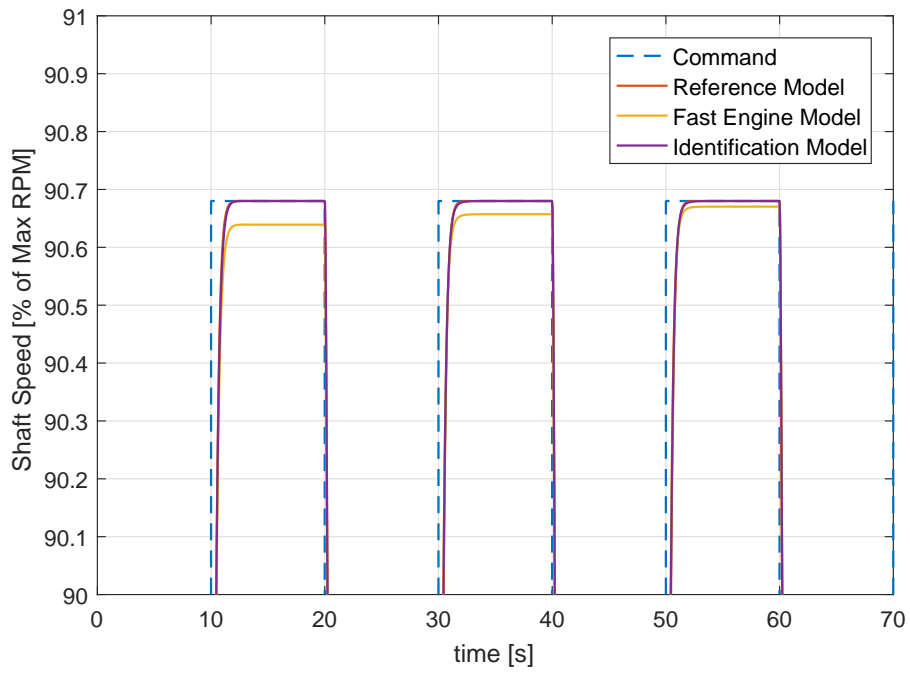


Figure 5.6: Indirect-MRAC Verification Result, Close View (first 20 s.)

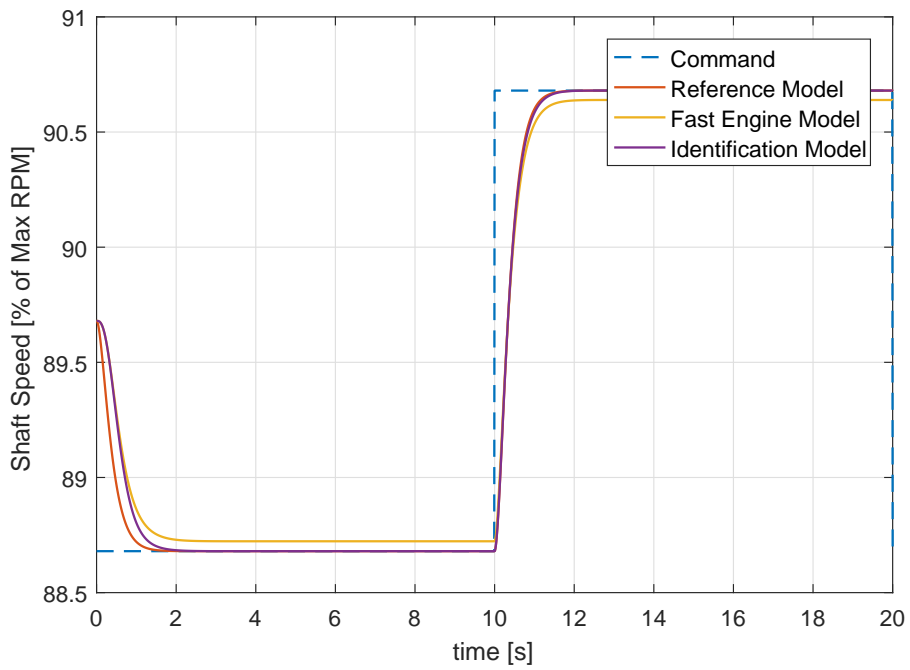


Figure 5.7: Indirect-MRAC Verification Result, Close View (first 70 s.)

For the simulation scenario, a square input signal with  $\Delta V = 1V$  amplitude and  $0.05Hz$  frequency is applied. The results obtained for 300 seconds of simulation time are shown in Fig. 5.5. Here, the blue dashed line is the shaft speed reference (or command). The red line denotes the reference model output representing the desired system response. The yellow line is the fast engine model or actual plant response, and the purple line is the identification model response. To distinguish the behaviours of the models clearly, the simulation results given in Fig. 5.6 are zoomed as it is shown in Fig. 5.6. As seen in the figure, the identification model follows the reference model. This means that the controller update algorithm finds the controller gains required to converge the identification model response to the reference model. The fast engine model response slowly approaches to the reference model response while the identification model parameters converge to the fast engine model parameters. Because at that time, the exact controller gains obtained from the identification model parameters also be ideal for the fast engine model. The general trend of the fast engine model can be seen better in Fig. 5.7.

The parameter estimations of the fast engine model are plotted in Fig. 5.8 and the final values of the parameter estimations are:

$$\hat{A}_p = \begin{bmatrix} 0 & 1 \\ -1.806 & -2.336 \end{bmatrix} \quad (5.33)$$

$$\hat{\Lambda} = 4.819 \quad (5.34)$$

$$\hat{\Theta}_f = \begin{bmatrix} 0 & 0 \\ -0.1846 & 0.0040 \end{bmatrix} \quad (5.35)$$

Here it is seen that the obtained values are very close to the exact parameters of the fast engine model given in Eqn. 5.17. Also, the general trend of the controller gains can be seen in Fig. 5.9. As it is highlighted in the figure, the final values of the controller gains are:

$$K_x = \begin{bmatrix} -4.813 & -1.59 \end{bmatrix} \quad (5.36)$$

$$K_r = -5.188 \quad (5.37)$$

$$K_f = \begin{bmatrix} -0.0008 & 0.03831 \end{bmatrix} \quad (5.38)$$



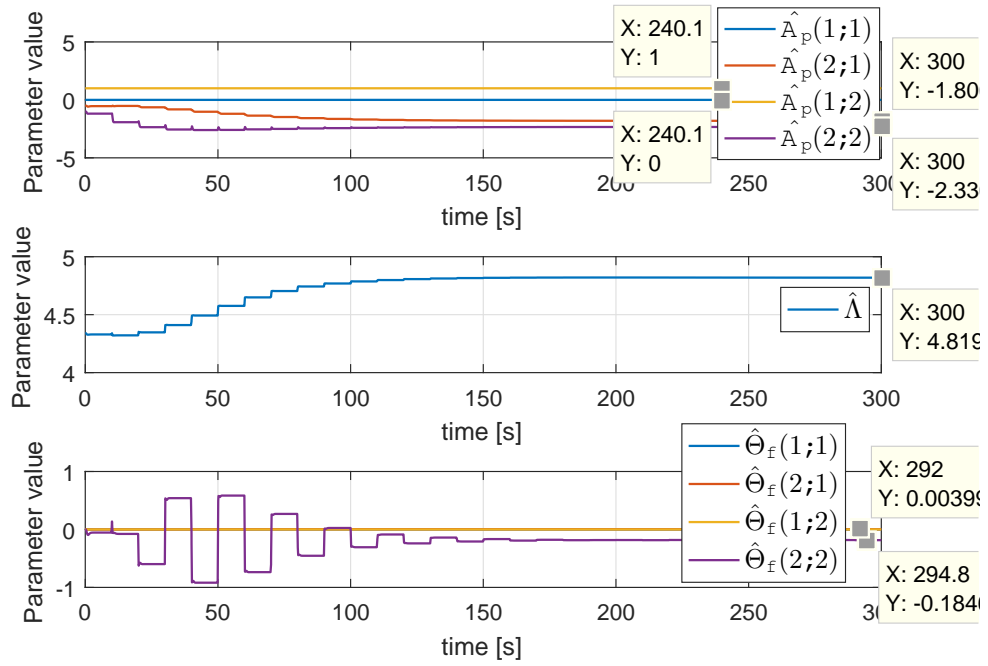


Figure 5.8: Indirect-MRAC Fast Engine Model Parameter Estimations

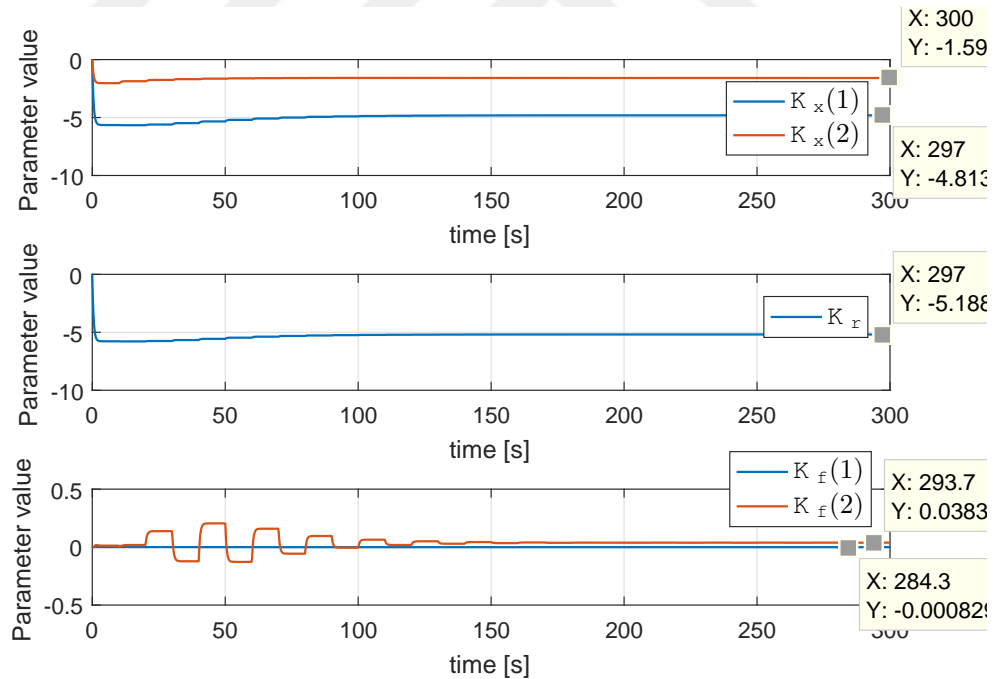


Figure 5.9: Indirect-MRAC Fast Engine Model Controller Gains

### 5.3 Testing of the Derived Indirect-MRAC

After verification of the indirect-MRAC algorithm, it is tested by using the aero-thermal engine model. For the simulation, the fast engine model plant given in Fig 5.3 was replaced with the aero-thermal turbojet model as depicted in Fig 5.10. The rest of the simulation structure is kept the same. The initial conditions of the aero-thermal turbojet model are 101325 Pa and 288.15 K for the ambient air, and  $U_0 = 0$  m/s for the airspeed at the inlet. The same operational conditions and shaft speed command defined in Sec:5.2 are applied. The other initial values of the indirect-MRAC algorithm are given as follows.

The reference model:

$$A_m = \begin{bmatrix} 0 & 1 \\ -25 & -10 \end{bmatrix} \quad (5.39)$$

$$B_m = \begin{bmatrix} 0 \\ 25 \end{bmatrix} \quad (5.40)$$

The initial parameter estimations of the plant:

$$\hat{A}_p = \begin{bmatrix} 0 & 1 \\ -0.5 & -1 \end{bmatrix} \quad (5.41)$$

$$\hat{\Lambda} = 4.3 \quad (5.42)$$

$$\hat{\Theta}_f = \begin{bmatrix} 0 & 0 \\ 0 & 0 \end{bmatrix} \quad (5.43)$$

The  $P$  matrix:

$$P = \begin{bmatrix} 1e^{-5} & 0 \\ 0 & 1 \end{bmatrix} \quad (5.44)$$

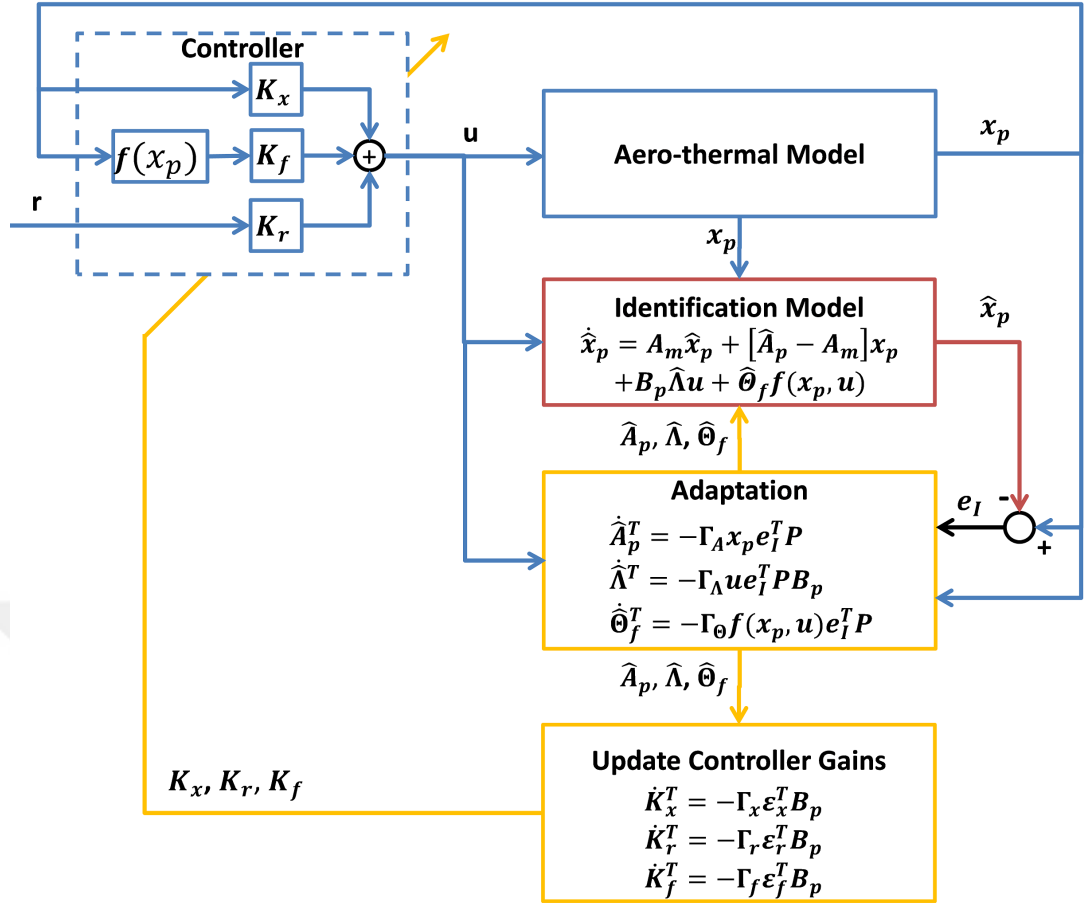


Figure 5.10: Detailed Structure of the Indirect-MRAC for Test

The learning gains of the adaptation block:

$$\Gamma_A = \begin{bmatrix} 3 & 0 \\ 0 & 3 \end{bmatrix} \quad (5.45)$$

$$\Gamma_\Lambda = 0.015 \quad (5.46)$$

$$\Gamma_\Theta = \begin{bmatrix} 0.02 & 0 \\ 0 & 0.1 \end{bmatrix} \quad (5.47)$$

The initial values of the controller parameters:

$$K_x = \begin{bmatrix} 0 & 0 \end{bmatrix} \quad (5.48)$$

$$K_r = 0 \quad (5.49)$$

$$K_f = \begin{bmatrix} 0 & 0 \end{bmatrix} \quad (5.50)$$

The learning gains of the controller gain update laws:

$$\Gamma_x = \begin{bmatrix} 0.1 & 0 \\ 0 & 0.1 \end{bmatrix} \quad (5.51)$$

$$\Gamma_r = 0.1 \quad (5.52)$$

$$\Gamma_f = \begin{bmatrix} 0.1 & 0 \\ 0 & 0.1 \end{bmatrix} \quad (5.53)$$

The shaft speed responses of the reference model, identification model, and aero-thermal model are compared in Fig. 5.11. To reveal the model response differences better, the simulation results of the first 20 seconds of simulation time are depicted in Fig. 5.12. Here, the shaft speed command and reference model output are denoted by the blue dashed line and red line, respectively. As seen in the figure, the identification model (purple line) approaches the reference model over time and the aero-thermal model (yellow line) follows the identification model with a delay. The convergence of the aero-thermal model is plotted in Fig. 5.13. The last 50 seconds of simulation time are shown in Fig. 5.14. As seen in the figure, the aero-thermal model gives the desired response.

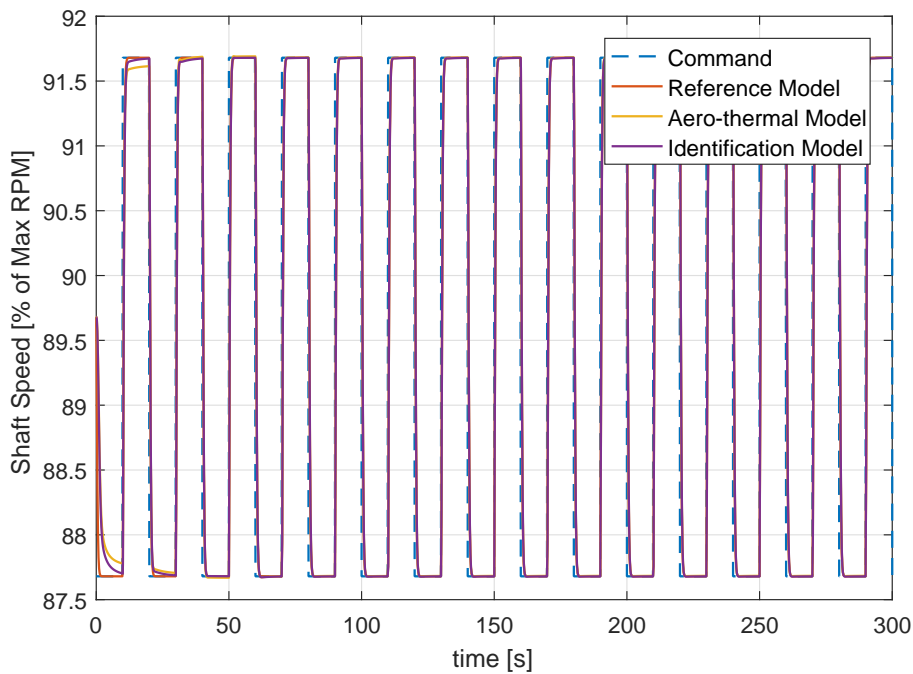


Figure 5.11: Indirect-MRAC Test Result

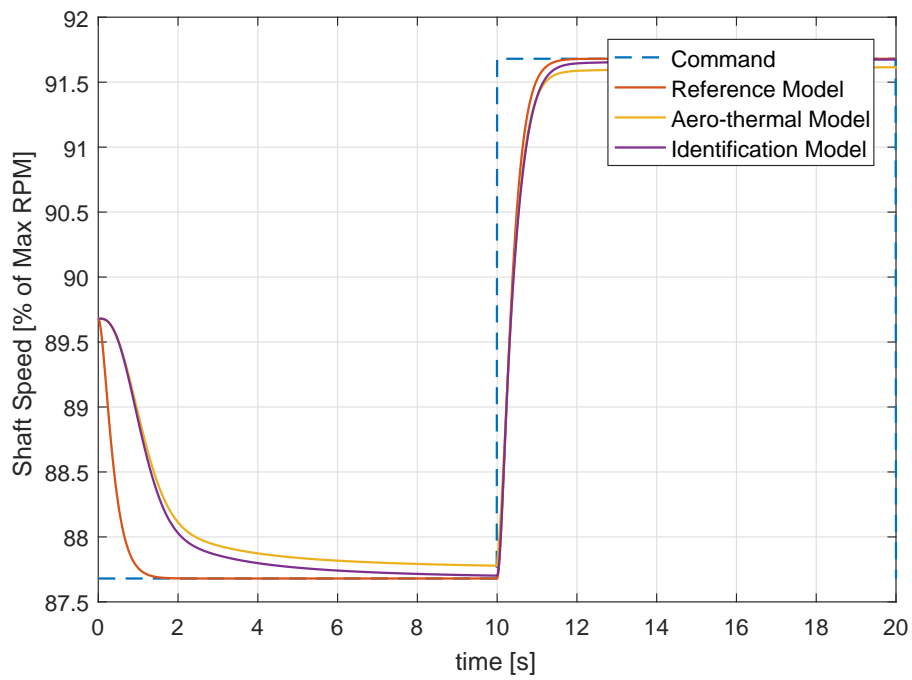


Figure 5.12: Indirect-MRAC Test Result (first 20 s.)

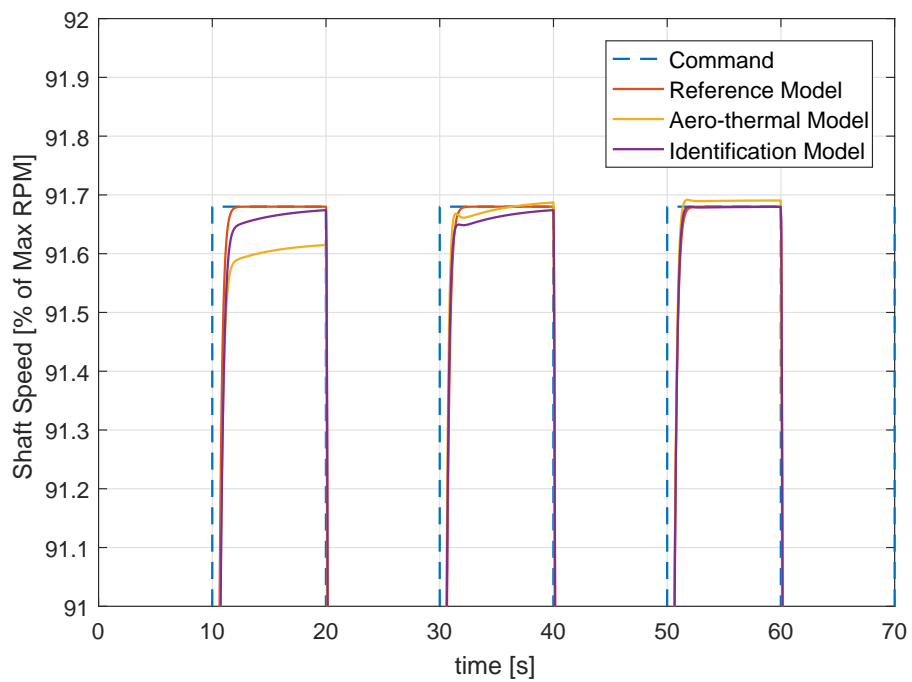


Figure 5.13: Indirect-MRAC Test Result (first 70 s.)

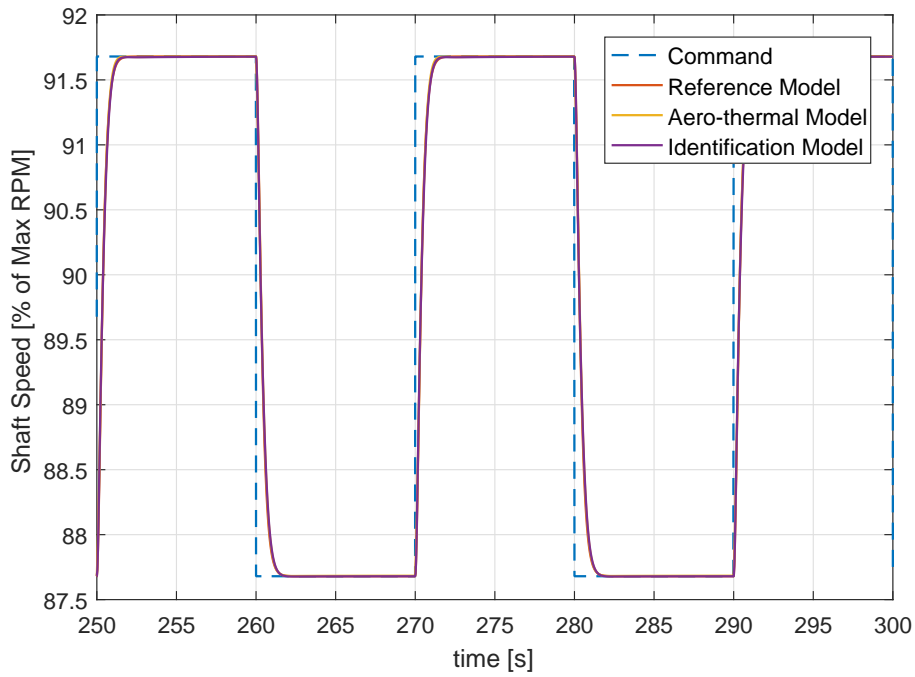


Figure 5.14: Indirect-MRAC Test Result (last 50 s.)

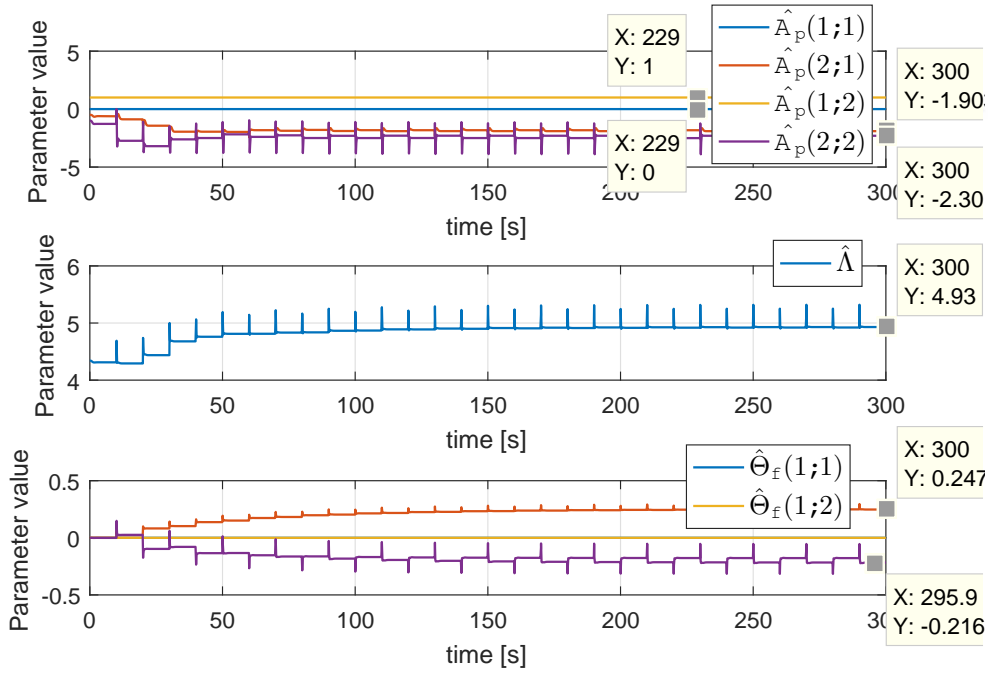


Figure 5.15: Indirect-MRAC Aero-Thermal Model Parameter Estimations

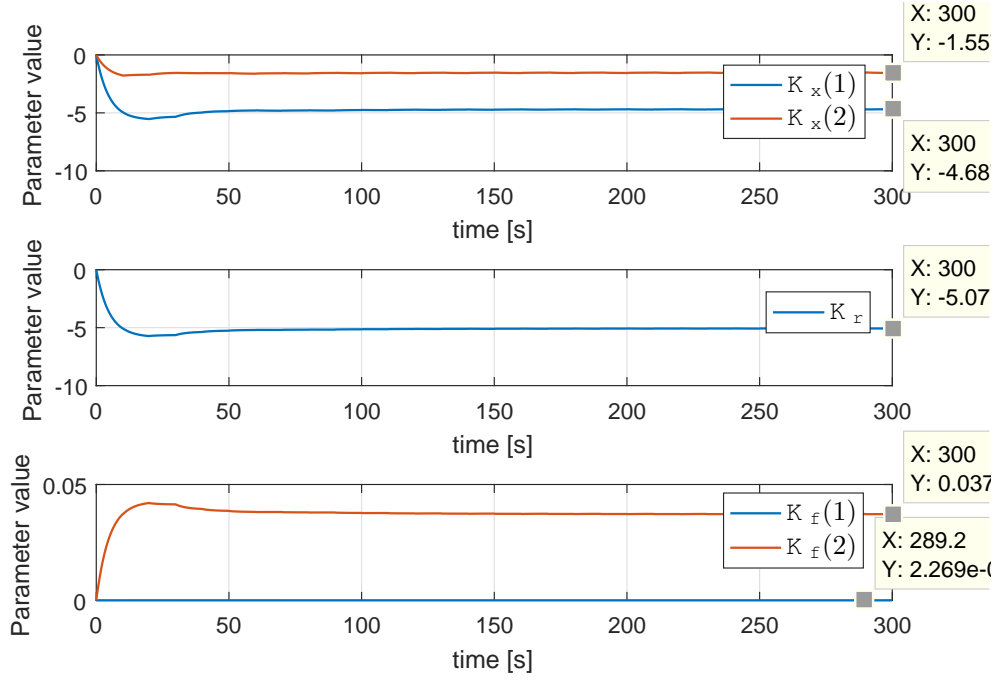


Figure 5.16: Indirect-MRAC Aero-Thermal Model Controller Gains

The parameter estimations of the aero-thermal model are depicted in Fig. 5.15. The followings are the final values of the estimated parameters:

$$\hat{A}_p = \begin{bmatrix} 0 & 1 \\ -1.903 & -2.301 \end{bmatrix} \quad (5.54)$$

$$\hat{\Lambda} = 4.93 \quad (5.55)$$

$$\hat{\Theta}_f = \begin{bmatrix} 0 & 0 \\ -0.2477 & -0.2164 \end{bmatrix} \quad (5.56)$$

Here, the obtained values are close to given values in Eqn. 5.17. Therefore, as highlighted in Fig. 5.16, the final controller parameters are also close to the obtained results in Eqn:5.2. The final controller values are:

$$K_x = \begin{bmatrix} -4.687 & -1.557 \end{bmatrix} \quad (5.57)$$

$$K_r = -5.071 \quad (5.58)$$

$$K_f = \begin{bmatrix} 2.269e^{-5} & 0.0372 \end{bmatrix} \quad (5.59)$$

## 5.4 Testing of the Obtained Nonlinear Controller

To reveal the performance of the nonlinear controller using the ideal controller gains obtained in the previous section, it is tested under different shaft speed scenarios. Figure 5.17 shows the response of the aero-thermal model to a staircase shaft speed command between  $70\%N_{max}$  and  $100\%N_{max}$ . As seen in the figure, the engine response follows the reference model and gives the same transient behavior for each step command. In Fig. 5.18, the engine response to the sinusoidal shaft speed command with  $10\%\Delta N$  amplitude and  $0.05Hz$  frequency is plotted. In the last scenario, to see the controller performance to the high-frequency commands at different operational levels, a sinusoidal signal with  $1\%\Delta N$  amplitude and  $1Hz$  frequency is added on the same staircase command in the first test. As seen in Figs. 5.18 and 5.19, the engine shows the desired response for both high-frequency and low-frequency shaft speed commands at different operational levels.

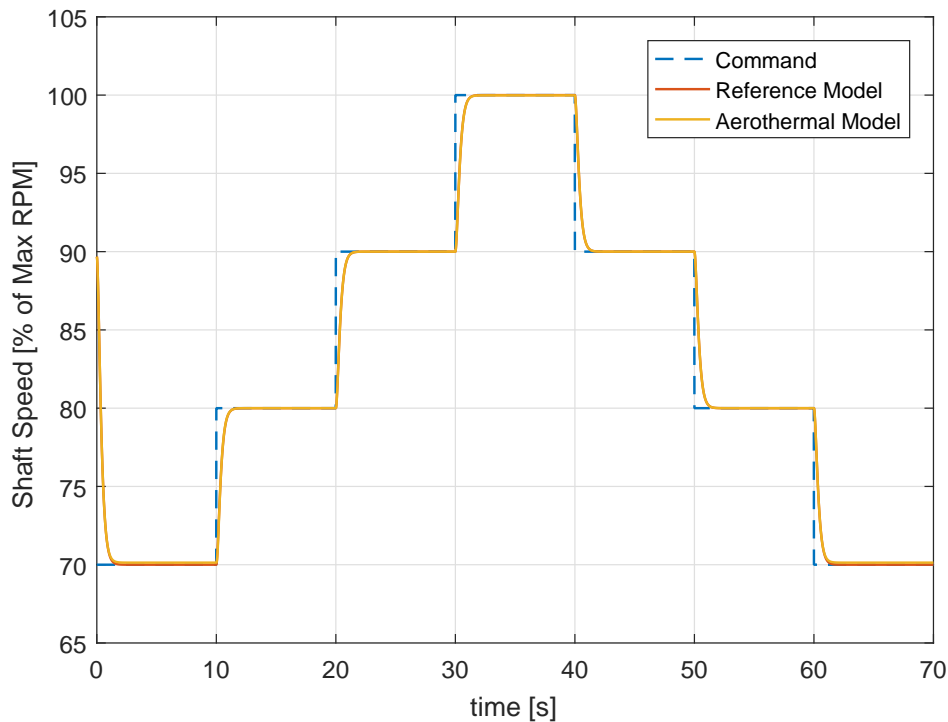


Figure 5.17: Nonlinear Controller Performance Test-1



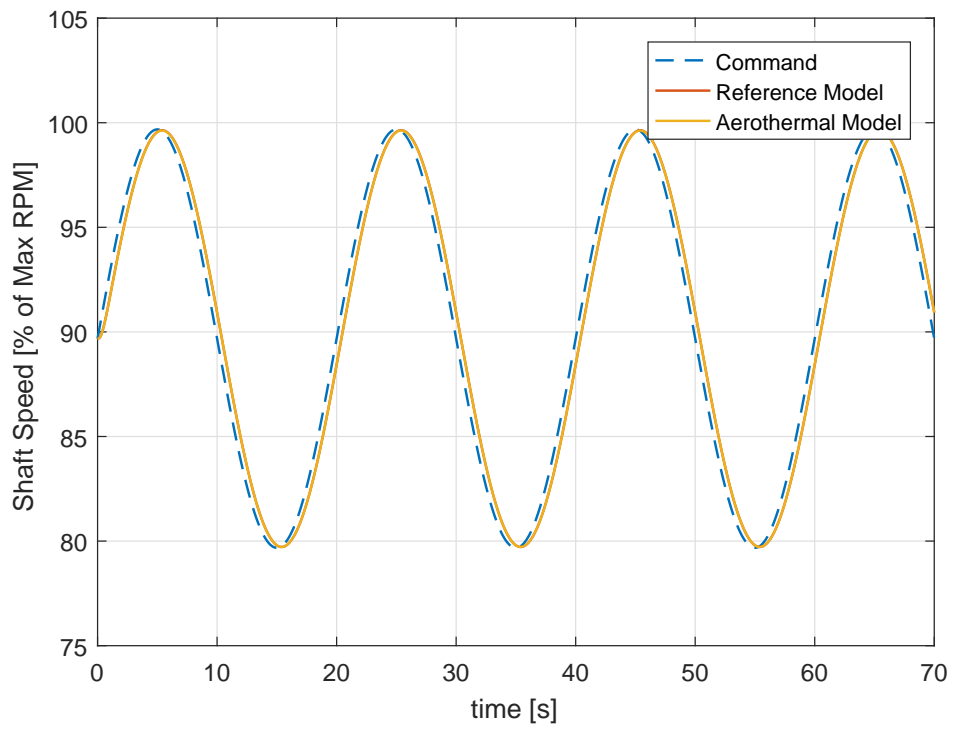


Figure 5.18: Nonlinear Controller Performance Test-2

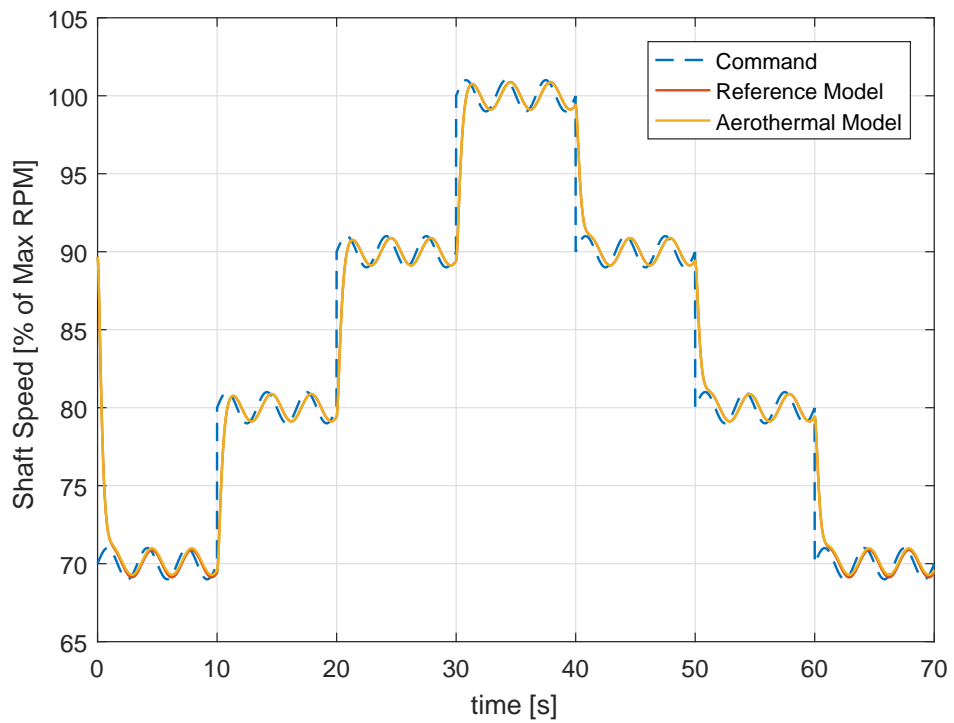


Figure 5.19: Nonlinear Controller Performance Test-3



## CHAPTER 6

### ADVANTAGES AND DISCUSSIONS

As shown in the first chapter, the gas turbines are inherently nonlinear machines. In addition, driving a gas turbine with a gear-type fuel pump rather than an FMU brings an additional nonlinearity to the overall system. This new concept makes the conventional gas turbine control methods based on the classical control approaches inconvenient. In this chapter, to demonstrate the main advantages of the derived indirect-MRAC method, it is compared with a classical controller in several conditions including a fault scenario.

Because of being the most preferred and known method, PID control is selected as the linear control method to compare with the derived indirect-MRAC [1]. The controller gains are adjusted as  $P = 2, I = 1, D = 0.5$  for the equilibrium point of the aero-thermal model at  $89.68 \%N_{max}$ . The same reference command is connected to both the aero-thermal model with PID controller and the aero-thermal model with indirect-MRAC for the simulation. Figure 6.1 shows the comparison results with the applied shaft speed command and the desired response. As seen in the figure, the performance of the PID controller is favorable for the rising edge of the reference command. However, that is not the same for the falling edge. Because, as mentioned before, the system to be controlled have nonlinear behavior and controlling this kind of a system with a linear method such as a PID controller is not adequate. To demonstrate the performance of the PID controller better, a staircase shaft speed command between  $70 \%N_{max}$  and  $100 \%N_{max}$  is applied to both systems.

As shown in Fig. 6.2, the PID controller exhibits poor performance outside its design region. To overcome this problem, the gain scheduling technique is mostly used [10, 28]. In this technique, the controller gains are determined separately for each specific

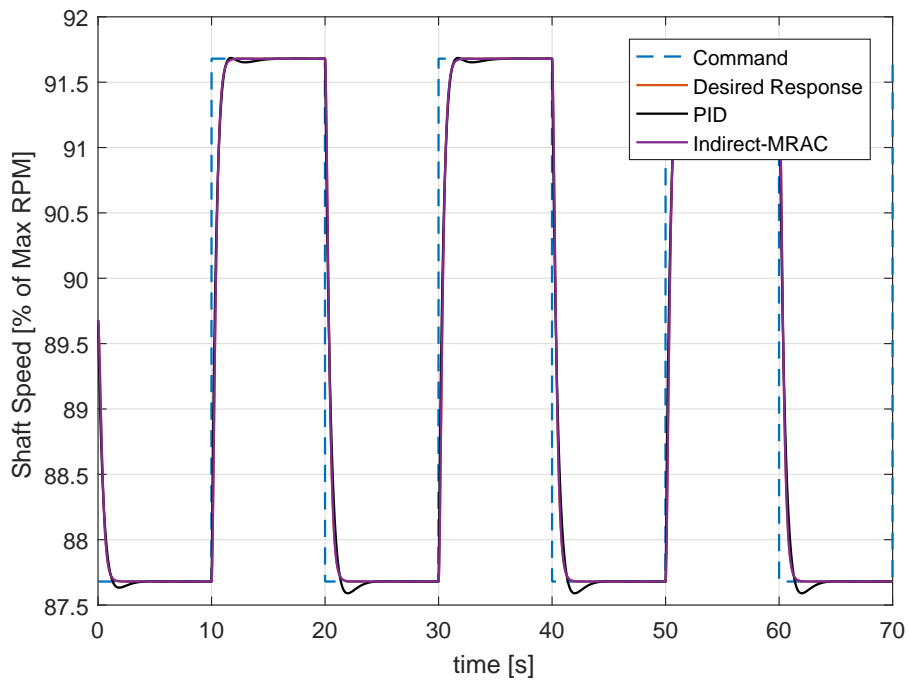


Figure 6.1: Comparison Scenario-1

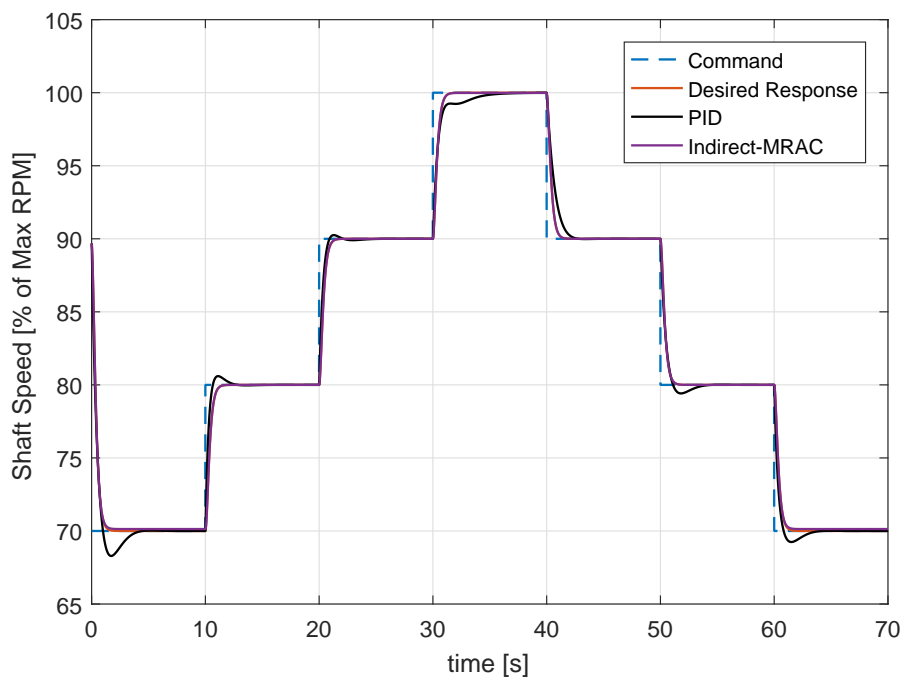


Figure 6.2: Comparison Scenario-2

operational region and condition of the engine including acceleration/deceleration cases. And then, the ideal controller gains are interpolated regarding the shaft speed and operating condition of the engine. However, these design procedures require detailed test campaigns that may be time-consuming. In addition, the manufacturing tolerances or modifications on the turbojet engine parts and fuel pump may cause repetition of these design procedures from the beginning.

On the other hand, the indirect-MRAC has a nonlinear controller structure. As seen in Fig. 6.2, it shows the same performance for the entire operational shaft speed range of the engine. Also with the help of the online parameter estimation part, the controller can adapt itself to the actual engine condition. This advantage eliminates the need for the time-consuming test campaigns.

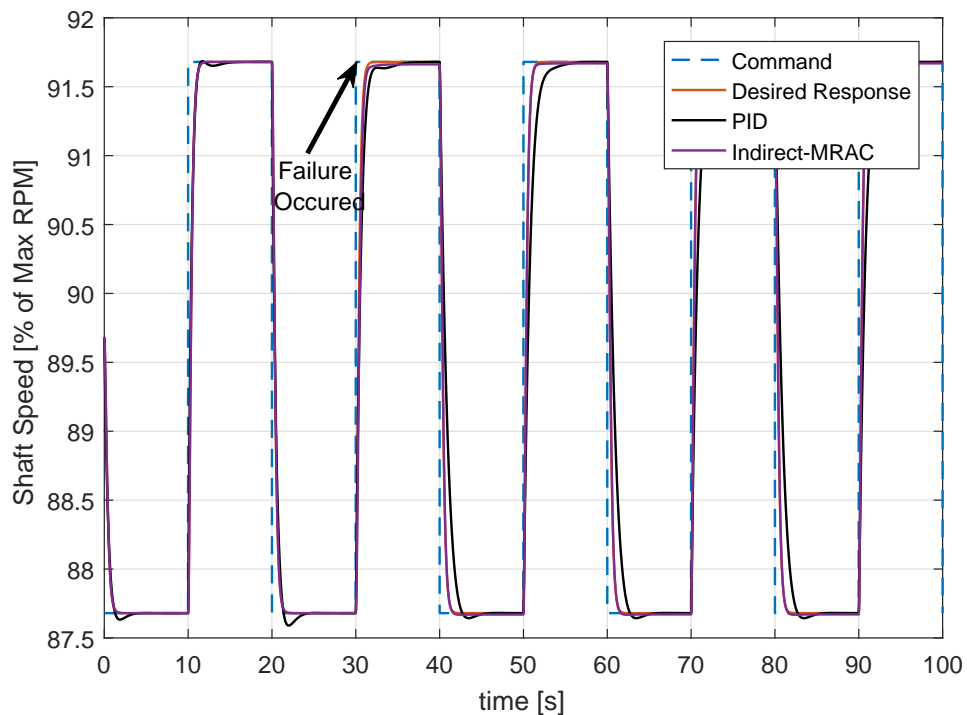


Figure 6.3: Failure Scenario, Shaft Speed Results

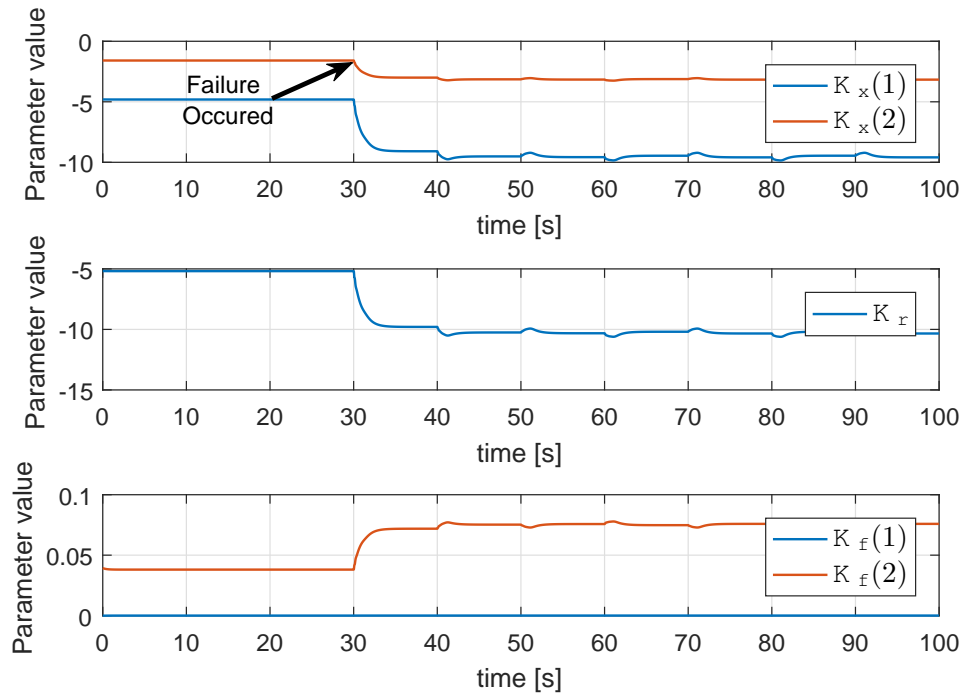


Figure 6.4: Failure Scenario, Controller Gains

To demonstrate the other advantages of the derived indirect-MRAC, both controllers are tested under a possible malfunction scenario. In the scenario, it is assumed that the efficiency of the fuel pump (fuel flow rate/supply voltage) decreases by half at 30th second. This efficiency (or effectiveness) was symbolized by  $\Lambda$  in the approximate model.

Figure 6.3 shows the simulation results for the reference command used at the previous test. As labeled in the figure, the failure occurs at 30th second and then, the PID controller shows a loose performance. However, the indirect-MRAC controller adapts itself to the actual engine condition and maintains the desired engine response. This behavior can also be seen in the controller gain results given in Fig. 6.4. Last, the controller effectiveness gain is plotted in Fig. 6.5. As it is shown in the figure, the gain  $\Lambda$  converges to half of its initial value. It is obvious that this gain provides very useful information about the health status of the fuel pump (or fuel system). For instance, the wear on the fuel pump gears decreases its effectiveness during the operation. The maintenance or replacement period of the fuel pump can be determined

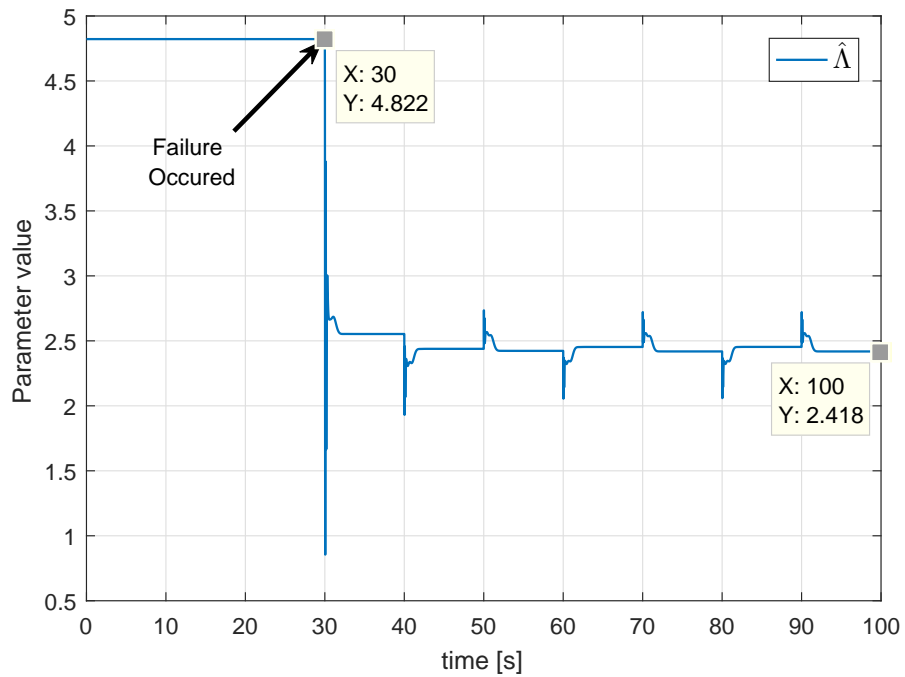


Figure 6.5: Failure Scenario, Control Effectiveness

by monitoring this effectiveness gain. This may be another application area of the indirect-MRAC structure for the further studies. Consequently, the indirect-MRAC does not only adapt itself to the actual operating condition but also gives very useful information about the engine parameters and health status.





## CHAPTER 7

### CONCLUSION

In this study, both offline and online system identification methods were applied to a small gas turbine engine (STE) equipped with a gear-type fuel pump to obtain its fast engine model. Then, the derived online parameter estimation method was converted to an indirect model reference adaptive control (Indirect-MRAC). In case of a failure, it was proved that the indirect-MRAC can adapt itself and, keeps the desired controller performance and also, the included online parameter estimation part provides very useful information about the health status of the engine.

First, a high fidelity aero-thermal turbojet model was developed in MATLAB-Simulink to generate the required realistic engine data. The developed aero-thermal model was then validated with the experimental results found in the literature.

Second, a fast model was proposed to simulate the shaft dynamics of a turbojet. The structure of the fast engine model was kept simple to be able to embed even on on-board computers that have low computational power. Then, the least squares method was used for the parameter estimation of this model. Next, the obtained model was tested under different fuel pump command scenarios. For the verification, the same identification procedure was repeated with real engine data. The obtained results show that the proposed fast engine model structure is capable of simulating the shaft dynamics of a turbojet engine over its operational range.

Third, an online estimation algorithm using the same fast engine model structure was derived. The convergence and boundedness of the parameter update laws were proved by using Lyapunov stability theory. The algorithm was first applied to the fast model and then verified on the aero-thermal turbojet model. The simulation results depict

that the parameter convergences occurred and the estimated parameter values were quite close to the parameters obtained from the least squares algorithm.

Fourth, for the shaft speed control of a small turbojet engine, an indirect-model reference adaptive control (indirect-MRAC) based on the derived online parameter estimation algorithm was applied. Firstly, the controller gain update laws were derived. It was also shown that the identification model acts as a reference model that inherently provides the desired response. Then, the algorithm was applied to both approximate and aero-thermal models. The simulation results prove that the indirect-MRAC finds the ideal controller gains providing the desired system output while estimating the parameters of the controlled system simultaneously.

Last, the derived indirect-MRAC algorithm was compared with a PID controller under various test conditions, including a failure scenario. Due to its non-linear control structure, indirect-MRAC followed the desired control response more closely than the PID controller. It was also shown that indirect-MRAC can adapt itself and maintain the desired control performance under fault conditions. Moreover, it can provide very useful data about the health status of the engine using the online parameter estimation algorithm.

Consequently, the parameter estimation and control methods expressed in this study are not limited to a gas turbine application field, but also can be applied to any control system especially actuated with a nonlinear actuator for the advanced control and diagnostic purposes such as adaptive control, limit detection and protection, failure detection and isolation (FDI) etc.

## REFERENCES

- [1] L. Jaw and J. Mattingly, *Aircraft Engine Controls: Design, System Analysis, and Health Monitoring*. AIAA education series, American Institute of Aeronautics and Astronautics, 2009.
- [2] “This article is about jet or rocket-powered flying devices.” <https://en.wikipedia.org/wiki/Jetpack>. Accessed: 2018-07-24.
- [3] D. Barbeau, “A family of small, low cost turbojet engines for short life applications,” in *ASME 1981 International Gas Turbine Conference and Products Show*, pp. V001T01A014–V001T01A014, American Society of Mechanical Engineers, 1981.
- [4] T. Krepec, A. Georgantas, M. Taylor, and C. To, “New family of low cost electronic fuel control units for small gas turbine engines,” *SAE transactions*, pp. 260–265, 1990.
- [5] G. Carrese, T. Krepec, and C. To, “Simulation, testing and optimization of a new low cost electronic fuel control unit for small gas turbine engines,” tech. rep., SAE Technical Paper, 1990.
- [6] R. Harrison and M. Yates, “Gas turbine fuel control systems for unmanned applications,” *Journal of engineering for gas turbines and power*, vol. 110, no. 1, pp. 33–40, 1988.
- [7] S. Usenmez, S. Ekinci, O. Uzol, and I. Yavrucuk, “Application of a fuzzy logic controller for speed control on a small-scale turbojet engine,” in *Proceedings of ASME Turbo Expo 2014*, (Dusseldorf, Germany), June 2014. GT2014-27158.
- [8] S. Ekinci, S. Usenmez, I. Yavrucuk, and O. Uzol, “Development and testing of a fuzzy logic controller for a small turbojet engine,” in *54th AIAA Aerospace Sciences Meeting, AIAA SciTech*, (San Diego, USA), December 2016. AIAA 2016-0120.

- [9] W. I. Rowen, "Simplified mathematical representations of heavy-duty gas turbines," *Journal of engineering for power*, vol. 105, no. 4, pp. 865–869, 1983.
- [10] M. Lichtsinder and Y. Levy, "Jet engine model for control and real-time simulations," *ASME. J. Eng. Gas Turbines Power*, vol. 128, no. 4, pp. 745–753, 2004.
- [11] "Advanced micro turbines (amt), the netherlands." <http://www.amtjets.com/OlympusHP.php>. Accessed: 2018-10-24.
- [12] M. Ballin, "A high fidelity real-time simulation of a small turboshaft engine," *NASA-TM-100991*, August 1988.
- [13] S. M. Camporeale, B. B. Fortunato, and M. M. Mastrovito, "A modular code for real time dynamic simulation of gas turbines in simulink," *ASME. J. Eng. Gas Turbines Power*, vol. 128, pp. 506–517, July 2002.
- [14] N. U. Rahman and J. F. Whidborne, "A numerical investigation into the effect of engine bleed on performance of a single-spool turbojet engine," in *Proc. IMechE, Part G: Journal of Aerospace Engineering*, vol. 222, (Publisher address), pp. 939–949, July 2008. Paper number 7.
- [15] Z. Leylek, W. S. Anderson, G. Rowlinson, and N. Smith, "An investigation into performance modeling of a small gas turbine engine," in *ASME Turbo Expo 2013: Turbine Technical Conference and Exposition*, pp. V05AT23A007–V05AT23A007, American Society of Mechanical Engineers, 2013.
- [16] O. Uzol, "A new high-fidelity transient aerothermal model for real-time simulations of the t700 helicopter turboshaft engine," *J. of Thermal Science and Technology*, vol. 31, pp. 37–44, June 2011.
- [17] G. Kocer, "Aerothermodynamic modelling and simulation of gas turbines for transient operating conditions," *Aerospace Engineering Department, Middle East Technical University*, 2008.
- [18] Y. Novikov, *Development of a High-Fidelity Transient Aerothermal Model for a Helicopter Turboshaft Engine for Inlet Distortion and Engine Deterioration Simulations*. PhD thesis, Middle East Technical University, 2012.

- [19] M. Montazeri-Gh, M. Nasiri, and S. Jafari, "Real-time multi-rate hil simulation platform for evaluation of a jet engine fuel controller," *Simulation Modelling Practice and Theory*, vol. 19, no. 3, pp. 996–1006, 2011.
- [20] R. Chacartegui, D. Sánchez, A. Muñoz, and T. Sánchez, "Real time simulation of medium size gas turbines," *Energy Conversion and Management*, vol. 52, no. 1, pp. 713–724, 2011.
- [21] J. DeCastro, J. Litt, and D. Frederick, "A modular aero-propulsion system simulation of a large commercial aircraft engine," in *44th AIAA/ASME/SAE/ASEE Joint Propulsion Conference & Exhibit*, p. 4579, 2008.
- [22] J. Mattingly, *Elements of Gas Turbine Propulsion*. AIAA education series, American Institute of Aeronautics and Astronautics, 2005.
- [23] H. Saravanamuttoo, H. Cohen, and G. Rodgers, *Gas turbine theory. Fifth edition*. Prentice Hall, 5 ed., 2001.
- [24] P. Walsh and P. Fletcher, *Gas Turbine Performance*. Wiley, 2008.
- [25] B. MacIsaac and R. Langton, *Gas Turbine Propulsion Systems*. John Wiley Sons, Ltd, 2011.
- [26] N. K. Sinha, C. D. Dicenzo, and B. Szabados, "Modeling of dc motors for control applications," *IEEE Transactions on Industrial Electronics and Control Instrumentation*, no. 2, pp. 84–88, 1974.
- [27] "Maxon motor catalog." <http://www.maxonmotor.com/maxon/view/catalog/>. Accessed: 2018-07-11.
- [28] S. Ekinici, A. T. Kutay, O. Uzol, and et al, "System identification and controller design for a small turbojet engine," (METU, Ankara, Turkey), 6th Ankara International Aerospace Conference, September 2011. AIAC-2011-085.
- [29] G. G. Kulikov and H. Thompson, *Dynamic Modelling of Gas Turbines: Identification, Simulation, Condition Monitoring and Optimal Control*. Springer, 2004.
- [30] L. Ljung, *System Identification: Theory for the User*. Prentice Hall information and system sciences series, Prentice Hall PTR, 1999.

- [31] R. Jategaonkar, *Flight vehicle system identification: a time domain methodology*. Progress in astronautics and aeronautics, American Institute of Aeronautics and Astronautics, 2006.
- [32] V. Klein and E. Morelli, *Aircraft System Identification: Theory and Practice*. AIAA education series, American Institute of Aeronautics and Astronautics, 2006.
- [33] F. Holzapfel, “Lecture notes in model reference adaptive control,” February 2017.
- [34] H. Khalil, *Nonlinear Systems*. Prentice Hall, 1996.
- [35] J. Slotine and W. Li, *Applied Nonlinear Control*. Prentice-Hall International Editions, Prentice-Hall, 1991.
- [36] S. Boyd and S. S. Sastry, “Necessary and sufficient conditions for parameter convergence in adaptive control,” *Automatica*, vol. 22, no. 6, pp. 629–639, 1986.
- [37] S. Sastry and M. Bodson, *Adaptive control: stability, convergence and robustness*. Courier Corporation, 2011.
- [38] G. Gursoy, *Direct Adaptive Flight Envelope Protection*. PhD thesis, Middle East Technical University, 2016.
- [39] G. Chowdhary, *Concurrent Learning for Convergence in Adaptive Control Without Persistency of Excitation*. PhD thesis, Georgia Institute of Technology, 2010.
- [40] S. Camporeale, L. Dambrosio, and B. Fortunato, “One step ahead adaptive control for gas turbine power plants,” in *ASME 1999 International Gas Turbine and Aeroengine Congress and Exhibition*, pp. V004T04A004–V004T04A004, American Society of Mechanical Engineers, 1999.
- [41] S. Chatterjee and J. Litt, “Online model parameter estimation of jet engine degradation for autonomous propulsion control,” in *AIAA Guidance, Navigation, and Control Conference and Exhibit*, p. 5425, 2003.
- [42] A. Volponi and D. L. Simon, “Enhanced self tuning on-board real-time model (estorm) for aircraft engine performance health tracking,” 2008.

- [43] A. Kreiner and K. Lietzau, "The use of onboard real-time models for jet engine control," *Project Report OBIDICOTE, MTU Aero Engines, Munich, Germany*, 2000.
- [44] P. A. Ioannou and J. Sun, *Robust adaptive control*, vol. 1. PTR Prentice-Hall Upper Saddle River, NJ, 1996.
- [45] Z. Ding, *Nonlinear and Adaptive Control Systems*. IET CONTROL ENGINEERING SERIES, Institution of Engineering and Technology, 2013.
- [46] M. A. Duarte and K. S. Narendra, "Indirect model reference adaptive control with dynamic adjustment of parameters," *International journal of adaptive control and signal processing*, vol. 10, no. 6, pp. 603–621, 1996.
- [47] I. Yavrucuk, J. Prasad, and S. Unnikrishnan, "Envelope protection for autonomous unmanned aerial vehicles," *Journal of Guidance, Control, and Dynamics*, vol. 32, no. 1, pp. 248–261, 2009.
- [48] I. Yavrucuk and J. V. R. Prasad, "Online dynamic trim and control limit estimation," *Journal of Guidance, Control, and Dynamics*, vol. 35, no. 5, pp. 1647–1656, 2012.





## Appendix A

### AMT OLYMPUS TURBOJET ENGINE SPECIFICATIONS

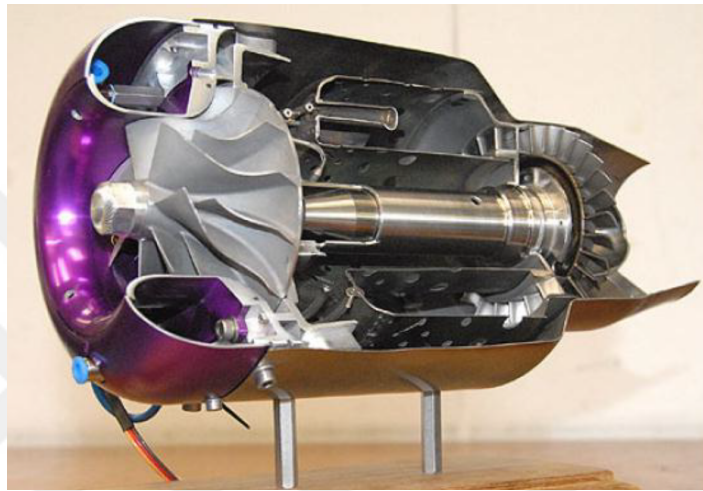


Figure A.1: Cutaway View of the AMT Olympus Turbojet Engine [15]

Table A.1: Technical Specifications of the AMT Olympus Turbojet Engine [14]

Engine Parameter	Value	Unit
Diameter	130	mm
Length	270	mm
Maximum Thrust	190	N
Pressure Ratio	4:1	
Mass Flow Rate	0.4	kg/s
Maximum Rotational Speed	112500	RPM
Nominal EGT	923	K
Maximum EGT	973	K
Maximum Fuel Consumption	0.4	kg/min



## Appendix B

### GENERAL PROCEDURE FOR FINDING AN APPROPRIATE NONLINEAR MODEL STRUCTURE

The data set, model structure, and identification method can be defined as the basic steps of the system identification procedure. For the success of the identification process, a suitable model structure that defines the relationship between the regressors and unknown system parameters is very important.

As the common approach, any system can be approximated by linear models around its equilibrium points. These piecewise-linear models can then be combined into a single model by using look-up tables. As an alternative way, a single nonlinear model structure can also be defined. This section provides a general procedure for finding an appropriate nonlinear model structure that can simulate target system dynamics.

First, a base model needs to be selected. As a rule of thumb, it is better to start with simple linear models. For this, a first-order transfer function can be chosen as the base model candidate:

$$\frac{\Delta N(s)}{\Delta V(s)} = \frac{K}{\tau s + 1} \quad (\text{B.1})$$

where  $\tau$  is the time constant, and  $K$  is the gain of the function.

Second, the appropriate parameter values for this function are found around the selected equilibrium point. The obtained transfer function is then tested in the operational envelope of the system. As an example, for our case, a first-order transfer function with  $K = 1.85$  and  $\tau = 0.8$  values fits on the aero-thermal engine model response between the shaft speeds of  $90\%N_{max}$  and  $94\%N_{max}$ . The response of the linear model for the out of this region can be seen in Fig. B.1

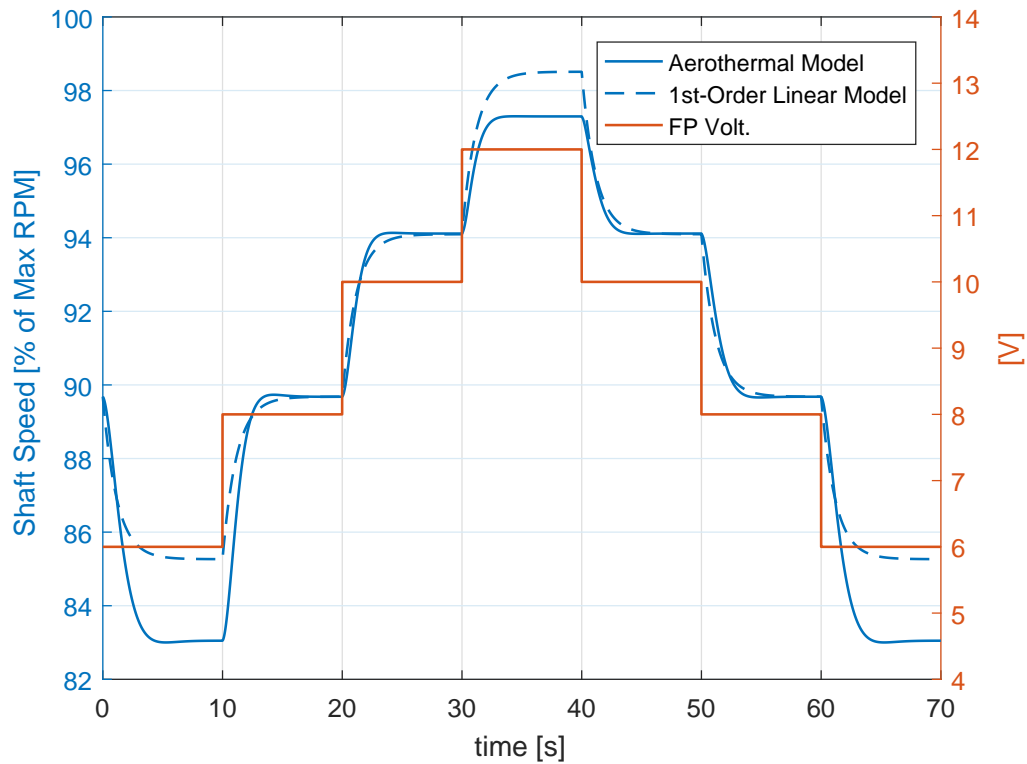


Figure B.1: First-Order Linear Model Output Comparison with Aero-Thermal Model Data

As shown in the figure, the output of this linear model, indicated by a dashed line, is incorrect at higher and lower shaft speeds. As it is known, the time constant  $\tau$  only affects the transient behavior of the linear model. So here, the major source of the error is the inaccurate  $K$  value. For this example, it is obvious that the  $K$  gain value varies with the shaft speed. As a general procedure, the linear function parameters must be represented as a function of the system states. For instance, here, the gain  $K$  can be modified as a function of the shaft speed. As a good starting point, a linear function can be selected as:

$$K = \alpha_1 \Delta N(s) + \alpha_0 \quad (\text{B.2})$$

where the  $\alpha$ 's are the coefficients of the linear function. Therefore, the first-order transfer function defined in Eqn. B.1 becomes:

$$\frac{\Delta N(s)}{\Delta V(s)} = \frac{\alpha_1 \Delta N(s) + \alpha_0}{\tau s + 1} \quad (\text{B.3})$$

If this equation is converted to the time-domain and rearranged, the following is obtained:

$$\Delta \dot{N} = \frac{-1}{\tau} \Delta N + \frac{\alpha_0}{\tau} \Delta V + \frac{\alpha_1}{\tau} \Delta N \Delta V \quad (\text{B.4})$$

The linear part of this nonlinear system model:

$$LP = \frac{-1}{\tau} \Delta N + \frac{\alpha_0}{\tau} \Delta V \quad (\text{B.5})$$

is still a first-order system, and the rest of the equation is the nonlinear part of the model:

$$NLP = \frac{\alpha_1}{\tau} \Delta N \Delta V \quad (\text{B.6})$$

Here; the regressor vector becomes:

$$x = [\Delta N \quad \Delta V \quad \Delta N \Delta V] \quad (\text{B.7})$$

and, the unknown parameter vector  $\theta$  is:

$$\theta = \left[ -\frac{1}{\tau} \quad \frac{\alpha_0}{\tau} \quad \frac{\alpha_1}{\tau} \right]^T \quad (\text{B.8})$$

By applying Eqn. 3.22 on the shaft speed data given in Fig. B.1, the parameter estimates  $\hat{\theta}$  are obtained as:

$$\hat{\theta} = [-0.5662 \quad 1.5632 \quad -0.0628] \quad (\text{B.9})$$

and the nonlinear system model given in Eqn. B.4 becomes:

$$\Delta \dot{N} = -0.5662 \Delta N + 1.5632 \Delta V - 0.0628 \Delta N \Delta V \quad (\text{B.10})$$

Finally, the estimated system parameters are found as follows:

$$\tau = 1.766$$

$$\alpha_0 = 2.7607$$

$$\alpha_1 = -0.11087$$

The model response comparison with the aero-thermal turbojet engine data is shown in Fig B.2

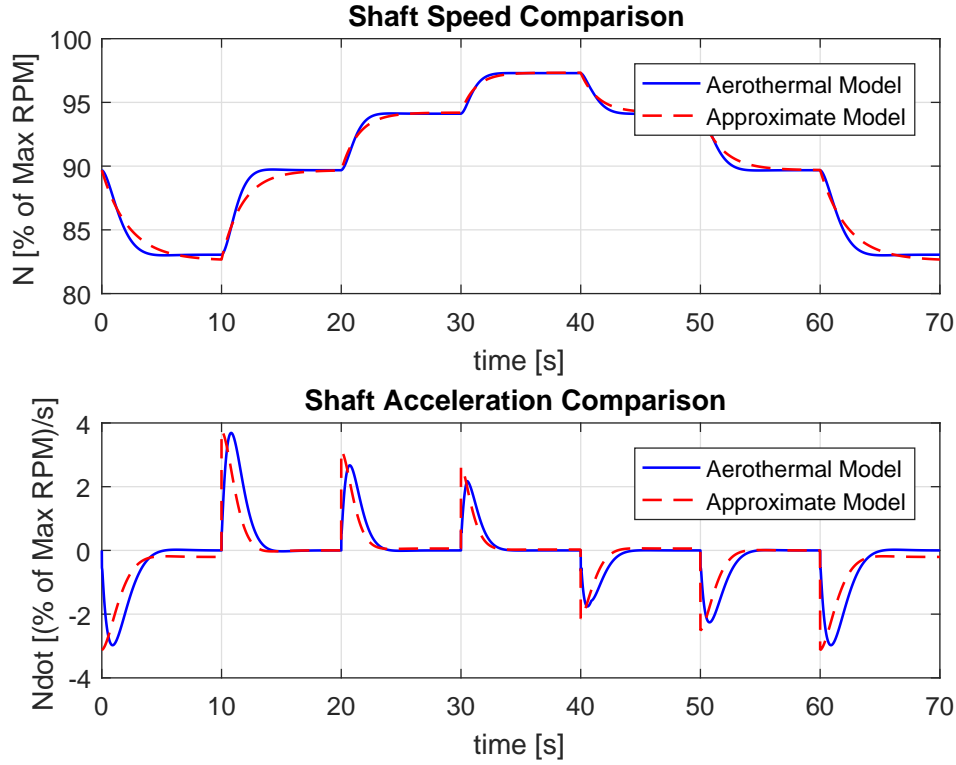


Figure B.2: First-Order Non-Linear Model Output Comparison with Aero-Thermal Model Data (with a linear  $K$  gain function)

Third, the order of  $K$  gain function can be increased for a better convergence. For our case, if the gain  $K$  is modified as a second-order polynomial of the shaft speed and applied to Eqn. B.1, the following is obtained:

$$\frac{\Delta N(s)}{\Delta V(s)} = \frac{\alpha_2 \Delta N(s)^2 + \alpha_1 \Delta N(s) + \alpha_0}{\tau s + 1} \quad (\text{B.11})$$

In the time-domain, this equation becomes:

$$\Delta \dot{N} = \frac{-1}{\tau} \Delta N + \frac{\alpha_0}{\tau} \Delta V + \frac{\alpha_1}{\tau} \Delta N \Delta V + \frac{\alpha_2}{\tau} \Delta N^2 \Delta V \quad (\text{B.12})$$

Again, the linear part of the model structure:

$$LP = \frac{-1}{\tau} \Delta N + \frac{\alpha_0}{\tau} \Delta V \quad (\text{B.13})$$

is still a first-order system, and the nonlinear part of the model becomes:

$$NLP = \frac{\alpha_1}{\tau} \Delta N \Delta V + \frac{\alpha_2}{\tau} \Delta N^2 \Delta V \quad (\text{B.14})$$

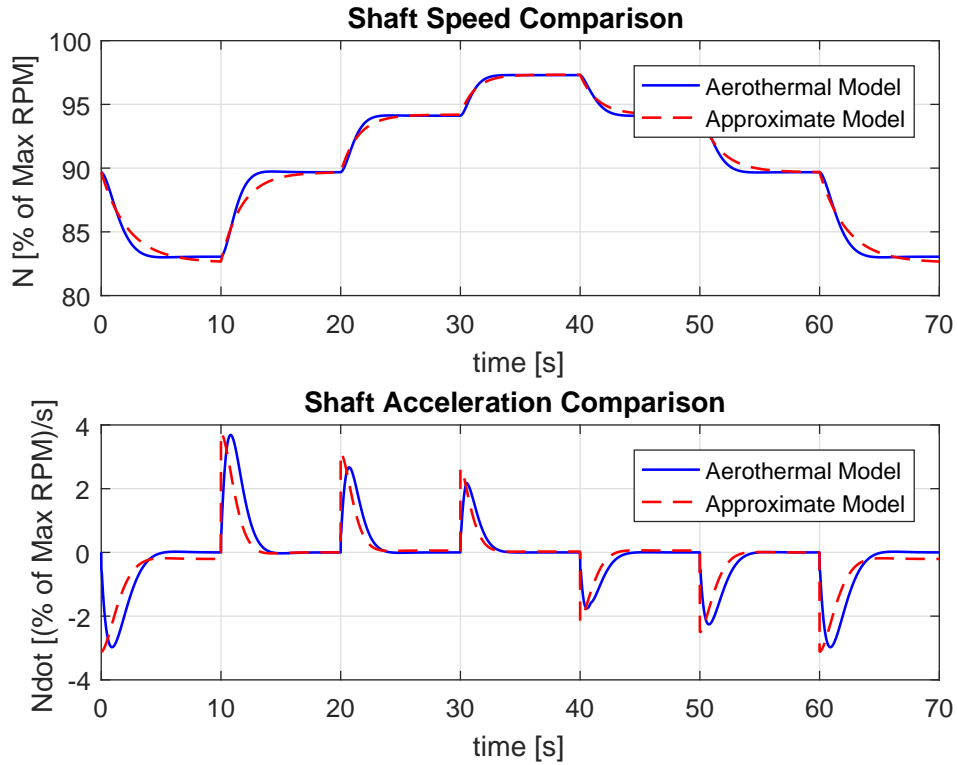


Figure B.3: First-Order Non-Linear Model Output Comparison with Aero-Thermal Model Data (with a second-order K gain polynomial)

So, the regressor vector can be modified as:

$$x = [\Delta N \quad \Delta V \quad \Delta N \Delta V \quad \Delta N^2 \Delta V] \quad (\text{B.15})$$

and, the unknown parameter vector  $\theta$  is:

$$\theta = \left[ -\frac{1}{\tau} \quad \frac{\alpha_0}{\tau} \quad \frac{\alpha_1}{\tau} \quad \frac{\alpha_2}{\tau} \right]^T \quad (\text{B.16})$$

If the least-square estimation equation given in 3.22 is applied to this first-order non-linear model structure, the parameter estimation vector  $\hat{\theta}$  is found as:

$$\hat{\theta} = [-0.5665 \quad 1.5629 \quad -0.0628 \quad 2.59e^{-5}] \quad (\text{B.17})$$

Finally, the estimated system parameters are found as follows:

$$\tau = 1.7652$$

$$\alpha_0 = 2.7589$$

$$\alpha_1 = -0.11091$$

$$\alpha_2 = -4.5865e^{-5}$$

The comparison of this model with aero-thermal turbojet engine data is shown in Fig B.3. In this case, the parameter estimations ( $\tau, \alpha_0, \alpha_1$ ) are very close to the previous estimations. The last parameter value ( $\alpha_2$ ) is too small, so it doesn't make a big difference in the results. The important thing here is that the order of the  $K$  gain function can be increased until the satisfactory condition is reached.

Fourth, the other model parameters can also be represented as a function of the system state. For the first-order base model case, the time constant  $\tau$  can be modified as a function of shaft speed to increase the convergence around the transient regions. In this case, the resulting regressor model cannot be separated as a linear and nonlinear part. However, the obtained model still can be used as an approximate model and its parameters can be estimated with the least squares method.

As the last step, the order of the linear base model can be increased. For instance, in Chp: 3, a second-order transfer function was selected as the base model and then the  $K$  gain is defined as a second-order polynomial of the shaft speed. The complexity of the base model and its parameter functions can be increased similarly until the satisfactory condition is reached. Consequently, the described procedure can be applied easily to any nonlinear system to obtain the nonlinear approximate model structure.



## CURRICULUM VITAE

### PERSONAL INFORMATION

**Surname, Name:** Ekinci, Sinan

**Nationality:** Turkish (TC)

**Date and Place of Birth:** 02.05.1981, Rotterdam

**Marital Status:** Married

**E-mail:** ekincisi@gmail.com

### EDUCATION

<b>Degree</b>	<b>Institution</b>	<b>Year of Graduation</b>
M.S.	ITU, Department of Mechatronics Engineering	2007
B.S.	ITU, Department of Aeronautical Engineering	2003
High School	Kırşehir Mehmet Akif Ersoy Lisesi	1998

### PROFESSIONAL EXPERIENCE

<b>Year</b>	<b>Place</b>	<b>Enrollment</b>
2016 - 2017	Reiser Simulation and Training GmbH., Munich	Software Developer
2010 - 2016	Aerotim Engineering LLC., Ankara	Senior Engineer
2006 - 2009	Roketsan Missile Inc., Ankara	Control Engineer

## **PUBLICATIONS**

### **International Conference Publications**

Ekinci, S., Usenmez, S., Yavrucuk, I., and Uzol, O., 2016. "Development and testing of a fuzzy logic controller for a small turbojet engine". In 54th AIAA Aerospace Sciences Meeting, AIAA SciTech. AIAA 2016-0120.

Usenmez, S., Ekinci, S., Uzol, O., and Yavrucuk, I., 2014. "Application of a fuzzy logic controller for speed control on a small-scale turbojet engine". In Proceedings of ASME Turbo Expo 2014. GT2014-27158.

Ekinci, S., Kutay, A. T., Uzol, O., and et al, 2011. "System identification and controller design for a small turbojet engine". 6th Ankara International Aerospace Conference. AIAC-2011-085.

### **National Conference Publications**

Usenmez, S.; Ekinci, S.; Yavrucuk, I.; Uzol, O.; "Bulanık Mantık Kontrolcüsü ile Küçük Ölçekli Turbojet Motorlara Devir Kontrolü Uygulaması"; TOK 2014 Türkiye Otomatik Kontrol Konferansı, Kocaeli.

Ekinci, S.; Usenmez, S.; Yavrucuk, I.; Kutay, A.T.; Uzol, O.; Kahraman, K.; "ArGe'den Ürüne FADEC Geliştirme Süreci", SAVTEK 2014 Savunma Teknolojileri Konferansı, Ankara.

Ekinci, S.; Kutay, A.T.; Uzol, O.; Kahraman, K.; "Küçük Turbojet/Turboprop Motorları için Özgün Elektronik Kontrol Ünitesi (EKÜ/FADEC) Tasarımı, Doğrulanması Ve Uygulanması"; SAVTEK 2012 Savunma Teknolojileri Konferansı, Ankara.

Ekinci, S.; Yavrucuk, I.; "Küçük İnsansız Hava Araçları için Düşük Maliyetli Otopilot Tasarımı", UHUK 2010 Ulusal Havacılık Konferansı, Eskişehir.

Ekinci, S.; Arslantas, Y. E.; Yavrucuk, I.; "İnsansız Helikopterin Uçuş Kontrol Algoritmalarının Gelistirilmesi için Test Platformu Tasarımları"; SAVTEK 2010 Savunma Teknolojileri Konferansı, Ankara.